Article

Metabolic regulation of species-specific developmental rates

https://doi.org/10.1038/s41586-022-05574-4

Received: 31 August 2021

Accepted: 18 November 2022

Published online: 4 January 2023

Check for updates

Margarete Diaz-Cuadros[1,2,13]✉, Teemu P. Miettinen[3], Owen S. Skinner[4,5,6], Dylan Sheedy[1,2], Carlos Manlio Díaz-García[7,14], Svetlana Gapon[1,2], Alexis Hubaud[1,2], Gary Yellen[7], Scott R. Manalis[3,8,9], William M. Oldham[10,11] & Olivier Pourquié[1,2,12]✉

Animals display substantial inter-species variation in the rate of embryonic development despite a broad conservation of the overall sequence of developmental events. Differences in biochemical reaction rates, including the rates of protein production and degradation, are thought to be responsible for species-specific rates of development[1–3]. However, the cause of differential biochemical reaction rates between species remains unknown. Here, using pluripotent stem cells, we have established an in vitro system that recapitulates the twofold difference in developmental rate between mouse and human embryos. This system provides a quantitative measure of developmental speed as revealed by the period of the segmentation clock, a molecular oscillator associated with the rhythmic production of vertebral precursors. Using this system, we show that mass-specific metabolic rates scale with the developmental rate and are therefore higher in mouse cells than in human cells. Reducing these metabolic rates by inhibiting the electron transport chain slowed down the segmentation clock by impairing the cellular NAD^+/NADH redox balance and, further downstream, lowering the global rate of protein synthesis. Conversely, increasing the NAD^+/NADH ratio in human cells by overexpression of the *Lactobacillus brevis* NADH oxidase *Lb*NOX increased the translation rate and accelerated the segmentation clock. These findings represent a starting point for the manipulation of developmental rate, with multiple translational applications including accelerating the differentiation of human pluripotent stem cells for disease modelling and cell-based therapies.

The rate of embryonic development across animal taxa varies among species and is correlated with lifespan, body size and other life history traits[4,5]. Among mammals, large-bodied species develop at slower rates and display increased lifespans (for example, humans) compared with small-bodied animals[6] (for example, mice). Although early mouse and human embryos undergo the same series of developmental steps and are similar in overall size, human embryos undergo the same steps 2–3 times more slowly[7]. The segmentation clock represents an ideal model to study developmental rate because its period is species-specific and temperature-sensitive, and it scales with the speed of embryonic development[1,8,9]. This clock consists of a molecular oscillator that operates in the precursors of the musculoskeletal system in the presomitic mesoderm (PSM), where it controls the periodicity of somite formation[10].

An in vitro model of developmental rate

We previously reported the establishment of pluripotent stem cell (PSC)-derived models of the mouse and human segmentation clocks[11]. We developed an updated protocol to differentiate mouse and human PSCs towards the PSM fate under identical conditions (Fig. 1a). The differentiation efficiency was remarkably high, with 78.3 ± 1% of mouse and 96.5 ± 1.5% of human cells expressing the posterior PSM-specific marker MSGN1-Venus (Fig. 1b and Extended Data Fig. 1a). Mouse cells activated MSGN1-Venus with accelerated kinetics compared with human cells (1–2 days for mouse versus 2–3 days for human) (Fig. 1b). The duration of the cell cycle was also shorter in mouse than in human PSM cells (13.9 ± 2 h versus 21.9 ± 3.6 h, respectively) (Fig. 1c). The oscillations of the segmentation clock reporter HES7-Achilles were more frequent in mouse than in human PSM cells (2.6 ± 0.3 h versus 4.9 ± 0.3 h) (Fig. 1d,e and Supplementary Videos 1 and 2)[12–14]. Notably, the cell cycle time and segmentation clock period of PSC-derived mouse PSM cells did not significantly differ from those of primary PSM cells from E9.5 embryos[15] (clock period: 2.5 ± 0.3 h versus 2.6 ± 0.1 h, $P = 0.314$; cell cycle: 13.9 ± 2 h versus 13.07 ± 1 h, $P = 0.057$) (Extended Data Fig. 1b,c). Together, these observations indicated an approximately twofold difference in developmental rate between mouse and human PSM cells differentiating in vitro.

[1]Department of Genetics, Harvard Medical School, Boston, MA, USA. [2]Department of Pathology, Brigham and Women's Hospital, Boston, MA, USA. [3]Koch Institute for Integrative Cancer Research, Massachusetts Institute of Technology, Cambridge, MA, USA. [4]Department of Molecular Biology, Massachusetts General Hospital, Boston, MA, USA. [5]Department of Systems Biology, Harvard Medical School, Boston, MA, USA. [6]Broad Institute, Cambridge, MA, USA. [7]Department of Neurobiology, Harvard Medical School, Boston, MA, USA. [8]Department of Biological Engineering, Massachusetts Institute of Technology, Cambridge, MA, USA. [9]Department of Mechanical Engineering, Massachusetts Institute of Technology, Cambridge, MA, USA. [10]Department of Medicine, Harvard Medical School, Boston, MA, USA. [11]Department of Medicine, Brigham and Women's Hospital, Boston, MA, USA. [12]Harvard Stem Cell Institute, Harvard University, Cambridge, MA, USA. [13]Present address: Department of Molecular Biology, Massachusetts General Hospital, Boston, MA, USA. [14]Present address: Department of Biochemistry and Molecular Biology, University of Oklahoma Health Sciences Center, Oklahoma City, OK, USA. ✉e-mail: mdiazcuadros@g.harvard.edu; pourquie@genetics.med.harvard.edu

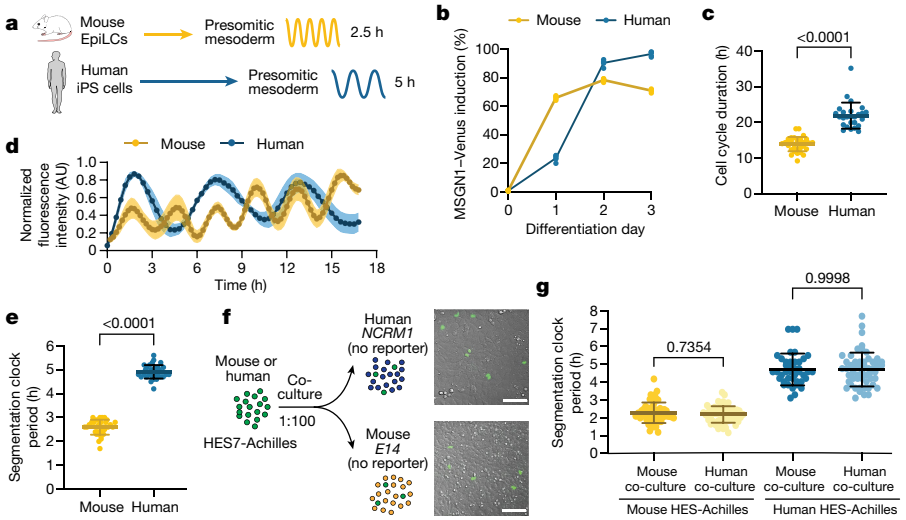

Fig. 1 | Cell-autonomous differences in developmental rate between differentiating mouse and human PSM cells. a, Schematic illustrating the differentiation of mouse and human PSCs towards PSM fate. The accelerated developmental pace of mouse cells is reflected in the reduced induction time and short oscillatory period relative to human cells. EpiLCs, epiblast-like cells; iPS cells, induced pluripotent stem cells. **b**, PSM induction efficiency over the course of 3 days of differentiation for mouse and human PSCs. The percentage of cells expressing MSGN1-Venus was assessed by flow cytometry. $n = 5$ independent experiments. **c**, Cell cycle duration for PSC-derived mouse and human PSM cells. Data are mean ± s.d. $n = 33$ (mouse), $n = 26$ (human). Unpaired two-sided t-test: $P = 2.88 \times 10^{-15}$. **d**, HES7-Achilles oscillation profiles for PSC-derived mouse and human PSM cells over the course of 18 h. Data are mean ± s.e.m. $n = 5$ independent experiments. AU, arbitrary units. **e**, Period of HES7-Achilles oscillations in PSC-derived mouse and human PSM cells. Data are mean ± s.d. $n = 25$. Unpaired two-sided t-test: $P = 7.33 \times 10^{-41}$. **f**, Left, experimental strategy for the co-culture of CAG-H2B-mCherry; HES7-Achilles human or CAG-NLS-BFP; Hes7-Achilles mouse PSM cells with non-reporter mouse E14 or human NCRM1 PSM cells at a ratio of 1:100. Right, merged bright-field and fluorescence images of human HES7-Achilles in human–human (top) and human–mouse (bottom) co-cultures. Scale bars, 100 µm. **g**, Period of HES7-Achilles oscillations in mouse (left) or human (right) HES7-Achilles PSM cells co-cultured with an excess of either mouse or human non-reporter PSM cells. Data are mean ± s.d. $n = 56$ (mouse–mouse), $n = 56$ (mouse–human), $n = 41$ (human–mouse), $n = 53$ (human–human). One-way ANOVA with Šidák correction.

In vitro, the segmentation clock retains its species-specific period in isolated cells[1,11,15]. When we performed homo- or hetero-specific co-cultures of individual mouse Hes7-Achilles reporter PSM cells mixed with unlabelled PSM cells of either human or mouse origin at a ratio of 1:100 (Fig. 1f), the segmentation clock period remained unchanged (2.29 ± 0.57 h versus 2.19 ± 0.46 h, $P = 0.73$) (Fig. 1g, Extended Data Fig. 1d,f,h,I and Supplementary Video 3). This was also true for individual human reporter cells co-cultured with an excess of either human or mouse PSM cells (4.71 ± 0.94 h versus 4.71 ± 0.88 h, $P = 0.99$) (Fig. 1g, Extended Data Fig. 1e,f,j,k and Supplementary Video 4). Although inter-species co-culture conditions gave rise to variable effects in oscillation amplitude (Extended Data Fig. 1g–k), these results indicated that the segmentation clock period is controlled autonomously by the cell.

The cell cycle has been proposed to function as a clock that controls developmental speed[2,16]. However, treating human PSM cells with aphidicolin led to near-complete cell cycle arrest but did not affect the oscillatory period (4.93 ± 0.47 h versus 4.88 ± 0.31 h, $P = 0.7378$) (Extended Data Fig. 2a,b). Thus, the cell cycle does not contribute to the regulation of the segmentation clock period.

Species-specific metabolic rates

According to Kleiber's law, mass-specific metabolic rates scale allometrically with adult body mass[17]. Gestation length also scales with adult body mass[18], suggesting that differences in basal metabolism could potentially explain the accelerated biochemical kinetics associated with faster development in mouse compared to human cells[1,2]. When comparing similar numbers of PSM cells, basal glycolytic proton efflux rate (glycoPER) was not different between mouse and human cells ($8.9 \times 10^{-3} \pm 6.3 \times 10^{-4}$ pmol min^{-1} per cell versus $8.8 \times 10^{-3} \pm 4.4 \times 10^{-4}$ pmol min^{-1} per cell, $P = 0.783$) and basal oxygen consumption rate (OCR) was slightly higher in human cells ($1.01 \times 10^{-3} \pm 4.3 \times 10^{-5}$ pmol min^{-1} per cell versus $1.09 \times 10^{-3} \pm 4.5 \times 10^{-5}$ pmol min^{-1} per cell, $P = 0.0002$) (Extended Data Fig. 2c,d).

However, we noted that human PSM cells had approximately twice the volume of mouse cells (2,060 ± 524 fl versus 885.9 ± 157.9 fl, $P < 0.0001$) (Fig. 2a and Extended Data Fig. 2e). When measured with a suspended microchannel resonator[19,20] (SMR), the mass of human cells was also approximately twice that of mouse cells (2,002 ± 71 pg versus 1,066 ± 56 pg, $P < 0.0001$) (Fig. 2b and Supplementary Table 2), such that the density was qualitatively similar for both species (1.057 ± 0.003 pg fl^{-1} versus 1.061 ± 0.002 pg fl^{-1}, $P = 0.03$) (Extended Data Fig. 2f and Supplementary Table 2). We also measured the dry mass, dry volume and dry density of single cells by comparing the cell's buoyant mass in medium prepared with either normal water (H_2O) or deuterium-based heavy water[19,20] (D_2O). The dry mass of mouse PSM cells was less than half that of human cells (162 ± 5.7 pg versus 380 ± 29.6 pg, $P = 0.0002$), as was dry volume (113 ± 5 fl versus 278 ± 24 fl, $P = 0.0003$) (Extended Data Fig. 2g,h and Supplementary Table 2). Dry mass density, which depends on the molecular composition of the cell, was thus qualitatively similar between the two species (1.435 ± 0.015 pg fl^{-1} versus 1.365 ± 0.012 pg fl^{-1}, $P = 0.004$) (Extended Data Fig. 2i and Supplementary Table 2). Thus, human cells contained twice as much biological material as mouse cells. Consequently, normalization by either volume or mass is required to correct for the cell size difference between the two species. Mass-specific OCR ($1.013 \times 10^{-6} \pm 4.333 \times 10^{-8}$ pmol min^{-1} pg^{-1} versus $5.475 \times 10^{-7} \pm 2.272 \times 10^{-8}$ pmol min^{-1} pg^{-1}, $P < 0.0001$) and glycoPER ($8.905 \times 10^{-6} \pm 6.372 \times 10^{-7}$ pmol min^{-1} pg^{-1} versus $4.425 \times 10^{-6} \pm 2.212 \times 10^{-7}$ pmol min^{-1} pg^{-1}, $P < 0.0001$) were twice as high in mouse compared with human cells (Fig. 2c,d). The extracellular acidification rate (ECAR), which accounts for glycolytic and other acidification sources such as CO_2 secretion, was also twice as high per unit mass in mouse

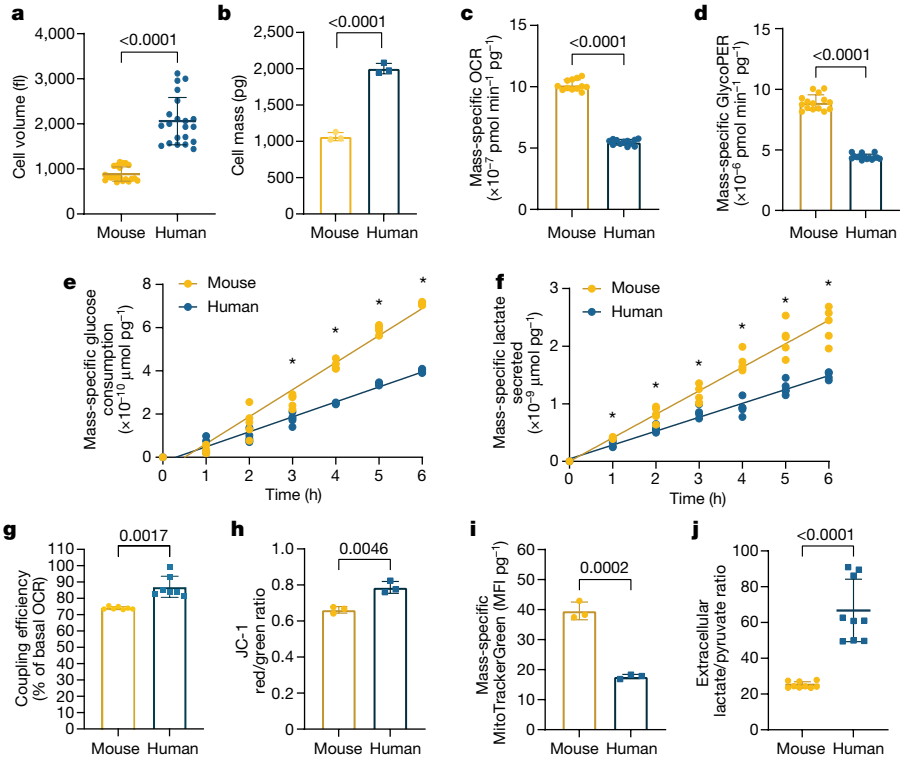

Fig. 2 | Mass-specific metabolic rates are higher in mouse PSM cells compared with human PSM cells. a, Volume of MSGN1-Venus$^+$ PSC-derived mouse and human PSM cells as measured with a Coulter counter. Data are mean ± s.d. $n = 21$. Unpaired two-sided t-test: $P = 3.25 \times 10^{-12}$. **b**, Total cell mass of MSGN1-Venus$^+$ PSC-derived mouse and human PSM cells as measured on a SMR. Each data point represents the mean of more than 200 individual cells. Data are mean ± s.d. $n = 3$ independent experiments. Unpaired two-sided t-test: $P = 5.77 \times 10^{-5}$. **c**, Mass-specific oxygen consumption rate for MSGN1-Venus$^+$ PSC-derived mouse and human PSM cells. Data are mean ± s.d. $n = 12$. Unpaired two-sided t-test: $P = 3.19 \times 10^{-20}$. **d**, Mass-specific glycolytic proton efflux rate for MSGN1-Venus$^+$ PSC-derived mouse and human PSM cells. Data are mean ± s.d. $n = 15$. Unpaired two-sided t-test: $P = 5.05 \times 10^{-21}$. **e**, Mass-specific cumulative glucose consumption for MSGN1-Venus$^+$ PSC-derived mouse and human PSM cells. $n = 5$. Multiple unpaired two-sided t-tests with false discovery rate (FDR) = 1%. P values: 1 h, 0.6074; 2 h, 0.0691, 3 h, 0.0013, 4 h, 7.44×10^{-8}; 5 h, 2.29×10^{-9}; 6 h, 3.58×10^{-12}. **f**, Mass-specific cumulative lactate secretion for MSGN1-Venus$^+$ PSC-derived mouse and human PSM cells. $n = 5$. Multiple unpaired two-sided t-tests with FDR = 1%. P values: 1 h, 0.00364; 2 h, 0.00246; 3 h, 0.0128; 4 h, 0.000039; 5 h, 0.000259; 6 h, 0.000172. **g**, Coupling efficiency shown as the percent of basal oxygen consumption linked to ATP production in MSGN1-Venus$^+$ PSC-derived mouse and human PSM cells. Data are mean ± s.d. $n = 7$ biological replicates. Unpaired two-sided t-test. **h**, Inner mitochondrial membrane potential (ΔΨm) in PSC-derived mouse and human PSM cells as measured by the ratiometric JC-1 dye. Data are mean ± s.d. $n = 4$ biological replicates. Unpaired two-sided t-test. **i**, Mass-specific mitochondrial content (MitoTracker Green) in PSC-derived mouse and human PSM cells. Data are mean ± s.d. $n = 6$ biological replicates. Unpaired two-sided t-test. **j**, Extracellular lactate/pyruvate ratio in PSC-derived mouse and human PSM cells, which reflects the cytosolic NADH/NAD$^+$ ratio. Data are mean ± s.d. $n = 9$. Unpaired two-sided t-test with Welch's correction: $P = 9.02 \times 10^{-5}$. *$P < 0.05$.

compared with human cells ($5.685 \times 10^{-7} \pm 3.493 \times 10^{-8}$ mpH min^{-1} pg^{-1} versus $2.805 \times 10^{-7} \pm 1.315 \times 10^{-8}$ mpH min^{-1} pg^{-1}) (Extended Data Fig. 2j).

Rates of glucose consumption (mouse: 1.252×10^{-10} µmol pg^{-1} h^{-1}, 95% confidence interval: 1.172×10^{-10} to 1.333×10^{-10} µmol pg^{-1} h^{-1} versus human: 6.922×10^{-11} µmol pg^{-1} h^{-1}, 95% confidence interval: 6.524×10^{-11} to 7.319×10^{-11} µmol pg^{-1} h^{-1}; $P < 0.0001$) and lactate secretion (mouse: 4.085×10^{-10} µmol pg^{-1} h^{-1}, 95% confidence interval: 3.777×10^{-10} to 4.394×10^{-10} µmol pg^{-1} h^{-1} versus human: 2.410×10^{-10} µmol pg^{-1} h^{-1}, 95% confidence interval: 2.249×10^{-10} to 2.571×10^{-10} µmol pg^{-1} h^{-1}, $P < 0.0001$) per unit mass were significantly higher in mouse cells (Fig. 2e,f). These data are consistent with the Warburg-like metabolism of PSM cells, in which active glycolysis producing large amounts of lactate coexists with aerobic respiration[21,22]. Mass-specific glutamine consumption was also significantly higher in mouse PSM cells (0.00136 ± 0.00022 relative light units (RLU) pg^{-1} versus 0.00078 ± 0.0002237 RLU pg^{-1}, $P = 0.0103$) (Extended Data Fig. 2k).

We compared the metabolic rates of mouse and human neural progenitors differentiated in vitro from PSCs. PAX6$^+$ neural progenitors were induced after 5 days for mouse and 7 days for human PSCs (Extended Data Fig. 2l,m). We did not detect significant volume differences between mouse and human neural progenitors (1,255 ± 88 fl versus 1,203 ± 86 fl, $P = 0.5101$) (Extended Data Fig. 2n). However, volume-specific OCR ($8.437 \times 10^{-7} \pm 6.779 \times 10^{-8}$ pmol min^{-1} fl^{-1} versus $1.449 \times 10^{-7} \pm 1.859 \times 10^{-8}$ pmol min^{-1} fl^{-1}, $P < 0.0001$) and ECAR ($2.99 \times 10^{-7} \pm 5.781 \times 10^{-8}$ mpH min^{-1} fl^{-1} versus $1.76 \times 10^{-7} \pm 2.521 \times 10^{-8}$ mpH min^{-1} fl^{-1}, $P < 0.0001$) were significantly higher in mouse (Extended Data Fig. 2o,p). Thus, normalized metabolic rates are higher in mouse PSM and neural progenitor cells compared with the equivalent human cells.

We next performed stable isotope tracing with uniformly labelled [U-$^{13}C_6$]glucose and [U-$^{13}C_5$]glutamine in mouse and human PSM cells. Temporal labelling profiles were qualitatively similar between both species and labelling patterns for most metabolites were stabilized by 24 h (Extended Data Fig. 3a–f and Supplementary Table 3). At isotopic steady state, glucose tracing led to high labelling levels for pyruvate and lactate, as well as partial labelling of TCA intermediates (Extended Data Fig. 3g–l). Glutamine tracing showed intermediate labelling levels for glutamate and TCA metabolites, but not pyruvate or lactate, supporting an anaplerotic role in the TCA cycle (Extended Data Fig. 3m–r). Of note, stable isotope labelling patterns were almost identical between species, indicating that only the rate of glucose and glutamine utilization by downstream metabolic pathways differs between mouse and human.

We next performed mitochondrial stress tests using a Seahorse instrument. Mouse and human PSM cells differed in their maximal

mass-specific respiration rate ($2.117 \times 10^{-6} \pm 1.559 \times 10^{-7}$ pmol min^{-1} pg^{-1} versus $4.467 \times 10^{-7} \pm 5.737 \times 10^{-8}$ pmol min^{-1} pg^{-1}, $P < 0.0001$) and their spare respiratory capacity (192 ± 11.6% versus 119.7 ± 4.2% of basal OCR, $P < 0.0001$), which were significantly higher in mouse cells (Extended Data Fig. 4a,b). Respiration was less coupled to ATP production in mouse cells than in human cells (74 ± 0.9% versus 87 ± 6.4% of basal OCR, $P = 0.0017$), reflecting an increase in proton leak (Fig. 2g)[23]. Measurement of the inner mitochondrial membrane potential ($\Delta\Psi_m$) with the ratiometric dye JC-1 revealed lower $\Delta\Psi_m$ in mouse cells than in human cells (red/green fluorescence ratio—0.66 ± 0.018 versus 0.78 ± 0.033, $P = 0.0046$) (Fig. 2h). Staining differentiated cells with MitoTracker Green revealed that the mitochondrial content per unit mass is approximately twice as high in mouse as in human cells (39.5 ± 2.9 mean fluorescence intensity (MFI) pg^{-1} versus 17.7 ± 0.7 MFI pg^{-1}, $P = 0.0002$) (Fig. 2i). Moreover, when we isolated mitochondria from PSM cells and cultured them with complex I substrates (that is, pyruvate and malate), mouse mitochondrial OCR was consistently higher than in the human cells (Extended Data Fig. 4c). Thus, mitochondrial abundance and inherent differences in mitochondrial properties contribute to the elevated respiration in mouse PSM cells[24].

ETC impairment slows the clock

In the chicken embryo, inhibition of respiration but not glycolysis alters segmentation clock oscillations[21]. We thus partially impaired the electron transport chain (ETC) in human PSM cells using inhibitors at sub-lethal concentrations, and measured the effect on the segmentation clock (Extended Data Fig. 4f). Treatment with inhibitors of ETC complexes I (rotenone), II (atpenin A5), III (antimycin A) and IV (sodium azide) (Fig. 3a), led to a decrease in basal respiration of more than 50% (control: 100 ± 21.6%, 20 nM rotenone: 41.5 ± 8.3%, 50 nM atpenin: 44.9 ± 9.6%, 100 nM antimycin A: 20.4 ± 6.4%, 1 mM sodium azide: 9.5 ± 3% of control, $P < 0.0001$ in all cases) (Extended Data Fig. 5a). These inhibitors led to premature arrest of segmentation clock oscillations (number of oscillations in 25 h—control: 5.3 ± 0.6, 20 nM rotenone: 3.5 ± 0.5, 50 nM atpenin: 3.5 ± 0.8, 100 nM antimycin A: 3.1 ± 0.3, 1 mM sodium azide: 3.2 ± 0.6, $P < 0.001$ in all cases) with variable effects on oscillation amplitude (Extended Data Fig. 5b,c,e–h,q–t). We observed a significant increase in the segmentation clock period (control: 4.86 ± 0.36 h, 20 nM rotenone: 5.56 ± 0.31 h, 50 nM atpenin: 5.66 ± 0.48 h, 100 nM antimycin A: 6.05 ± 0.31 h, 1 mM sodium azide: 6.57 ± 0.42 h, $P < 0.0001$ in all cases) (Fig. 3b, Extended Data Fig. 5d,k–n and Supplementary Video 5). As ETC impairment leads to cell cycle arrest[25], we could not measure cell cycle length. Thus, decreasing the metabolic rate can decrease the clock period.

ETC activity builds up a proton gradient across the inner mitochondrial membrane that powers oxidative phosphorylation. Inhibiting ATP synthase with oligomycin led to premature arrest of oscillations (number of oscillations in 25 h—5.3 ± 0.6 versus 3.6 ± 1, $P < 0.0001$) and reduced the oscillation amplitude (99.7 ± 29.4% versus 42.9 ± 11.6% of control, $P < 0.0001$) (Extended Data Fig. 5b,c,i,u). Surprisingly, this did not alter the period (4.86 ± 0.36 h versus 4.76 ± 0.45 h, $P = 0.8541$) (Fig. 3b and Extended Data Fig. 5d,o), despite a significant reduction of OCR (100 ± 21.6% versus 56.7 ± 22.8% of control, $P < 0.001$) (Extended Data Fig. 5a). Treatment with the ionophore FCCP decreased $\Delta\Psi_m$ (fluorescence ratio—0.99 ± 0.02 versus 0.11 ± 0.01, $P < 0.0001$), uncoupling ETC activity from ATP production (Extended Data Fig. 5w). In cells treated with 1 μM FCCP for 24 h, oxygen consumption levels were indistinguishable from those in control cells (100 ± 21.6% versus 99.5 ± 17.2% of control, $P > 0.999$), representing entirely leak respiration (Extended Data Fig. 5a). FCCP-treated cells did not show premature arrest of oscillations (number of oscillations in 25 h—5.3 ± 0.6 versus 5.1 ± 4, $P = 0.968$) but displayed decreased amplitude (99.7 ± 29.4% versus 61.9 ± 15% of control, $P = 0.0047$) (Extended Data Fig. 5b,c,j,v). FCCP did not affect the clock period (4.86 ± 0.36 h versus 4.68 ± 0.59 h, $P = 0.1849$) (Fig. 3b and Extended Data Fig. 5d,p). Thus, ETC activity—rather than oxidative phosphorylation—is involved in controlling the segmentation clock period.

These results suggested that cellular ATP levels are not involved in regulating the clock period. Indeed, the ADP/ATP ratio was higher in mouse PSM cells than in human cells (0.42 ± 0.06 versus 0.22 ± 0.03, $P < 0.0001$) (Extended Data Fig. 4d), suggesting that an increased cellular energy charge does not mediate the accelerated developmental rate of mouse cells. To test this hypothesis, we cultured human PSM cells under conditions of increasing cellular ATP concentration. First, we supplemented the medium with succinate to directly feed the ETC at complex II. Second, we replaced glucose with galactose in the medium to increase the reliance on oxidative phosphorylation for ATP production. Third, we treated the cells with the pyruvate dehydrogenase kinase (PDK) inhibitor dichloroacetate (DCA) to increases the conversion of pyruvate to acetyl-CoA for consumption by the TCA cycle (Extended Data Fig. 6a). Under all three conditions, ATP levels increased (control: 0.005826 ± 0.00027 μg, 25 mM succinate: 0.006776 ± 0.00027 μg, 10 mM galactose: 0.007315 ± 0.00009 μg, 6.25 mM DCA: 0.006778 ± 0.00036 μg ATP per well, $P < 0.0001$ in all cases) (Extended Data Fig. 6b) along with OCR/ECAR ratio (control: 1.757 ± 0.24, 25 mM succinate: 2.03 ± 0.14, $P = 0.0016$, 10 mM galactose: 10.08 ± 1.99, $P < 0.0001$, 6.25 mM DCA: 2.03 ± 0.21, $P = 0.0033$) (Extended Data Fig. 6c–e). Replacement of glucose by galactose decreased ECAR compared with control and other treatments (control: 49.21 ± 4.07 mpH min^{-1} per well, 25 mM succinate: 46.35 ± 1.91 mpH min^{-1} per well, $P = 0.0099$; 10 mM galactose: 7.92 ± 1.06 mpH min^{-1} per well, $P < 0.0001$; 6.25 mM DCA: 31.76 ± 2.66 mpH min^{-1} per well, $P < 0.0001$) (Extended Data Fig. 6e), such that glycolytic ATP production was strongly downregulated (control: 72.04 ± 0.95%, 25 mM succinate: 65.96 ± 0.82%, 10 mM galactose: 16.82 ± 2.37%, 6.25 mM DCA: 67.02 ± 1.5%, $P < 0.0001$ in all cases) (Extended Data Fig. 6f). The clock period in cells treated with succinate, galactose or DCA was moderately lengthened (control: 4.73 ± 0.4 h, 25 mM succinate: 5.07 ± 0.41 h, $P = 0.0111$; 10 mM galactose: 5.28 ± 0.52 h, $P < 0.0001$; 6.25 mM DCA: 5.22 ± 0.38 h, $P < 0.0001$) (Extended Data Fig. 6g–m,q). Although the amplitude of oscillations was decreased in galactose and DCA-treated cells (control: 99.59 ± 19.6%, 25 mM succinate: 81.67 ± 17.9%, $P = 0.0715$; 10 mM galactose: 67.45 ± 18.5%, $P = 0.0018$; 6.25 mM DCA: 79.29 ± 16.6% of control, $P = 0.0347$) (Extended Data Fig. 6n–p,r), oscillations persisted normally (number of oscillations in 25 h—control: 5.26 ± 0.4, 25 mM succinate: 5 ± 0, $P = 0.2647$; 10 mM galactose: 5 ± 0, $P = 0.3537$; 6.25 mM DCA: 5.25 ± 0.4, $P = 0.9999$) (Extended Data Fig. 6s). Cell cycle length was also increased (control: 20.84 ± 3.1 h, 25 mM succinate: 23.04 ± 3.8 h, $P = 0.0105$; 10 mM galactose: 28.66 ± 3.7 h, $P < 0.0001$; 6.26 mM DCA: 23.66 ± 2.9 h, $P = 0.0024$) (Extended Data Fig. 6t). Together, these results confirmed that higher ATP concentrations do not promote faster oscillations or proliferation.

NAD$^+$/NADH regulates the clock period

In cancer cells, PDK inhibition also decreases cellular proliferation[26]. This activates pyruvate dehydrogenase, shunting pyruvate away from lactate dehydrogenase (LDH), leading to a lower NAD$^+$/NADH ratio (Extended Data Fig. 6a). Additionally, complex I of the ETC cannot sufficiently regenerate cellular NAD$^+$ because the inner mitochondrial membrane becomes hyperpolarized and opposes the pumping of additional protons. Supplementing cells with pyruvate, which can be rapidly reduced by LDH to generate NAD$^+$, rescues the proliferation rate of cells treated with a PDK inhibitor[26]. Restoring ETC activity by dissipating the increased $\Delta\Psi_m$ with uncoupling agents such as FCCP rescues the NAD$^+$/NADH ratio and proliferation rate[26]. A similar mechanism may be responsible for the increased segmentation clock period in PSM cells subjected to PDK inhibition. We observed significantly lower total NAD$^+$/NADH ratio (11.59 ± 0.7 versus 9.63 ± 0.5, $P = 0.0003$) (Extended Data Fig. 7a) and increased $\Delta\Psi_m$ (0.99 ± 0.02

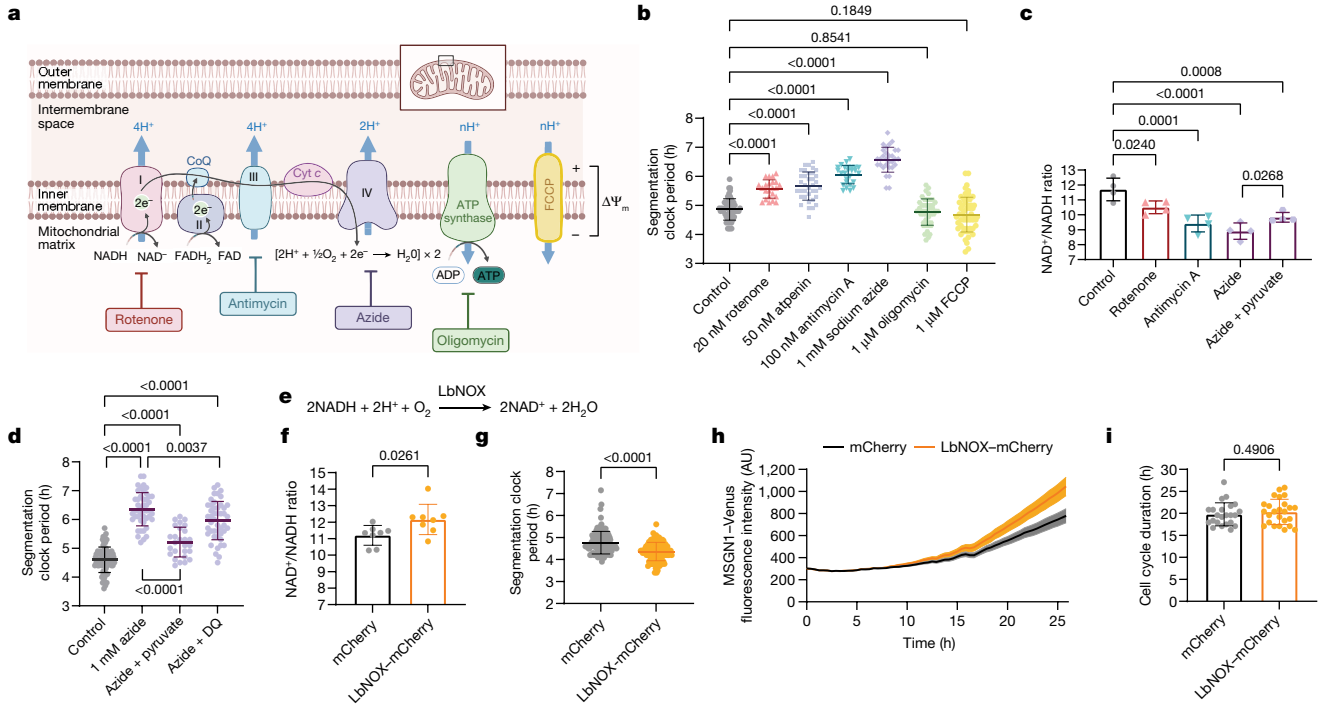

Fig. 3 | Regulation of the segmentation clock by the NAD$^+$/NADH ratio. **a**, ETC and relevant small molecule inhibitors. Adapted from BioRender.com (2021). Cyt *c*, cytochrome *c*. **b**, The HES7-Achilles oscillatory period in human PSM cells treated with DMSO control ($n = 53$), 20 nM rotenone ($n = 23$), 50 nM atpenin A5 ($n = 36$), 100 nM antimycin A ($n = 26$), 1 mM sodium azide ($n = 30$), 1 μM oligomycin ($n = 44$) or 1 μM FCCP ($n = 55$) for 24 h. Data are mean ± s.d. One-way ANOVA with Šidák correction. Rotenone, $P = 1.1 \times 10^{-8}$; atpenin, $P = 6.4 \times 10^{-14}$; antimycin, $P = 1.85 \times 10^{-23}$; azide, $P = 1.88 \times 10^{-42}$. **c**, Whole-cell NAD$^+$/NADH ratio in human PSM cells treated with DMSO control, 20 nM rotenone, 100 nM antimycin A, 1 mM sodium azide and 1 mM sodium azide with 1 mM sodium pyruvate for 24 h. Data are mean ± s.d. $n = 4$ biological replicates. One-way ANOVA with Dunnett correction. Control versus azide, $P = 1.1 \times 10^{-5}$. **d**, The HES7-Achilles oscillatory period in human PSM cells treated with DMSO control ($n = 67$), 1 mM sodium azide alone ($n = 46$), azide with 1 mM sodium pyruvate ($n = 27$) or azide with 5 μM duroquinone (DQ) ($n = 46$). Data are mean ± s.d. One-way ANOVA with Tukey's correction. Control versus azide, $P = 7.4 \times 10^{-14}$; control versus azide + pyruvate, $P = 1.2 \times 10^{-5}$; control versus azide + duroquinone, $P = 7.5 \times 10^{-14}$; azide versus azide + pyruvate, $P = 1.4 \times 10^{-13}$. **e**, NADH oxidation reaction catalysed by *Lb*NOX[28]. **f**, Whole-cell NAD$^+$/NADH ratio in human PSM cells transduced with a lentivirus expressing either mCherry alone or *Lb*NOX with mCherry. Data are mean ± s.d. $n = 8$ biological replicates. Unpaired two-sided *t*-test. **g**, HES7-Achilles oscillatory period in human PSM cells transduced with a lentivirus expressing either mCherry alone ($n = 113$) or *Lb*NOX with mCherry ($n = 116$). Data are mean ± s.d. Unpaired two-sided *t*-test: $P = 3.7 \times 10^{-10}$. **h**, MSGN1-Venus fluorescence during days 1–2 of human PSM differentiation, transduced with a lentivirus expressing either mCherry alone or *Lb*NOX with mCherry. Data are mean ± s.e.m. $n = 7$ biological replicates. **i**, Cell cycle length in human PSM cells transduced with a lentivirus expressing either mCherry alone ($n = 23$) or *Lb*NOX with mCherry ($n = 25$). Data are mean ± s.d. Unpaired two-sided *t*-test.

versus 1.12 ± 0.05, $P = 0.038$) (Extended Data Fig. 7b) in PSM cells treated with 6.25 mM DCA. The NAD$^+$/NADH ratio could be restored to control levels by pyruvate supplementation or FCCP treatment (control: 11.59 ± 0.7, DCA + pyruvate: 12.4 ± 0.09, $P = 0.084$; DCA + 10 nM FCCP: 12.02 ± 0.3, $P = 0.4634$) (Extended Data Fig. 7a).

These total NAD$^+$/NADH ratio measurements included both mitochondrial and cytoplasmic NAD(H) pools. We generated a human PSC line carrying the fluorescent sensor Peredox, which exhibits increased fluorescence when cytoplasmic—but not mitochondrial—levels of NADH are increased[27] (Extended Data Fig. 7c,d). Using this reporter line, we confirmed the changes in cytosolic NAD$^+$/NADH ratio upon DCA treatment and its restoration by pyruvate and FCCP (Peredox/mCherry ratio—control: 1.053 ± 0.04, DCA: 1.114 ± 0.02, $P = 0.0074$; DCA + pyruvate: 1.08 ± 0.01, $P = 0.2425$; DCA + 10 nM FCCP: 1.07 ± 0.02, $P = 0.6327$) (Extended Data Fig. 7e). Of note, the clock period in DCA-treated cells was fully rescued by both pyruvate and FCCP (control: 4.63 ± 0.4 h, DCA: 4.9 ± 0.4 h, $P = 0.0001$; DCA + pyruvate: 4.53 ± 0.3 h, $P = 0.5455$; DCA + 10 nM FCCP: 4.77 ± 0.4 h, $P = 0.0927$) (Extended Data Fig. 7f). Thus, the segmentation clock period depends on NAD$^+$ availability rather than on ATP supply. A similar mechanism may underlie the extended segmentation clock period when supplementing with succinate. Succinate supplementation increased $\Delta\Psi_m$ (2.044 ± 0.11 versus 2.465 ± 0.19, $P = 0.0341$) (Extended Data Fig. 7g) and reduced the total NAD$^+$/NADH ratio, which could be rescued by pyruvate (control: 9.65 ± 0.25, succinate: 8.26 ± 0.68, $P = 0.024$; succinate + pyruvate: 8.94 ± 0.44, $P = 0.2126$) (Extended Data Fig. 7h). Normalization of the NAD$^+$/NADH ratio by pyruvate supplementation in succinate-treated cells fully rescued the oscillatory period (control: 4.47 ± 0.5 h, succinate: 4.76 ± 0.5 h, $P = 0.017$; succinate + pyruvate: 4.58 ± 0.6 h, $P = 0.5299$) (Extended Data Fig. 7i).

Impaired ETC activity also decreases the NAD$^+$/NADH ratio, because NAD$^+$ regeneration by complex I is altered. In cells treated with complex I, III and IV inhibitors, we observed a significant decrease in the NAD$^+$/NADH ratio (control: 11.7 ± 0.7, 20 nM rotenone: 10.5 ± 0.4, $P = 0.0240$; 100 nM antimycin A: 9.4 ± 0.5, $P = 0.0001$; 1 mM sodium azide: 8.9 ± 0.5, $P < 0.0001$) (Fig. 3c) with increased Peredox fluorescence (Peredox/mCherry ratio—control: 0.947 ± 0.05, 20 nM rotenone: 1.18 ± 0.02, 100 nM antimycin A: 1.22 ± 0.01, 1 mM sodium azide: 1.35 ± 0.02, $P < 0.0001$ in all cases) (Extended Data Fig. 7j). Pyruvate supplementation of azide-treated cells partially restored the NAD$^+$/NADH ratio[28] (total NAD$^+$/NADH: 8.9 ± 0.5 versus 9.8 ± 0.3, $P = 0.0268$; Peredox/mCherry: 1.35 ± 0.02 versus 1.20 ± 0.01, $P < 0.0001$) (Fig. 3c and Extended Data Fig. 7j) and the clock period (6.3 ± 0.6 h versus 5.2 ± 0.5 h, $P < 0.0001$) (Fig. 3d, Extended Data Fig. 7k and Supplementary Video 5). We also supplemented azide-treated cells with duroquinone, which can mediate NAD$^+$ regeneration via the quinone oxidase NQO1[29].

Duroquinone treatment led to modest recovery of the cytoplasmic NAD^+/NADH ratio as measured by Peredox fluorescence (Peredox/mCherry ratio—1.35 ± 0.02 versus 1.27 ± 0.01, $P < 0.0001$) (Extended Data Fig. 7j), but the total NAD^+/NADH ratio did not increase (6.63 ± 0.2 versus 6.60 ± 0.5, $P = 0.999$) (Extended Data Fig. 7l). Nevertheless, clock oscillations were slightly but significantly accelerated in azide and duroquinone-treated cells relative to cells treated with azide alone (clock period 6.35 ± 0.6 h versus 5.96 ± 0.6 h, $P = 0.0037$) (Fig. 3d and Extended Data Fig. 7m). This is consistent with ETC inhibition slowing the segmentation clock by impairing NAD(H) redox homeostasis.

Our results suggested that differences in the NAD(H) redox balance may underlie the developmental rate differences between mouse and human cells. NAD^+ is used as an electron acceptor in many metabolic reactions and is required for key steps in nucleotide synthesis and in central carbon, amino acid and lipid metabolism[30]. We compared the NAD^+/NADH ratio in mouse with that in human PSM cells and found that, contrary to our expectations, the total NAD^+/NADH ratio was significantly lower in mouse (6.81 ± 0.3 versus 9.66 ± 0.4, $P < 0.0001$) (Extended Data Fig. 4e). However, the marked difference in mitochondrial content between mouse and human PSM cells confounded this whole-cell NAD^+/NADH measurement as mitochondria exhibit much lower NAD^+/NADH values relative to cytoplasm[31,32]. Our measurements of total NAD^+/NADH ratio therefore most probably reflected the higher mitochondrial density of mouse cells compared with human cells. We therefore measured the extracellular lactate/pyruvate ratio[31], a proxy for cytoplasmic NADH/NAD^+. This ratio was more than twofold higher in human than mouse PSM cells (25.1 ± 1.8 versus 66.7 ± 17.4, $P < 0.0001$) (Fig. 2j), suggesting that the cytosolic NAD^+/NADH redox balance scales with developmental rate.

We next inhibited LDH in human PSM cells with sodium oxamate to prevent NAD^+ regeneration. This led to a decreased NAD^+/NADH ratio (total NAD^+/NADH: 11.19 ± 1.3 versus 8.12 ± 0.3, $P = 0.0002$; Peredox/mCherry: 0.6 ± 0.01 versus 0.78 ± 0.01, $P < 0.0001$) (Extended Data Fig. 8a,b) and concomitant increase in clock period (4.75 ± 0.5 h versus 5.04 ± 0.3 h, $P = 0.0404$) (Extended Data Fig. 8c–f). Oscillations displayed normal amplitude (Extended Data Fig. 8g) but occasionally arrested early (number of oscillations in 25 h—5.2 ± 0.4 versus 4.6 ± 0.5, $P = 0.0406$) (Extended Data Fig. 8h). Thus, directly lowering the cytosolic NAD^+/NADH ratio could slow down the segmentation clock tempo.

*Lb*NOX[28] can be expressed in mammalian cells to drive the regeneration of NAD^+ from NADH with concomitant reduction of oxygen to water (Fig. 3e). We used lentiviruses to express either mCherry or cytosolic *Lb*NOX together with mCherry in human PSM cells (Extended Data Fig. 8i). *Lb*NOX modestly increased the total NAD^+/NADH ratio (11.20 ± 0.6 versus 12.16 ± 0.9, $P = 0.0261$) (Fig. 3f). We could not measure Peredox fluorescence ratios owing to the spectral overlap with mCherry. However, we confirmed *Lb*NOX activity by measuring non-mitochondrial oxygen consumption, which was increased owing to oxygen reduction by *Lb*NOX (fraction of basal OCR—0.25 ± 0.04 versus 0.36 ± 0.02, $P < 0.0001$) (Extended Data Fig. 8j). When we transduced HES7-Achilles reporter cells with *Lb*NOX–mCherry, we observed a clock period decrease by approximately 25 min each cycle (4.76 ± 0.5 h versus 4.36 ± 0.4 h, $P < 0.0001$) (Fig. 3g, Extended Data Fig. 8k–m and Supplementary Video 6). The oscillation amplitude was not affected (14.3 ± 2.9 AU versus 12.5 ± 3.4 AU, $P = 0.1196$) (Extended Data Fig. 8n,o), and there was an increase in the mean number of oscillations observed in 25 h (5.6 ± 0.5 versus 6 ± 0, $P = 0.0092$) (Extended Data Fig. 8p). *Lb*NOX–mCherry also accelerated the induction dynamics of the MSGN1-Venus reporter relative to mCherry alone (rate of growth (k)—mCherry: 0.048 AU, 95% confidence interval 0.04561 to 0.05064 AU versus *Lb*NOX–mCherry: 0.06438 AU, 95% confidence interval 0.06140 to 0.06742 AU, $P < 0.0001$) (Fig. 3h). Cell cycle length was not different between cells transduced with *Lb*NOX-mCherry or mCherry alone (19.78 ± 2.6 h versus 20.33 ± 2.8 h, $P = 0.4906$) (Fig. 3i). Thus, modulation of the NAD^+/NADH ratio can slow down or accelerate the segmentation clock.

The ETC effect is mediated by translation

Increased mitochondrial activity is correlated with faster transcription, faster translation and accelerated growth in human cell lines[33–35]. We compared translation rates by pulsing PSM cells with puromycin for 1 h. We then measured the amount of puromycilated peptides produced[36,37] (Fig. 4a). The mass-specific translation rate was almost twice as high in mouse PSM cells as in human cells (antibody: 28.95 ± 1.3 MFI pg^{-1} versus 19.15 ± 1.4 MFI pg^{-1}, $P = 0.001$; click-it: 13.01 ± 1.1 MFI pg^{-1} versus 7.44 ± 0.3 MFI pg^{-1}, $P = 0.011$) (Fig. 4b and Extended Data Fig. 9a). Slowing down translation by treating human PSM cells with low doses of cycloheximide (CHX) increased the clock period (control: 4.92 ± 0.3 h, 40 nM CHX: 5.43 ± 0.5 h, $P = 0.0001$; 80 nM CHX: 5.49 ± 0.3 h, $P = 0.0007$; 160 nM CHX: 5.58 ± 0.3 h, $P < 0.0001$) with little effect on oscillation number or amplitude (Fig. 4c, Extended Data Fig. 9b–h and Supplementary Video 7). Cell cycle length was also increased by CHX treatment (20.89 ± 3.1 h versus 25.17 ± 3.6 h, $P < 0.0001$) (Fig. 4d). Thus, the global translation rate could potentially control developmental rate, although this effect could also be mediated by a subset of specific transcripts whose translation is slowed by CHX.

We observed that rotenone, antimycin A and sodium azide all decreased the translation rate (control: 100.0 ± 4.2%, 20 nM rotenone: 85.7 ± 8.8%, $P = 0.0354$; 100 nM antimycin A: 60.8 ± 3.8%, $P < 0.0001$; 1 mM sodium azide: 49.5 ± 4.8% of control, $P < 0.0001$) (Fig. 4e). Supplementing azide-treated cultures with pyruvate partially rescued the translation rate (49.5 ± 4.8% versus 65.9 ± 5.0% of control, $P = 0.0153$) (Fig. 4e). Cultures treated with sodium azide for 1 h displayed reduced translation, indicating rapid downregulation of protein synthesis (39,851 ± 2,298 MFI versus 30,262 ± 5,267 MFI, $P = 0.0446$) (Extended Data Fig. 9i). These results suggested that ETC inhibition and NAD^+ depletion can slow down the segmentation clock in part by reducing protein translation. Transduction with *Lb*NOX-mCherry also significantly increased puromycin incorporation over mCherry (23,601 ± 3,167 MFI versus 30,953 ± 1,646 MFI, $P = 0.0062$) (Fig. 4f). We performed Seahorse assays in human PSM cells treated with CHX. All aspects of respiration were indistinguishable between CHX-treated and control cells (Extended Data Fig. 9j–l). Thus, mitochondrial activity acts upstream of translation rate to control the segmentation clock period.

Differences in global protein stability also correlate with species-specific developmental rates. Proteome half-life is two times shorter in mouse neural progenitors compared to human[2]. We found that the half-life of puromycilated peptides was shorter in mouse compared with human PSM cells (2.23 ± 0.63 h versus 4.46 ± 1.47 h, $P < 0.0001$) (Extended Data Fig. 10a). Mass-specific proteasome activity was significantly higher in mouse PSM cells (2,323 ± 259 RLU pg^{-1} versus 1,446 ± 34 RLU pg^{-1}, $P = 0.0005$) (Fig. 4g), suggesting that reduced protein stability is caused by higher proteasome activity.

Inhibiting proteasome function can lead to disruption of segmentation clock oscillations[38]. Treating human PSM cells with low doses of the proteasome inhibitors bortezomib or lactacystin caused premature arrest of oscillations (number of oscillations in 25 h—control: 5.17 ± 0.39, 2.5 nM bortezomib: 5.50 ± 0.54, $P = 0.459$; 5 nM bortezomib: 2.69 ± 0.63, $P \leq 0.0001$; 10 nM bortezomib: 2.16 ± 0.38, $P < 0.0001$; 1 μM lactacystin: 4.77 ± 0.44, $P = 0.1635$) but did not change the oscillatory period (control: 4.98 ± 0.5 h, 2.5 nM bortezomib: 4.8 ± 0.5 h, $P = 0.4348$; 5 nM bortezomib: 5.00 ± 0.5 h, $P = 0.9999$; 10 nM bortezomib: 4.62 ± 0.5 h, $P = 0.1223$; 1 μM lactacystin: 5.10 ± 0.6 h, $P = 0.8501$) despite significant inhibition of proteasome activity (control: 2,257,774 ± 122,326 RLU, 2.5 nM bortezomib: 1,707,326 ± 63,125 RLU, 5 nM bortezomib: 1,590,243 ± 122,000 RLU, 10 nM bortezomib: 1,309,836 ± 102,240 RLU,

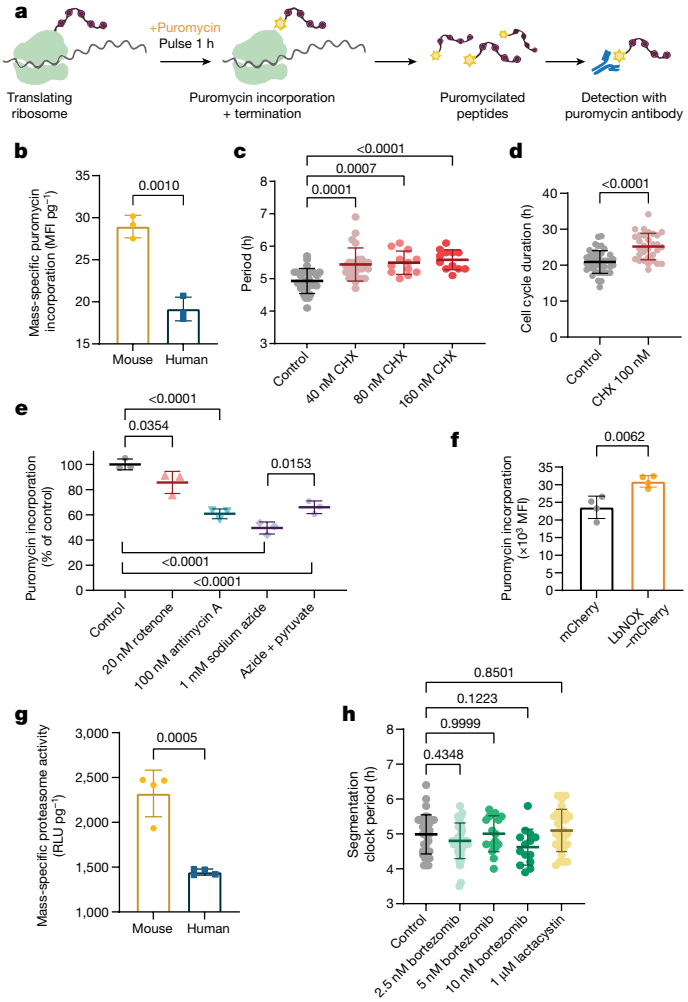

Fig. 4 | The global rate of protein synthesis acts downstream of the ETC to regulate developmental speed. a, Experimental approach to measure global protein synthesis by detection of puromycylated peptides following a 1-h pulse with puromycin. Created with BioRender.com. **b**, Mass-specific global translation rate as measured by puromycin incorporation in MSGN1-Venus$^+$ PSC-derived mouse and human PSM cells immediately after a 1-h puromycin pulse and detection by directly conjugated AlexaFluor647 anti-puromycin antibody. Data are mean ± s.d. $n = 3$ biological replicates. Unpaired two-sided *t*-test. **c**, Period of HES7-Achilles oscillations in human PSM cells treated with vehicle control (DMSO, $n = 27$) or increasing doses of CHX (40 nM, $n = 24$; 80 nM, $n = 12$; 160 nM, $n = 12$). Data are mean ± s.d. One-way ANOVA with Dunnett's correction: control versus 160 nM CHX, $P = 7.1 \times 10^{-5}$. **d**, Duration of the cell cycle in control (DMSO-treated; $n = 42$) human PSM cells and cells treated with 100 nM CHX ($n = 31$). Data are mean ± s.d. Unpaired two-sided *t*-test, $P = 1.1 \times 10^{-6}$. **e**, Relative translation rate expressed as puromycin incorporation normalized to control (DMSO treatment) in human PSM cells treated with 20 nM rotenone, 100 nM antimycin A, 1 mM sodium azide or azide with 1 mM sodium pyruvate for 24 h. Data are mean ± s.d. $n = 3$ biological replicates. One-way ANOVA with Šidák correction. Control versus antimycin, $P = 2.8 \times 10^{-5}$; control versus azide, $P = 2.8 \times 10^{-6}$; control versus azide + pyruvate, $P = 9.6 \times 10^{-5}$. **f**, Global translation rate as measured by puromycin incorporation in human PSM cells transduced with a lentivirus expressing either mCherry alone or *Lb*NOX with mCherry. Data are mean ± s.d. $n = 4$ biological replicates. Unpaired two-sided *t*-test. **g**, Mass-specific proteasome activity in MSGN1-Venus$^+$ PSC-derived mouse and human PSM cells as measured by cleavage of a luminogenic proteasome substrate. Data are mean ± s.d. $n = 4$ biological replicates. Unpaired two-sided *t*-test. **h**, The period of HES7-Achilles oscillations in human PSM cells treated with DMSO control ($n = 35$), 2.5 nM ($n = 37$), 5 nM ($n = 17$) or 10 nM ($n = 14$) bortezomib, or 1 μM lactacystin ($n = 30$). Data are mean ± s.d. One-way ANOVA with Dunnett's correction.

1 μM lactacystin: 1,536,581 ± 195,052 RLU, $P < 0.0001$ in all cases) (Fig. 4h, Extended Data Fig. 10b–l and Supplementary Video 8). The cell cycle duration could not be assessed under these conditions, as proteasome inhibitors induce cell cycle arrest[39].

Neither azide nor antimycin treatment reduced the proteasome activity (control: 2,082,679 ± 23,055 RLU, 100 nM antimycin A: 2,452,103 ± 30,891 RLU, 1 mM sodium azide: 2,778,603 ± 37,391 RLU, $P < 0.0001$ in both cases) or increased the stability of puromycylated peptides (Extended Data Fig. 10j,k). To assess the degradation profile of the full-length proteome, we performed pulse-chase experiments with the methionine analogue L-azidohomoalanine (AHA). Unlike puromycin, AHA incorporation into growing peptides does not induce chain termination and thus labels full-length proteins. AHA labelling resulted in indistinguishable decay profiles between control and azide-treated cells over the timeframe relevant to segmentation clock oscillations (Extended Data Fig. 10l). Together, these experiments suggest that the segmentation clock period is more sensitive to inhibition of protein production than to degradation.

Discussion

In summary, we found that mass-specific respiration rates scale with and regulate the segmentation clock period by modulating NAD(H) redox balance and, further downstream, translation rate. Given that the segmentation clock period can be used as a proxy for developmental rate[1], our results may explain—at least in part—the temporal differences observed at early stages of mouse and human development. Such a mechanism may also be modulated locally in the embryo to generate heterochronic changes, as seen for instance in the acceleration of the segmentation clock period relative to growth rate in snakes[40]. Additional studies in other embryonic cell types and mammalian species are required to assess the generality of our findings. Our results also suggest that mass-specific metabolic rates for embryonic cell types may scale with adult body mass as predicted by Kleiber's law, even under uniform culture conditions[23]. Our studies also reveal a striking parallel between the metabolic requirements of cancer cell proliferation and those of the segmentation clock[41]. In both cases, NAD^+ redox homeostasis is more important than ATP availability for maintaining normal growth and oscillation rates[26]. Given that PSM cells exhibit Warburg-like metabolism with high levels of aerobic glycolysis[21], these similarities further strengthen the notion that cancer cells resemble embryonic progenitors.

Moreover, the finding that the segmentation clock period is sensitive to NAD^+ levels draws a parallel between developmental rate and aging. NAD^+ levels decrease progressively with age and restoring NAD^+ levels can ameliorate aging-associated phenotypes[42]. The aging process and developmental rate may share some regulatory mechanisms, especially given that lifespan and gestation period are positively correlated[43]. Future work should focus on the identification of factors that can modulate mass-specific respiration rates in vertebrates[23]. Ultimately, interspecific differences in developmental rate must be traceable to genetic causes. Finally, the implication of translation rate downstream of mitochondrial activity strongly suggests that the integrated stress response may have a role in determining the developmental rate[44,45]. Continued research in this area will reveal how developmental time can be manipulated externally, with important applications in human stem cell therapy and in vitro disease modelling.

Online content

Any methods, additional references, Nature Portfolio reporting summaries, source data, extended data, supplementary information, acknowledgements, peer review information; details of author contributions and competing interests; and statements of data and code availability are available at https://doi.org/10.1038/s41586-022-05574-4.

1. Matsuda, M. et al. Species-specific segmentation clock periods are due to differential biochemical reaction speeds. *Science* **369**, 1450 (2020).
2. Rayon, T. et al. Species-specific pace of development is associated with differences in protein stability. *Science* **369**, eaba7667 (2020).
3. Hoyle, N. P. & Ish-Horowicz, D. Transcript processing and export kinetics are rate-limiting steps in expressing vertebrate segmentation clock genes. *Proc. Natl Acad. Sci. USA* **110**, E4316–E4324 (2013).
4. Stearns, S. C. The evolution of life history traits: a critique of the theory and a review of the data. *Annu. Rev. Ecol. Syst.* **8**, 145–171 (1977).
5. Ricklefs, R. E. Embryo development and ageing in birds and mammals. *Proc. Biol. Sci.* **273**, 2077–2082 (2006).
6. Blagosklonny, M. V. Big mice die young but large animals live longer. *Aging* **5**, 227–233 (2013).
7. Otis, E. M. & Brent, R. Equivalent ages in mouse and human embryos. *Anat. Rec.* **120**, 33–63 (1954).
8. Schröter, C. et al. Dynamics of zebrafish somitogenesis. *Dev. Dyn.* **237**, 545–553 (2008).
9. Pourquié, O. Vertebrate segmentation: from cyclic gene networks to scoliosis. *Cell* **145**, 650–663 (2011).
10. Hubaud, A. & Pourquie, O. Signalling dynamics in vertebrate segmentation. *Nat. Rev. Mol. Cell Biol.* **15**, 709–721 (2014).
11. Diaz-Cuadros, M. et al. In vitro characterization of the human segmentation clock. *Nature* **580**, 113–118 (2020).
12. Matsuda, M. et al. Recapitulating the human segmentation clock with pluripotent stem cells. *Nature* **580**, 124–129 (2020).
13. Chu, L. F. et al. An in vitro human segmentation clock model derived from embryonic stem cells. *Cell Rep.* **28**, 2247–2255.e5 (2019).
14. Matsumiya, M. et al. ES cell-derived presomitic mesoderm-like tissues for analysis of synchronized oscillations in the segmentation clock. *Development* **145**, dev156836 (2018).
15. Hubaud, A. et al. Excitable dynamics and Yap-dependent mechanical cues drive the segmentation clock. *Cell* **171**, 668–682.e11 (2017).
16. Johnson, M. H. & Day, M. L. Egg timers: how is developmental time measured in the early vertebrate embryo? *Bioessays* **22**, 57–63 (2000).
17. Kleiber, M. Body size and metabolic rate. *Physiol. Rev.* **27**, 511–541 (1947).
18. Martin, R. D., Genoud, M. & Hemelrijk, C. K. Problems of allometric scaling analysis: examples from mammalian reproductive biology. *J. Exp. Biol.* **208**, 1731–1747 (2005).
19. Feijó Delgado, F. et al. Intracellular water exchange for measuring the dry mass, water mass and changes in chemical composition of living cells. *PLoS ONE* **8**, e67590 (2013).
20. Miettinen, T. P. et al. Single-cell monitoring of dry mass and dry mass density reveals exocytosis of cellular dry contents in mitosis. *eLife* **11**, e76664 (2022).
21. Oginuma, M. et al. A gradient of glycolytic activity coordinates FGF and Wnt signaling during elongation of the body axis in amniote embryos. *Dev. Cell* **40**, 342–353.e10 (2017).
22. Bulusu, V. et al. Spatiotemporal analysis of a glycolytic activity gradient linked to mouse embryo mesoderm development. *Dev. Cell* **40**, 331–341.e4 (2017).
23. Porter, R. K. Allometry of mammalian cellular oxygen consumption. *Cell. Mol. Life Sci.* **58**, 815–822 (2001).
24. Porter, R. K., Hulbert, A. J. & Brand, M. D. Allometry of mitochondrial proton leak: influence of membrane surface area and fatty acid composition. *Am. J. Physiol.* **271**, R1550–R1560 (1996).
25. Harris, M. Pyruvate blocks expression of sensitivity to antimycin A and chloramphenicol. *Somatic Cell Genet.* **6**, 699–708 (1980).
26. Luengo, A. et al. Increased demand for NAD^+ relative to ATP drives aerobic glycolysis. *Mol. Cell* **81**, 691–707.e6 (2021).
27. Hung, Y. P. et al. Imaging cytosolic NADH–NAD^+ redox state with a genetically encoded fluorescent biosensor. *Cell Metab.* **14**, 545–554 (2011).
28. Titov, D. V. et al. Complementation of mitochondrial electron transport chain by manipulation of the NAD^+/NADH ratio. *Science* **352**, 231–235 (2016).
29. Merker, M. P. et al. Influence of pulmonary arterial endothelial cells on quinone redox status: effect of hyperoxia-induced NAD(P)H:quinone oxidoreductase 1. *Am. J. Physiol.* **290**, L607–L619 (2006).
30. Fessel, J. P. & Oldham, W. M. Pyridine dinucleotides from molecules to man. *Antioxid. Redox Signal.* **28**, 180–212 (2017).
31. Williamson, D. H., Lund, P. & Krebs, H. A. The redox state of free nicotinamide-adenine dinucleotide in the cytoplasm and mitochondria of rat liver. *Biochem. J.* **103**, 514–527 (1967).
32. Veech, R. L., Guynn, R. & Veloso, D. The time-course of the effects of ethanol on the redox and phosphorylation states of rat liver. *Biochem. J.* **127**, 387–397 (1972).
33. das Neves, R. P. et al. Connecting variability in global transcription rate to mitochondrial variability. *PLoS Biol.* **8**, e1000560 (2010).
34. Johnston, I. G. et al. Mitochondrial variability as a source of extrinsic cellular noise. *PLoS Comput. Biol.* **8**, e1002416 (2012).
35. Guantes, R. et al. Global variability in gene expression and alternative splicing is modulated by mitochondrial content. *Genome Res.* **25**, 633–644 (2015).
36. Hidalgo San Jose, L. & Signer, R. A. J. Cell-type-specific quantification of protein synthesis in vivo. *Nat. Protoc.* **14**, 441–460 (2019).
37. Schmidt, E. K. et al. SUnSET, a nonradioactive method to monitor protein synthesis. *Nat. Methods* **6**, 275–277 (2009).
38. Bessho, Y. et al. Periodic repression by the bHLH factor Hes7 is an essential mechanism for the somite segmentation clock. *Genes Dev.* **17**, 1451–1456 (2003).
39. Bonvini, P. et al. Bortezomib-mediated 26S proteasome inhibition causes cell-cycle arrest and induces apoptosis in CD-30^+ anaplastic large cell lymphoma. *Leukemia* **21**, 838–842 (2007).
40. Gomez, C. et al. Control of segment number in vertebrate embryos. *Nature* **454**, 335–339 (2008).
41. Hosios, A. M. & Vander Heiden, M. G. The redox requirements of proliferating mammalian cells. *J. Biol. Chem.* **293**, 7490–7498 (2018).
42. Covarrubias, A. J. et al. NAD^+ metabolism and its roles in cellular processes during ageing. *Nat. Rev. Mol. Cell Biol.* **22**, 119–141 (2021).
43. Fushan, A. A. et al. Gene expression defines natural changes in mammalian lifespan. *Aging Cell* **14**, 352–365 (2015).
44. Bao, X. R. et al. Mitochondrial dysfunction remodels one-carbon metabolism in human cells. *eLife* **5**, e10575 (2016).
45. Mick, E. et al. Distinct mitochondrial defects trigger the integrated stress response depending on the metabolic state of the cell. *eLife* **9**, e49178 (2020).

Methods

Pluripotent stem cell culture

E14 and its derivative reporter lines pMsgn1-Venus[46] and Hes7-Achilles[11] mouse embryonic stem (ES) cells were maintained under feeder-free conditions on gelatin-coated dishes (StemCell Technologies cat. no. 07903) with 2i medium composed of high glucose DMEM (Gibco cat. no. 11965-118) supplemented with 1% GlutaMAX (Gibco cat. no. 35050061), 1% Non-Essential Amino Acids (Gibco cat. no. 11140-050), 1% sodium pyruvate (Gibco cat. no. 11360-070), 0.01% Bovine Serum Albumin (Gibco cat. no. 15260-037), 0.1% β-mercaptoethanol (Gibco cat. no. 21985-023), 15% Fetal Bovine Serum (EMD Millipore cat. no. ES009B), 1,000 U ml^{-1} LIF (EMD Millipore cat. no. ESG1106), 3 μM CHIR 99021 (Tocris cat. no. 4423) and 1 μM PD0325901 (Stemgent cat. no. 04-006). Mouse ES cells were passaged by TrypLE Express (Gibco cat. no. 12605010) dissociation every 2 days at a density of 1×10^4 cells per cm^2.

Human stem cell work was approved by Partners Human Research Committee (protocol no. 2017P000438/PHS). We complied with all relevant ethical regulations. Written informed consent from the donor of the NCRM1 iPS cells was obtained by Rutgers University at the time of sample collection. NCRM1 iPS cells (RUCDR, Rutgers University) and lines carrying the MSGN1-Venus[47], HES7-Achilles[11], HES7-Achilles; pCAG-H2B-mCherry[11] reporters and the AAVS1-CAG-Peredox-mCherry-NLS sensor were maintained on Matrigel-coated plates (Corning, cat. no. 35277) in mTeSR1 medium (StemCell Technologies cat. no. 05851) as previously described[48]. Human iPS cells were passaged every 4–5 days by Accutase (Corning cat. no. 25058CI) dissociation and seeded at a density of 5×10^4 cells per cm^2 in mTeSR1 supplemented with 10 μM Y-27362 dihydrochloride (Rocki; Tocris Bioscience, cat. no. 1254).

Generation of NLS-BFP; Hes7-Achilles mouse ES cell line

To track individual mouse pPSM cells in homo- or hetero-specific co-culture conditions, we integrated a constitutive nuclear label into the Hes7-Achilles mouse ES cell line using the Tol2 system. We used Lipofectamine 3000 (Invitrogen cat. no. L3000001) to co-transfect the following plasmids into Hes7-Achilles mouse ES cells: (1) pCAGGS-Tol2-NLS-BFP-Tol2, (2) pCAGGS-transposase, (3) pMAX-GFP. We isolated GFP$^+$ cells by FACS and plated them at low density on 35-mm gelatin-coated dishes in 2i medium. Note the GFP transfection was transient and only used for selection of successfully transfected cells. After clonal expansion, we visually inspected colonies, manually picked those expressing NLS-BFP and seeded them into individual wells of a 96-well plate. A set of five different clones were verified to stably transmit the CAG-NLS-BFP transgene and used for subsequent experiments.

PSM differentiation

Mouse ES cells were pre-differentiated to an epiblast-like state as previously described[11] by seeding fibronectin-coated dishes (BD Biosciences cat. no. 356008) at a density of 0.8×10^4 cells per cm^2 in NDiff227 medium (Takara cat. no. Y40002) supplemented with 1% KSR (Gibco cat. no. 10828028), 25 ng ml^{-1} Activin A (R&D systems cat. no. 338-AC-050) and 12 ng ml^{-1} bFGF (PeproTech cat. no. 450-33). The medium was refreshed after 24 h. Human iPS cells were seeded on Matrigel-coated plates at a density of 3×10^4 cells per cm^2 in mTeSR1 with 10 μM Rocki. After 24 h, the medium was replaced by mTeSR1 without Rocki.

PSM differentiation was initiated 48 h after initial seeding for both mouse and human PSCs. Cultures were switched to DMEM/F12 GlutaMAX (Gibco cat. no. 10565042) supplemented with 1% Insulin-Transferrin-Selenium (ITS; Gibco cat. no. 41400045), 5% Fetal Bovine Serum (EMD Millipore cat. no. ES009B), 6 μM Chir 99021 (Tocris cat. no. 4423), 20 ng ml^{-1} mouse bFGF (PeproTech cat. no. 450-33) and 30 ng ml^{-1} Activin A (R&D systems cat. no. 338-AC-050). After 24 h, the medium was replaced by DMEM/F12 GlutaMAX with 1% ITS, 5% FBS, 6 μM Chir 99021, 20 ng ml^{-1} bFGF and 0.5 μM LDN193189 (Stemgent cat. no. 04-0074). If PSM cultures needed to be maintained for longer than 2 days, the medium was refreshed at 48 h with DMEM/F12 GlutaMAX, 1% ITS, 5% FBS, 6 μM Chir 99021, 0.5 μM LDN193189, 50 ng ml^{-1} mouse FGF4 (R&D Systems cat. no. 5846-F4-025), 1 μg ml^{-1} Heparin (Sigma Aldrich cat. no. H3393-100KU), 2.5 μM BMS493 (Sigma Aldrich cat. no. B6688-5MG) and 10 μM Rocki to maintain the posterior PSM fate.

For live-imaging experiments, cells were seeded on 24-well glass-bottom plates (In Vitro Scientific cat. no. P24-1.5H-N) on day 0 and cultured in DMEM/F12 without phenol red (Gibco cat. no. 31053028). Whenever the effects of chemical inhibitors or culture conditions on the segmentation clock were tested, human HES7-Achilles or HES7-Achilles; AAVS1-CAG-H2B-mCherry cells were differentiated under serum-free conditions as previously described[11] to avoid confounding factors from FBS composition.

Neural progenitor differentiation

Neural progenitor induction relied on dual Smad inhibition and was adapted from previously described protocols[49]. Mouse ES cells were seeded on fibronectin-coated dishes at a density of 1×10^4 cells per cm^2 and pre-differentiated to epiblast state as described above. Human iPS cells were seeded on Matrigel-coated plates at a density of 3.5×10^4 cells per cm^2 in mTeSR1 with 10 μM Rocki. At 24 h, the medium was replaced by mTeSR1 without Rocki. Two days after initial seeding, both mouse and human cells were switched to NDiff227 supplemented with 1% FBS, 0.1 μM LDN193189, and 10 μM SB431542 (Selleck Chemicals cat. no. S1067). The media was refreshed daily. Mouse cells were cultured for 5 days and human cells for 7 days. Neural progenitor fate was confirmed by PAX6 immunofluorescence as described below.

Immunofluorescence

For immunostaining of 2D cultures, cells were grown on Matrigel-coated 24-well glass-bottom plates (In Vitro Scientific cat. no. P24-1.5H-N). Cells were rinsed in PBS and fixed in a 4% paraformaldehyde solution (Electron Microscopy Sciences cat. no. 15710) for 20 min at room temperature, then washed 3 times with phosphate buffered saline (PBS). Samples were permeabilized by washing three times for three minutes each in Tris buffered saline (TBS) with 0.1% Tween (TBST) and blocked for one hour at room temperature in TBS-0.1% Triton-3% FBS. The primary antibody (Rabbit anti-PAX6, Biolegend cat. no. 901301, lotB277104; rabbit anti-pHistone H3 (Ser10), Santa Cruz cat. no. sc-8656, lot D1615; or rabbit anti-Flag, Cell Signaling Technologies cat. no. 14793S, lot 7) was diluted in blocking solution at 1:350 and incubated overnight at 4 °C with gentle rocking. Following three TBST washes and a 10-min block, cells were incubated with a goat anti-rabbit Alexa Fluor 488-conjugated secondary antibody (Thermo Fisher cat. no. A11034) or goat anti-rabbit Alexa Fluor 594-conjugated secondary antibody (Thermo Fisher cat. no. A-11037) (1:500) and Hoechst33342 (1:1,000) overnight at 4 °C with gentle rocking. Three final TBST washes and a PBS rinse were performed, and cells were mounted in Fluoromount G (Southern Biotech cat. no. 0100-01). Images were acquired using a Zeiss LSM 780 point-scanning confocal microscope with a 20× objective.

PAX6 intracellular staining

Samples were washed in PBS and dissociated with TrypLE. One million cells per sample were fixed with 4% formaldehyde and then permeabilized with 0.3% Triton, 0.5% BSA in PBS. Cells were washed once in 0.5% BSA. PAX6 primary antibody (Rabbit α PAX6 Biolegend cat. no. 901301, lotB277104) was diluted 1:100 in 0.5% BSA and samples were incubated for 1 h. Following a wash in PBS, goat anti-rabbit Alexa Fluor 488-conjugated secondary antibody (Thermo Fisher cat. no. A11034) (1:500) was applied for 30 min. Samples were then washed and analysed by flow cytometry.

Generation, validation and imaging of AAVS1-CAG-Peredox-mCherry-NLS

CAG-Peredox-mCherry-NLS was inserted into the *AAVS1* safe harbour locus using the approach previously described by Oceguera-Yanez and

colleagues[50]. For plasmid and cloning design, we used the following software: NEBuilder Assembly Tool (https://nebuilderv1.neb.com/), Geneious 9.1.5, In-Fusion cloning tools (https://www.takarabio.com/learning-centers/cloning/in-fusion-cloning-tools), and ApE v2.0.49.10. In brief, we cloned the CAG-Peredox-mCherry-NLS sequence from pcDNA3.1-Peredox-mCherry-NLS (Addgene cat. no. 32384) into the pAAVS1-P-CAG-DEST vector (Addgene cat. no. 80490) by Gibson assembly and co-transfected it along with the pXAT2 vector (Addgene cat. no. 80494) into NCRM1 cells. Two days after transfection, we selected positive clones by supplementing mTeSR1 with puromycin (0.5 μg ml^{-1}, Sigma Aldrich cat. no. P7255) for a total of 10 days. To enhance single-cell survival, we added CloneR (StemCell Technologies cat. no. 05888) to the medium during the first 2 days of selection. We obtained several positive clones and confirmed the homozygous insertion of the sensor by PCR as previously described[50].

To validate that the Peredox NADH/NAD^+ sensor worked as expected in the newly generated AAVS1- CAG-Peredox-mCherry-NLS line, we first performed fluorescence lifetime imaging under different conditions (Extended Data Fig. 4f). We differentiated the sensor line to PSM fate under serum-free conditions on glass coverslips. Cells on coverslips were submerged in a recording chamber filled with a balanced salt solution (140 mM NaCl, 2.5 mM KCl, 10 mM HEPES, 1 mM MgCl2, 2 mM CaCl2, and pH 7.4) at ~34 °C, using a perfusion rate of 5 ml min^{-1}. Cells were sequentially perfused with the following solutions: 2 mM glucose, 0.2 mM, 0 mM glucose, 0 mM glucose with 10 mM lactate, 0 mM glucose with 10 mM pyruvate, and finally 0 mM glucose with a mixture of lactate to pyruvate at a ratio of 30:1. Cells were visualized with a Thorlabs Bergamo II microscope (Thorlabs Imaging Systems), with hybrid photodetectors R11322U-40 (Hamamatsu Photonics). The objective lens used for cell visualization was an Olympus LUMPLFLN 60x/W (NA 1.0). Biosensor fluorescence was excited using light with a wavelength of 790 nm, delivered by a Chameleon Vision-S tunable Ti-Sapphire mode-locked laser (80 MHz,~75 fs; Coherent). Fluorescence emission light was split with an FF562-Di03 dichroic mirror and band-pass filtered for green (FF01-525/50) and red (FF01-641/75) channels (all filter optics from Semrock). Peredox emission was recorded in the green channel. The photodetector signals and laser sync signals were preamplified and then digitized at 1.25 gigasamples per second using a field programmable gate array board (PC720 with FMC125 and FMC122 modules, 4DSP). Microscope control and image acquisition, as well as laboratory-built firmware and software for fluorescence lifetime determination, can be found elsewhere[51].

To further confirm that similar results could be obtained by ratiometric measurements, we imaged AAVS1- CAG-Peredox-mCherry-NLS cells with an LSM880 confocal microscope using a 20×/0.8 objective (Extended Data Fig. 4g) PSM cells were cultured in a balanced salt solution supplemented with 2 mM, 0.2 mM or 0 mM glucose, 10 mM lactate, 10 mM pyruvate or a mixture of lactate to pyruvate at a ratio of 30:1 as described above. Images were thresholded based on mCherry-NLS fluorescence and nuclei were automatically segmented in Fiji[52]. A ratio of the mean Peredox: mCherry fluorescence intensity was calculated for each cell. All cells within an image were averaged to obtain the mean ratio for each sample. This ratiometric imaging approach was used in all experiments.

Mouse and human PSM co-culture

Mouse E14 (no reporter), mouse NLS-BFP; Hes7-Achilles, human NCRM1 (no reporter), and human H2B-mCherry; HES7-Achilles PSCs were differentiated to PSM fate separately as described above. On day 2 of differentiation, PSM cells were dissociated with TrypLE. Mixed cell suspensions consisting of either mouse or human reporter cells combined with either human NCRM1 or mouse E14 cells at a ratio of 1:100 were prepared. This ratio allowed individual cells of the minority species to be completely surrounded by cells of the majority species and prevented the formation of cell clusters corresponding to the minority species. Cells were then reseeded on fibronectin-coated 24-well glass-bottom plates at a density of 2.5×10^6 cells per cm^2 when human cells were in excess or 4×10^6 cells per cm^2 when mouse cells were in excess. These densities allowed the cultures to be fully confluent upon attachment. Cells were then allowed to attach for one hour and subjected to time-lapse imaging. Human H2B-mCherry$^+$ cells were automatically segmented and tracked as previously described[11] to obtain single-cell HES7-Achilles fluorescence intensity profiles. Mouse NLS-BFP$^+$ cells were manually tracked.

Primary mouse PSM explant culture

Explant culture was performed as described by Hubaud and colleagues[15]. LuVeLu[53] CD1 E9.5 mice (both male and female) were sacrificed according to local regulations in agreement with national and international guidelines. We complied with all relevant ethical regulations. Study protocol was approved by Brigham and Women's Hospital IACUC/CCM (Protocol number N000478). Sample size was not estimated, nor were randomization or blinding performed. Tailbud was dissected with a tungsten needle and ectoderm was removed using Accutase. Explants were then cultured on fibronectin-coated plate (LabTek chamber). The medium consisted of DMEM, 4.5 g l^{-1} glucose, 2 mM L-glutamine, 1× non-essential amino acids, 100 U ml^{-1} penicillin, 100 μg ml^{-1} streptomycin, 15% fetal bovine serum (FBS), 3 μM Chir 99021, 200 nM LDN193189, 2.5 μM BMS493, 50 ng ml^{-1} mouse FGF4, 1 μg ml^{-1} heparin, 10 mM HEPES and 10 μM Y-27632. Explants were incubated at 37 °C, 7.5% CO_2.

Time-lapse microscopy

Time-lapse imaging of mouse and human PSM cells and of mouse explants was performed on a Zeiss LSM 780 point-scanning confocal inverted microscope fitted with a large temperature incubation chamber and a CO_2 module. An Argon laser at 514 nm and 7.5% or 2% power was used to excite Achilles or Venus fluorescent proteins, respectively. A DPSS 561 laser at 561 nm and 2% laser power was used to excite mCherry. In all cases, a 20× Plan Apo (N.A. 0.8) objective was used to acquire images with an interval of 18 or 25 min in the case of human samples and 11 or 12 min for mouse samples, for a total of 16–48 h. A 3 × 3 tile of 800 × 800 pixels per tile with a single *z*-slice of 18 μm thickness and 16-bit resolution was acquired per position. Multiple positions, with at least two positions per sample, were imaged simultaneously using a motorized stage. For mouse explants, a single section (~19.6 μm thick) with tiling (3 × 3) of a 512 × 512 pixels field was acquired every 7.5 min at 8-bit resolution.

Oscillation analysis

We used *HES7* knock-in fluorescent reporters to assess segmentation clock oscillations. Although dozens of genes display cyclic gene expression as part of the segmentation clock network[12,54,55], *HES7* was chosen because it is considered the core oscillator for the mammalian segmentation clock. Hairy and enhancer of split (Her/Hes) genes represent the only gene family that is known to oscillate in all vertebrates[55]. Moreover, we and others had previously established pluripotent stem cell-based in vitro clock models based on *HES7* reporters[11–14] Time-lapse movies of HES7-Achilles were first stitched and separated into subsets by position in the Zen program (Zeiss). Then, background subtraction and Gaussian blur filtering were performed in Fiji[52] to enhance image quality. A small region of interest was drawn and the mean fluorescence intensity over time was calculated. For co-culture experiments, we instead tracked individual cells as described in 'Mouse and human PSM co-culture'. Intensity is presented in arbitrary units. For Fig. 1e, intensity profiles were smoothened in GraphPad Prism using six neighbouring data points and a second order polynomial. Profiles were then normalized between zero and one.

For each raw intensity profile, we manually identified peaks and calculated the time interval between each pair of consecutive peaks. All peaks in a given profile were measured. We did not distinguish peaks

based on their order in the oscillation profile. The oscillatory period was defined as the average time between two peaks in HES7-Achilles profiles. This value is shown in figures as the segmentation clock period. Note that HES7-Achilles oscillatory profiles in figures are shown as the mean ± s.e.m. for a set of individual profiles originating from the same experimental batch.

To measure how the oscillation parameters changed over time, we performed Hilbert analysis[56,57] in MATLAB. Oscillation profiles for a given condition were saved as CSV files where the first column represents timepoints (hours) and each subsequent column represents an individual profile. To smoothen the oscillation profiles, we applied the Savitzky-Golay filtering function with a polynomial order of 3 and a frame length of 11. At this point, we manually identified peaks and counted the number of peaks between 0 and 25 h. Peaks were identified by visual inspection based on width and height (that is, no narrower than 8 data points, not shallower than 50 AU). We then subtracted the moving mean with a time window of 10 timepoints. This normalized the data to oscillate about zero. An example of signal processing and peak calling can be found in Supplementary Fig. 1. Next, we applied the Hilbert transformation to the data. The instantaneous amplitude was extracted as the complex magnitude (also called modulus) of the Hilbert transform. Figures showing mean amplitude or relative amplitude simply display the mean over the entire time course. The instantaneous phase was calculated by unwrapping the phase angle of the Hilbert transform. We then obtained the instantaneous frequency by differentiating the phase. We converted frequency to period and plotted this over time. As the Hilbert transformation is overly sensitive to drifts and changes in the shape of oscillations, we excluded non-physiological period values (for example, >30 h, <0) resulting from small blips in the profiles. The MATLAB code for this analysis can be found at GitHub: https://github.com/md2981/Hilbert-Segmentation-Clock

Cell cycle length measurements

To generate cultures with sparsely labelled cells, we mixed HES7-Achilles; AAVS1-CAG-H2B-mCherry human iPS cells or pMsgn1-Venus mouse ES cells with their parental line (NCRM1 or E14, respectively) at a ratio of 1:100 during the initial seeding. Cultures were then differentiated normally and subjected to time-lapse imaging. Individual reporter cells were tracked manually on Fiji[52] and the time of cell division was recorded. The cell cycle length was defined as the time elapsed between the time a cell first divides and the time one of its daughter cells divides again.

To measure cell cycle length in primary mouse PSM explants, lentiviral infection was used to sparsely label cells with a SV40-mCherry reporter[15]. The plasmid EβC (Addgene Plasmid #24312) was cut with BamHI and self-ligated to remove the original insert, thus generating a lentiviral transfer vector that expresses only mCherry. Lentivirus was produced in 293T cells, which were transfected using the $CaCl_2$ method with the packaging plasmids psPAX2 (Addgene cat. no. 12260) and pVSVG (gift from the M. Wernig laboratory). Supernatant was collected, filtered using a 0.45 µM filter and concentrated by centrifugation of 4 volumes of supernatant on 1 volume of TNE buffer (50 mM Tris pH 7.2, 100 mM NaCl, 0.5 mM EDTA, 15% sucrose) at 7,197 rcf for 4 h at 4 °C. Explants were infected for ~4 h and further incubated overnight before imaging. SV40-mCherry$^+$ cells were manually tracked, and the cell cycle length was calculated as described above.

Flow cytometry and cell sorting

To determine the fraction of PSM cells expressing MSGN1-Venus, cultures were dissociated with Accutase and analysed by flow cytometry using an S3 cell sorter (Biorad). Undifferentiated ES cells or iPS cells, which do not express the fluorescent protein, were used as negative control for gating purposes. Samples were analysed in biological triplicates. Results are presented as the percentage of Venus-positive cells among singlets. The same gating strategy was used to sort MSGN1-Venus$^+$ cells for subsequent experiments. The gating strategy is illustrated in Supplementary Fig. 2. All other flow cytometry analyses were performed on a 5-laser Fortessa analyser (BD). Automatic compensation was set up whenever more than one dye or fluorescent protein was used at a time. Flow cytometry data was analysed in FlowJo. The mean fluorescence intensity (MFI) for 10,000 cells is presented. In the case of mouse versus human comparisons, only MSGN1-Venus$^+$ cells were considered in the analysis and MFI was normalized to cell mass.

*Lb*NOX lentiviral overexpression

A plasmid containing the *Lb*NOX sequence was obtained from Addgene (plasmid #75285)[28]. We cloned the *Lb*NOX coding sequence into the BamHI-digested E[beta]C (Addgene plasmid #24312) transfer plasmid. This plasmid was linearized by MluI digestion and *Lb*NOX was inserted by Gibson assembly. The resulting transfer plasmid therefore expressed *Lb*NOX under the control of the EF-1α promoter and mCherry under the control of the SV40 promoter. We produced lentivirus in Lenti-X 293T cells (Takara cat no. 632180) by co-transfecting the transfer plasmid along with psPAX2 (Addgene cat. no. 12260) and pVSVG (gift from the M. Wernig laboratory). Transfection was performed with the jetPEI reagent (Polyplys cat. no. 101000053). Supernatants were collected at 24, 48 and 72 h. Lentiviruses were concentrated using the Lenti-X Concentrator (Takara cat no. 631232), resuspended in DMEM and stored in single-use aliquots at −80 °C. In parallel, we also produced the control BamHI-digested E[beta]C lentivirus, which only expresses mCherry. We did not determine the viral titre.

To transduce human iPS cells, we combined the lentiviruses with dissociated iPS cells immediately prior to seeding. We used a volume of 5 µl lentivirus concentrated supernatant per 100,000 cells. Cultures were incubated overnight and re-infected when PSM differentiation was initiated. This achieved high efficiency of transduction as judged by mCherry expression. Due to issues with silencing, we did not maintain stable lines but rather transduced cells anew for each experiment. We verified that PSM induction was not affected by lentiviral transduction. We confirmed that *Lb*NOX was expressed by immunofluorescence against the C-terminal flag tag.

Mitochondrial content and $\Delta\Psi_m$ measurement

PSM cells were washed in PBS, dissociated in TryplE, washed in DMEM and then incubated for 30 min at 37 °C 5% CO_2 in DMEM supplemented with the appropriate dye. For mitochondrial content measurements, we used 25nM Mitotracker Green (Invitrogen cat. no. M7514). For comparison of $\Delta\Psi_m$ between mouse and human PSM cells, cells were treated with 1 µg ml^{-1} JC-1 (Invitrogen cat. no. T3168). For $\Delta\Psi_m$ measurements in human PSM cells under different conditions, we used 20 nM TMRM (Invitrogen, T668) in combination with 25 nM Mitotracker Green for normalization. The cells were then washed in PBS, spun down, and resuspended in PBS/1% FBS prior to analysis by flow cytometry. As a control, 1 uM FCCP was used to depolarize the inner mitochondrial membrane.

Seahorse assays

PSM cells were dissociated on day 2 of differentiation and reseeded onto fibronectin-coated Seahorse plates (Agilent cat. no. 101085-004) at a density of 7×10^5 cells per cm^2 in Seahorse XF DMEM (Agilent cat. no. 103575-100) supplemented with 10 mM glucose (Agilent cat. no. 103577-100), 1 mM pyruvate (Agilent cat. no. 103578-100) and 2 mM glutamine (Agilent cat. no. 103579-100). For mouse versus human comparisons, MSGN1-Venus$^+$ cells were pre-sorted. Cells were allowed to attach at room temperature for 20 min and then transferred to a 37 °C incubator without CO_2 for 1 h. The Seahorse cartridge was hydrated and calibrated as per the manufacturer instructions. For the Mitochondrial Stress Test (Agilent cat. no. 103015-100), we used oligomycin at 1 µM, FCCP at 1 µM, rotenone at 0.5 µM and antimycin A at 0.5 µM. No-glucose controls were used to calculate the CO_2 contribution factor for glycolytic proton efflux rate determination. To quantify glycolytic versus mitochondrial ATP production, we used the ATP Rate Assay kit (Agilent cat. no. 103592-100).

All samples were run in six to ten replicates in either a Seahorse XF96 or XFe24 Analyzer and the data were analysed in Wave and Microsoft Excel using macros provided by the manufacturer.

For the isolation of mitochondria from mouse and human PSM cells, we followed the protocol described by Bharadwaj and colleagues with some modifications[58]. To obtain sufficient starting material, mouse and human PSM cells from four confluent 10 cm dishes for each species were dissociated using TryplE. Following a PBS wash, the cell pellets were resuspended in 250 µl ice-cold Chappel–Perry buffer I (see[58] for formulation) and transferred to 2 ml glass–glass Douncers. All further steps were performed on ice, including centrifugation at steps at 4 °C. Cells were broken apart with 30 douncer strokes. An additional 250 µl Chappel–Perry buffer I were added, followed by 500 µl Chappel–Perry buffer II. Samples were transferred to 1.5 ml microcentrifuge tubes and centrifuged at 900*g* for 10 min. Supernatants were transferred to new tubes and centrifuged at 10,000*g* for 10 min. Mitochondrial pellets were resuspended in 500 µl Chappel–Perry buffer II, then centrifuged again at 10,000*g* for 10 min and resuspended in 500 µl Chappel–Perry buffer I. Aliquots were taken for BCA protein quantification at this time. Samples were centrifuged one last time at 10,000*g* for 10 min and resuspended in 50 µl mitochondrial assay solution (see ref. [58] for formulation). Mitochondria were diluted to the desired concentration in mitochondrial assay solution supplemented with 10 mM pyruvic acid and 2 mM malic acid. A total amount of 10 µg mitochondria in a volume of 20 µl were seeded per well of an Agilent Seahorse XFe96 plate and attached by centrifugation at 2,000*g* for 20 min. The volume was then completed to 180 µl per well with mitochondrial assay solution containing pyruvic and malic acids, and the samples were loaded into the Seahorse XFe96 analyser. Mix, wait and measurement intervals were followed as per[58]. Injections consisted of final concentrations 2 mM ADP (port A), 5 µM oligomycin (port B), 6 µM FCCP (port C), and 1 µM rotenone with 1 µM antimycin A (port D).

Extracellular glucose, lactate and glutamine quantification

Mouse and human MSGN1-Venus$^+$ cells were pre-sorted and seeded onto a fibronectin-coated 96-well plate at a density of 4×10^5 cells per cm^2. The media consisted of DMEM (Gibco cat. no. A1443001) containing 2 mM glucose, 1 mM glutamine, 1 mM pyruvate, 0.1 mM non-essential amino acids, 1% ITS, 5% dialysed FBS supplemented (Cytiva cat. no. SH30079.01) with 6 µM Chir 99021, 0.5 µM LDN193189, 50 ng ml^{-1} mouse FGF4, 1 µg ml^{-1} heparin, 2.5 µM BMS493 and 10 µM Rocki. Control samples with media only (no cells) were also included. For glucose and lactate detection, 5 µl of media were collected every hour for a total of 6 h, diluted in 195 µl PBS and frozen at −20 °C. The Promega Glucose-Glo (Promega cat. no. J6021) and Lactate-Glo (Promega cat. no. J5021) kits were used according to manufacturer protocols on white 384-well plates. Standard curves of glucose and lactate were used to calculate metabolite concentration in the media. For glutamine detection, media was collected at a single timepoint (12 h) and the Promega Glutamate/Glutamine-Glo kit (Promega cat. no. J8021) was used. Luminescence was measured after the incubation time indicated by the manufacturer using a GloMax Promega plate reader with 1 s integration. Measurements were normalized to cell mass.

Stable isotope tracing

Sample preparation. Mouse and human PSM cells were differentiated as described above in 6 well plates. On day 2 of differentiation, the plates were washed once with PBS and replaced with tracer medium. Tracer medium consisted of 25 mM either unlabelled glucose or [U-$^{13}C_6$] glucose (Cambridge Isotope Laboratories cat. no. CLM-1396-0.5), 4 mM either unlabelled glutamine or [U-$^{13}C_5$]glutamine (Cambridge Isotope Laboratories cat. no. CLM-1822-H-0.1), 1 mM sodium pyruvate, 0.1 mM non-essential amino acids, 100 U ml^{-1} penicillin, 100 µg ml^{-1} streptomycin, 1% ITS, 5% dialysed FBS supplemented with 6 µM Chir 99021, 0.5 µM LDN193189, 50 ng ml^{-1} mouse FGF4, 1 µg ml^{-1} heparin, 2.5 µM BMS493 and 10 µM Rocki. For time-course experiments, samples were collected at the following timepoints: 0 h, 3 h, 6 h, 9 h, 12 h, 18 h, 24 h, 36 h and 48 h. We could not extend the time course further because PSM cells differentiate to somitic fate past this time window[11]. For steady-state measurements, cultures were incubated for 24 h prior to metabolite extraction. Experiments were performed three times independently.

Metabolite extraction. Intracellular metabolites were obtained after washing cells with 2 volumes of room temperature HPLC-grade water and floating the dry plates on liquid nitrogen to quench metabolism. Plates were stored at −80 °C until extraction. Metabolites were extracted with 1 ml 80% methanol pre-cooled to −80 °C. Insoluble material was removed by centrifugation at 21,000*g* for 15 min at 4 °C. The supernatant was evaporated to dryness at 42 °C using a SpeedVac concentrator (Thermo Savant). Samples were resuspended in 35 µl LC–MS-grade water prior to analysis.

Acquisition parameters. LC–MS analysis was performed on a Vanquish ultra-high-performance liquid chromatography system coupled to a Q Exactive orbitrap mass spectrometer by a HESI-II electrospray ionization probe (Thermo). External mass calibration was performed weekly. Metabolite samples (2.5 µl) were separated using a ZIC-pHILIC stationary phase (2.1 × 150 mm, 5 µm) (Merck). The autosampler temperature was 4 °C and the column compartment was maintained at 25 °C. Mobile phase A was 20 mM ammonium carbonate and 0.1% ammonium hydroxide. Mobile phase B was acetonitrile. The flow rate was 0.1 ml min^{-1}. Solvent was introduced to the mass spectrometer via electrospray ionization with the following source parameters: sheath gas 40, auxiliary gas 15, sweep gas 1, spray voltage +3.0 kV for positive mode and −3.1 kV for negative mode, capillary temperature 275 °C, S-lens RF level 40, and probe temperature 350 °C. Data were acquired and peaks integrated using TraceFinder 4.1 (Thermo).

Stable isotope quantification. All metabolites were measured using the following mobile phase gradient: 0 min, 80% B; 5 min, 80% B; 30 min, 20% B; 31 min, 80% B; 42 min, 80% B. The mass spectrometer was operated in selected ion monitoring mode with an m/z window width of 9.0 centred 1.003355-times half the number of carbon atoms in the target metabolite. The resolution was set at 70,000 and AGC target was 1×10^5 ions. Peak areas were corrected for quadrupole bias as previously described[59]. Raw mass isotopomer distributions were corrected for natural isotope abundance using a custom R package (mzrtools, https://github.com/wmoldham/mzrtools) employing the method of ref. [60].

Cell volume measurements

Cells were dissociated in TrypLE, washed and resuspended in PBS. Volume was measured on a Moxi Go II Coulter-principle cell sizer and flow cytometer. When mouse versus human PSM cells were compared, only MSGN1-Venus$^+$ cells were considered. Data was analysed in FlowJo.

SMR mass and density measurements

Mouse and human PSM cells were dissociated in TrypLE and MSGN1-Venus$^+$ cells were sorted. Cells were then counted and resuspended in DMEM/F12, 1% ITS, 5% FBS with 6 µM Chir 99021, 20 ng ml^{-1} bFGF and 0.5 µM LDN193189 at a concentration of 3×10^5 cells per ml. The cells were kept on ice and their total mass and density were measured using a SMR according to a previously developed fluid-switching method[20]. The SMR is a vibrating cantilever with a fluidic channel inside. In the absence of cells, the vibration frequency of the cantilever is proportional to the density of the fluid flowing through the cantilever. As a cell flows through the cantilever, the vibration frequency of the cantilever changes proportionally to the buoyant mass of the cell. Following the measurements of normal media density and the cell's buoyant mass with this media, the cell is immersed in culture media that has been made denser by the addition of 35% OptiPrep (Sigma Aldrich cat.

no. D1556-250ML). The cell then flows back through the cantilever in the high-density media to obtain a second set of buoyant mass and media density measurements. The total mass and density of the cell is calculated by comparing these two sets of measurements according to the equation $BM = V(\rho_{cell} - \rho_{fluid})$, where BM is buoyant mass, V is volume, ρ_{cell} is density of the cell, and ρ_{fluid} is the density of the medium. After each cell is measured, the cell is flushed out of the SMR before fresh media and the next cell is loaded into the SMR. For measurements of cells' dry mass, dry volume and the density of the dry mass, a similar fluid-switching protocol was followed but, instead of using OptiPrep containing media, the second measurement was carried out in media where 50% of the water content was heavy water (D_2O). Cellular water content exchanges rapidly[19,20] causing the intracellular water content to be identical and neutrally buoyant to the extracellular water content. Therefore, the measurements in normal and heavy water can be used to calculate the dry mass, dry volume and the density of the dry mass according to the equation $BM = M_{dry}(1 - (\rho_{fluid}/\rho_{drymass}))$, where BM is buoyant mass, M_{dry} is dry mass of the cell, $\rho_{drymass}$ is density of the dry mass, and ρ_{fluid} is the density of the extracellular fluid[19,20]. All measurements were carried out at +4 °C. Calibration of the SMR frequency response to a cell was done using NIST traceable 10.12 µm diameter polystyrene beads (Thermo Scientific, Duke Standard beads, cat. no. 4210A), and the calibration of SMR baseline frequency to fluid density was done using NaCl solutions of known density[61].

Small molecule inhibitor treatments

Human PSM cells were differentiated using the serum-free protocol[11] and treated chronically with the relevant inhibitors or supplements as indicated on Supplementary Table 1[28,29,33,62–74] starting on day 2 of differentiation. Time-lapse imaging started approximately 2 h after the inhibitor addition. In the case of aphidicolin, cells were pre-treated for 24 h before imaging. All other assays (Seahorse, proteasome activity, NAD^+/NADH, Peredox fluorescence, and so on) were performed after 16–24 h of treatment to observe chronic effects.

Whole-cell NAD^+/NADH ratio

Cells were dissociated with TrypLE, washed and resuspended in PBS at a density of 8×10^5 cells per ml. For each sample, 50 µl were distributed in triplicate wells of a 96-well plate. In the case of mouse versus human comparisons, MSGN1-Venus$^+$ cells were pre-sorted. Samples were lysed by adding 50 µl 0.2 N NaOH with 1% dodecyltrimethylammonium bromide to preserve the stability of dinucleotides and incubated for 10 min at room temperature with gentle shaking. Half of each sample was then transferred to an empty well within the same plate and 25 µl 0.4 N HCl were added. Samples were then incubated for 15 min at 65 °C to selectively denature NAD^+ in the basic solution and NADH in the acidic solution. Samples were then cooled down to room temperature for 5 min. pH was restored to neutral conditions by adding 25 µl 0.5 M Trizma base to acid-treated samples and 50 µl Trizma/HCl solution (1:1 mixture of 0.5 M Trizma base and 0.4 N HCl) to base-treated samples. 40 µl of each sample were then transferred to a white 96-well plate. The detection reagent mixture was prepared according to the instructions in the Promega NAD/NADH (cat. no. G9071) kit and 40 µl were added per sample. Luminescence was measured after an incubation of 45 min at room temperature using a GloMax Promega plate reader with 1 s integration. The NAD^+/NADH ratio was calculated as the luminescence ratio of the acid-treated sample to the base-treated sample.

Extracellular lactate/pyruvate measurements

On day 2 of differentiation, the media was refreshed, and cells were incubated for 10 h. Spent medium was collected and centrifuged at 300*g* for 5 min to pellet cell debris. The supernatant was transferred to a new tube and flash frozen in liquid nitrogen. Samples were kept at −80 °C until extraction. Media lactate and pyruvate quantitation was performed by using a LC–MS method with stable isotope dilution. Fifteen microlitres of spent medium was extracted with 117 µl acetonitrile and 45 µl labelled lactate (D_3-lactate, CDN Isotopes) and pyruvate ($13C_3$-pyruvate, Sigma) diluted in water. The samples were then vortexed and left on ice for 5 min, vortexed again, and then spun at 21,100*g* for 10 min. One-hundred microlitres of the supernatant was loaded into a glass vial for LC–MS analysis. Ten microlitres of each sample was analysed using a Q Exactive Plus Orbitrap Mass Spectrometer with a DionexUltiMate 3000 UHPLC system (Thermo Fisher Scientific). Metabolites were separated on an Xbridge amide HILIC column (2.1X100 mm, 2.5 µM particle size, Waters). Mobile phase A was 20 mM ammonium acetate, 0.25% ammonium hydroxide, 5% acetonitrile, pH 9.0. Mobile phase B was 100% acetonitrile. The gradient was: 85%B for 0–0.5 min, decreased to 35% B from 0.5–9 min, decreased to 2% B from 9–11 min, held at 2% B from 11–12 min, increased to 85% B from 12–13.5 min, held at 85% B from 13.5–18 min. The flow rate was 220 µl min^{-1} from 0–14.6 min and 420 µl min^{-1} from 15–18 min. The MS data acquisition was polarity-switching full scan mode in a range of 70–1,000 *m/z*, with resolution 70,000, AGC target of 3×10^6, and maximum injection time of 80 ms. All LC–MS data were collected with samples injected in a randomized order. Absolute quantitation was determined with a standard curve of known concentrations of unlabelled lactate and pyruvate extracted with the same labelled internal standards.

ADP/ATP ratio and ATP content measurements

The BioVision ApoSENSOR ADP/ATP Ratio Bioluminescent Assay Kit (cat. no. K255-200) was used according to manufacturer's instructions. Cells were dissociated with TrypLE, washed and resuspended in nucleotide releasing buffer at a density of 3×10^5 cells per ml. In the case of mouse versus human comparisons, MSGN1-Venus$^+$ cells were pre-sorted. Background luminescence was measured first, followed by ATP-linked luminescence. To measure ADP, samples were treated with ADP-converting enzyme to generate ATP from ADP. Total (ATP + ADP) luminescence was then recorded. ADP-linked luminescence was calculated by subtracting the ATP-linked luminescence from the total luminescence. A GloMax Promega plate reader with 1 s integration was used.

Puromycin incorporation and pulse-chase experiments

To pulse cells with puromycin, samples were washed in PBS and incubated for 1 h at 37 °C 5% CO_2 in DMEM containing 1 µg ml^{-1} puromycin or 20 µM *O*-propargyl-puromycin (OPP-Puro). Samples were collected immediately following the incubation period for translation rate measurements. For degradation rate measurements, samples were washed with DMEM and chased for the indicated period of time. Specifically, samples were collected every 3 h for a total of 12 h. After collection, samples were washed again in PBS and dissociated with TrypLE. One million cells per sample were fixed with 4% formaldehyde and then permeabilized with 0.3% Triton in PBS. Puromycin-treated samples were then incubated for 1 h with anti-puromycin Alexa Fluor 647-directly conjugated antibody (1:100; Millipore Sigma cat. no. MABE343). OPP-Puro samples were processed for Click chemistry detection with Alexa Fluor 647 picolyl azide as per the instructions in the Click-iT Plus OPP Protein Synthesis Assay Kit (Invitrogen cat. no. C10458). Samples were then analysed by flow cytometry. In the case of mouse versus human comparisons, only MSGN1-Venus$^+$ cells were considered.

L-Azidohomoalanine pulse-chase experiments

The Click-it L-azidohomoalanine (AHA) Alexa Fluor 488 Protein Synthesis HCS Assay (Invitrogen cat. no. C10289) was used. Cells were washed in PBS and pre-incubated in DMEM lacking methionine (Gibco cat. no. 21013024 supplemented with 2 mM glutamine, 1 mM sodium pyruvate, 1% non-essential amino acids and 0.2 mM cysteine) for 1 h prior to the AHA pulse. The medium was then replaced by methionine-free DMEM containing 50 µM AHA and cells were incubated for one hour. Samples were either processed immediately or after the indicated chase time as per the manufacturer instructions. Samples were then analysed by flow cytometry.

Proteasome activity assays

The Promega Proteasome-Glo Chemotrypsin-like assay (Promega cat. no. G8660) was used following the manufacturer's protocols. Cells were dissociated with TrypLE, washed several times and resuspended in DMEM at a density of 8×10^5 cells per ml. In the case of mouse versus human comparisons, MSGN1-Venus$^+$ cells were pre-sorted. Luminescence was recorded on a GloMax Promega plate reader with 1 s integration.

Cell viability assay

To document that inhibitor doses are sub-lethal, we assessed cell viability with trypan blue following 24 h of incubation with the relevant inhibitor.

Statistical analyses

Statistical analyses were performed with Prism 9 software (GraphPad). *P* values < 0.05 were considered significant. Details of statistical analyses are indicated in figure legends. Unpaired *t*-tests or ordinary one-way ANOVA were performed with Tukey correction for multiple comparisons. All differentiation experiments were performed a minimum of three independent times (rounds of differentiation), each containing at least three technical replicates (wells) per condition.

Reporting summary

Further information on research design is available in the Nature Portfolio Reporting Summary linked to this article.

Data availability

All data are available within the article, supplementary files and source data files. All materials used in this study, including stem cell lines carrying knock-in reporters, are available by request from the corresponding author. Source data are provided with this paper.

Code availability

The MATLAB code for Hilbert analysis of oscillation properties can be found at GitHub: https://github.com/md2981/Hilbert-Segmentation-Clock. The R custom package, mzrtools, for correction of natural isotope abundance in raw mass isotopomer distributions can also be found at GitHub: https://github.com/wmoldham/mzrtools.

46. Chal, J. et al. Differentiation of pluripotent stem cells to muscle fiber to model Duchenne muscular dystrophy. *Nat. Biotechnol.* **33**, 962–969 (2015).
47. Chal, J. et al. Recapitulating early development of mouse musculoskeletal precursors of the paraxial mesoderm in vitro. *Development* **145**, dev157339 (2018).
48. Chal, J. et al. Generation of human muscle fibers and satellite-like cells from human pluripotent stem cells in vitro. *Nat. Protoc.* **11**, 1833–1850 (2016).
49. Tomishima, M. in *StemBook* (Harvard Stem Cell Institute, 2008).
50. Oceguera-Yanez, F. et al. Engineering the AAVS1 locus for consistent and scalable transgene expression in human iPSCs and their differentiated derivatives. *Methods* **101**, 43–55 (2016).
51. Yellen, G. & Mongeon, R. Quantitative two-photon imaging of fluorescent biosensors. *Curr. Opin. Chem. Biol.* **27**, 24–30 (2015).
52. Schindelin, J. et al. Fiji: an open-source platform for biological-image analysis. *Nat. Methods* **9**, 676–682 (2012).
53. Aulehla, A. et al. A β-catenin gradient links the clock and wavefront systems in mouse embryo segmentation. *Nat. Cell Biol.* **10**, 186–193 (2008).
54. Dequéant, M. L. et al. A complex oscillating network of signaling genes underlies the mouse segmentation clock. *Science* **314**, 1595–1598 (2006).
55. Krol, A. J. et al. Evolutionary plasticity of segmentation clock networks. *Development* **138**, 2783–2792 (2011).
56. Oppenheim, A. V., Schafer, R. W. & Buck., J. R. *Discrete-Time Signal Processing*. 2nd edn (Prentice Hall, 1999).
57. Rosenblum, M. & Kurths, J. *Synchronization: A Universal Concept in Nonlinear Science* (Cambridge Univ. Press, 2003).
58. Bharadwaj, M. S. Preparation and respirometric assessment of mitochondria isolated from skeletal muscle tissue obtained by percutaneous needle biopsy. *J. Vis. Exp.* **96**, 52350 (2015).
59. Kim, D. et al. SHMT2 drives glioma cell survival in ischaemia but imposes a dependence on glycine clearance. *Nature* **520**, 363–367 (2015).
60. Fernandez, C. A. et al. Correction of 13C mass isotopomer distributions for natural stable isotope abundance. *J. Mass Spectrom.* **31**, 255–262 (1996).
61. Mu, L. et al. Mass measurements during lymphocytic leukemia cell polyploidization decouple cell cycle- and cell size-dependent growth. *Proc Natl Acad Sci USA* **117**, 15659–15665 (2020).
62. Sheaff, R., Ilsley, D. & Kuchta, R. Mechanism of DNA polymerase α inhibition by aphidicolin. *Biochemistry* **30**, 8590–8597 (1991).
63. Palmer, G. et al. Studies on the respiratory chain-linked reduced nicotinamide adenine dinucleotide dehydrogenase. XIV. Location of the sites of inhibition of rotenone, barbiturates, and piericidin by means of electron paramagnetic resonance spectroscopy. *J. Biol. Chem.* **243**, 844–847 (1968).
64. Miyadera, H. et al. Atpenins potent and specific inhibitors of mitochondrial complex II (succinate-ubiquinone oxidoreductase). *Proc. Natl Acad. Sci. USA* **100**, 473–477 (2003).
65. Slater, E. C. The mechanism of action of the respiratory inhibitor antimycin. *Biochim. Biophys. Acta Rev. Bioenerg.* **301**, 129–154 (1973).
66. Keilin, D. The action of sodium azide on cellular respiration and on some catalytic oxidation reactions. *Proc. R. Soc. B. Biol. Sci.* **121**, 165–173 (1936).
67. Kankotia, S. & Stacpoole, P. W. Dichloroacetate and cancer: new home for an orphan drug? *Biochem. Biophys. Acta Rev. Cancer* **1846**, 617–629 (2014).
68. Benz, R. & McLaughlin, S. The molecular mechanism of action of the proton ionophore FCCP (carbonylcyanide *p*-trifluoromethoxyphenylhydrazone). *Biophys. J.* **41**, 381–398 (1983).
69. Racker, E. A mitochondrial factor conferring oligomycin sensitivity on soluble mitochondrial ATPase. *Biochem. Biophys. Res. Commun.* **10**, 435–439 (1963).
70. Baliga, B. S., Pronczuk, A. W. & Munro, H. N Mechanism of cycloheximide inhibition of protein synthesis in a cell-free system prepared from rat liver. *J. Biol. Chem.* **244**, 4480–4489 (1969).
71. Fu, Z., Lu, C., Zhang, C. & Qiao, B. PSMA5 promotes the tumorigenic process of prostate cancer and is related to bortezomib resistance. *Anti-Cancer Drugs* **30**, 722–730 (2019).
72. Dick, L. R. et al. Mechanistic studies on the inactivation of the proteasome by lactacystin in cultured cells. *J. Biol. Chem.* **272**, 182–188 (1997).
73. Zhou, M. et al. Warburg effect in chemosensitivity: targeting lactate dehydrogenase-A re-sensitizes taxol-resistant cancer cells to taxol. *Mol. Cancer* **9**, 33 (2010).
74. Aguer, C. et al. Galactose enhances oxidative metabolism and reveals mitochondrial dysfunction in human primary muscle cells. *PLoS ONE* **6**, e28536 (2011).

Acknowledgements We thank members of the Pourquié laboratory and J. Locasale, G. Ruvkun, C. Tabin, N. Perrimon, S. Rath and V. Mootha for critical reading of the manuscript and discussions; the NeuroTechnology Studio at Brigham and Women's Hospital for providing access to the Agilent Seahorse XF96 Extracellular Flux Analyzer and Zeiss LSM880 confocal microscope, and for consultation on data acquisition and data analysis; the Center for Neurologic Diseases (ARCND) Flow Cytometry Core Facility at Brigham and Women's Hospital for access to the BD Fortessa flow cytometer; the Seahorse core facility at Brigham and Women's hospital for training and access to the Agilent Seahorse XFe24 Extracellular Flux Analyzer; S. Oh and the Kirschner laboratory at Harvard Medical School for providing access to the Moxi Go II for cell volume measurements; O. Goldberger and V. Mootha for providing the *Lb*NOX plasmids; and M. Bharadwaj for guidance in the implementation of Seahorse measurements on isolated mitochondria. The Pourquié laboratory and M.D.-C. were funded by grants from the Eunice Kennedy Shriver National Institute of Child Health and Human Development (NICHD) of the National Institutes of Health (NIH) under award numbers 2R01HD085121-06A and F31HD100033, respectively. M.D.-C. is a recipient of the NASEM Ford Foundation Dissertation fellowship. This work was supported by the Cancer Systems Biology Consortium funding (U54-CA217377) from the National Cancer Institute (S.R.M.) and the Virginia and D. K. Ludwig Fund for Cancer Research (S.R.M.). O.S.S. was supported by the F32GM133047 from the NIH. The content is solely the responsibility of the authors and does not necessarily represent the official views of the National Institutes of Health.

Author contributions M.D.-C. and O.P. conceptualized the study. M.D.-C. performed the experiments and analysed the data. T.P.M. and S.R.M. carried out SMR experiments and analysed the resulting data. O.S.S. performed the lactate and pyruvate measurements in spent media. D.S. generated the AAVS1-CAG-Peredox-mCherry-NLS human PSC line. C.M.D.-G. and G.Y. contributed to the functional validation of the AAVS1-CAG-Peredox-mCherry-NLS human PSC line. S.G. helped maintain mouse and human PSC cultures and seeded cells for differentiation. A.H. performed experiments involving primary mouse PSM tissue. W.M.O. performed LC–MS/MS for stable isotope metabolic tracing, helped with Seahorse experiments, and provided guidance on the project. M.D.-C. and O.P. wrote the manuscript. O.P. supervised the project. All authors discussed the results and commented on the manuscript.

Competing interests O.P. is scientific founder of Anagenesis Biotechnologies. S.R.M. is a co-founder of Travera and Affinity Biosensors, which develop technologies relevant to the research presented in this work. All other authors declare no competing interests.

Additional information

Supplementary information The online version contains supplementary material available at https://doi.org/10.1038/s41586-022-05574-4.

Correspondence and requests for materials should be addressed to Margarete Diaz-Cuadros or Olivier Pourquié.

Peer review information *Nature* thanks Joseph Baur, Katharina Sonnen and the other, anonymous, reviewer(s) for their contribution to the peer review of this work. Peer review reports are available.

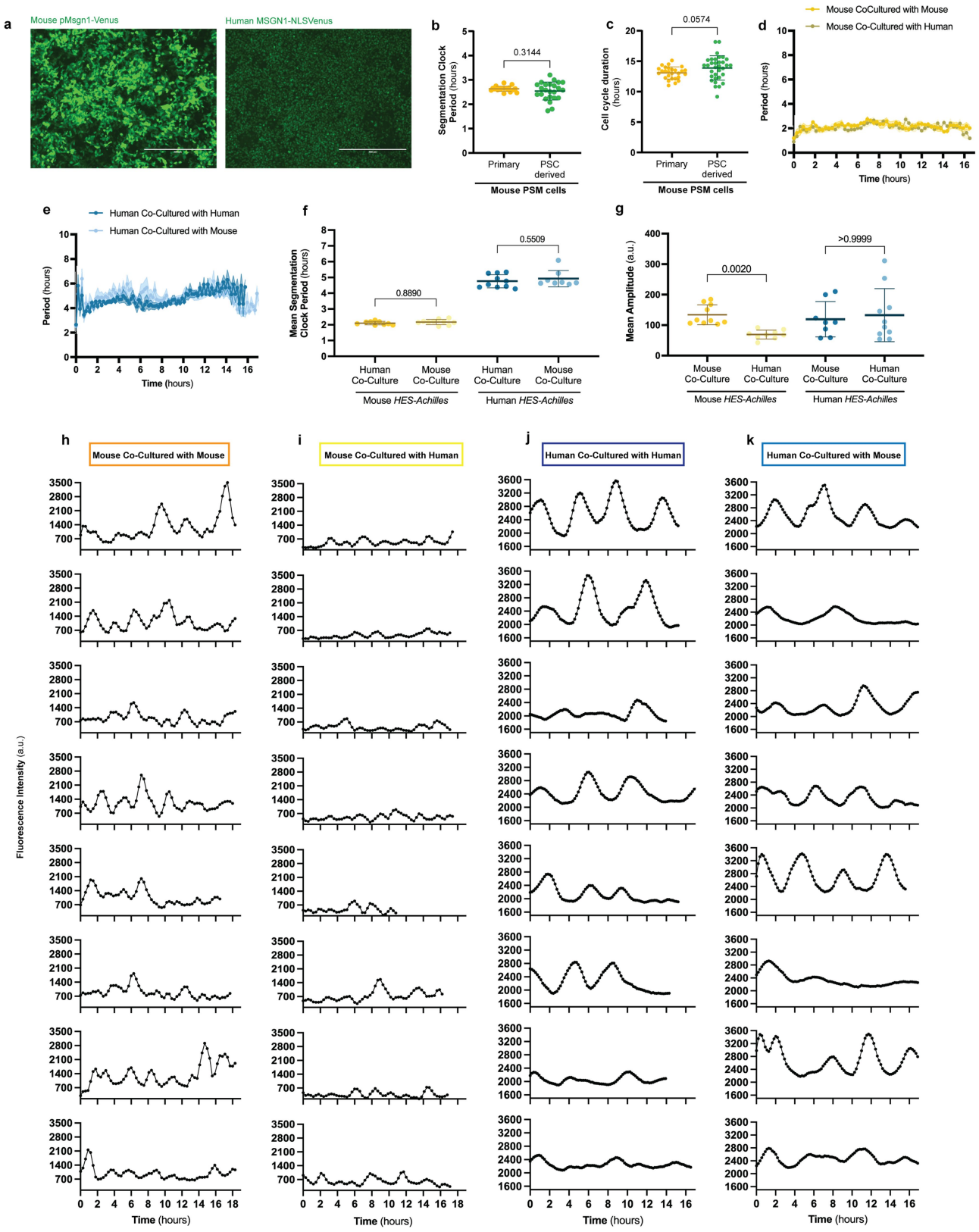

Extended Data Fig. 1 | See next page for caption.

Extended Data Fig. 1 | The segmentation clock-period is cell-autonomous even in chimeric conditions. a. Representative micrographs of MSGN1-Venus fluorescence in mouse (left) and human (right) PSC-derived PSM cells on day 2 of differentiation. Note the reporter is cytoplasmic in mouse cells but nuclear in human cells. Similar results were obtained n = 15 times. Scale bar = 400 μm. b. Period of segmentation clock oscillations in primary PSM tissue dissected from E9.5 mouse embryos carrying the *LuVeLu* reporter (n = 18) and PSC-derived PSM expressing the *Hes7-Achilles* reporter (n = 24). Mean ±SD. Unpaired two-sided t-test. c. Cell cycle duration in primary PSM tissue dissected from E9.5 mouse embryos (n = 27) and PSC-derived PSM (n = 33). Mean ±SD. Unpaired two-sided t-test. d. Instantaneous HES7-Achilles oscillatory period over the course of 16 h as calculated by Hilbert transformation for mouse PSM cells co-cultured with mouse (n = 10) or human (n = 7) non-reporter PSM cells. Mean ±SEM. e. Instantaneous HES7-Achilles oscillatory period over the course of 16 h as calculated by Hilbert transformation for human PSM cells co-cultured with human (n = 11) or mouse (n = 8) non-reporter PSM cells. Mean ±SEM. f. Mean segmentation clock period as calculated by Hilbert transformation for mouse (left) or human (right) PSM cells co-cultured with either mouse or human non-reporter PSM cells. Mean ±SD. n = 10 (mouse-mouse), n = 9 (mouse-human), n = 8 (human-mouse), n = 10 (human-human). One-way ANOVA with Šidák correction. g. Mean amplitude of HES7-Achilles oscillations in mouse (left) or human (right) PSM cells co-cultured with either mouse or human non-reporter PSM cells. Mean ±SD. n = 10 (mouse-mouse), n = 9 (mouse-human), n = 8 (human-mouse), n = 10 (human-human). Kruskal-Wallis test with Dunn's correction. h. Representative single-cell tracks of HES7-Achilles fluorescence for mouse PSM cells cultured with non-reporter mouse PSM cells. i. Representative single-cell tracks of HES7-Achilles fluorescence for mouse PSM cells cultured with non-reporter human PSM cells. j. Representative single-cell tracks of HES7-Achilles fluorescence for human PSM cells cultured with non-reporter human PSM cells. k. Representative single-cell tracks of HES7-Achilles fluorescence for human PSM cells cultured with non-reporter mouse PSM cells.

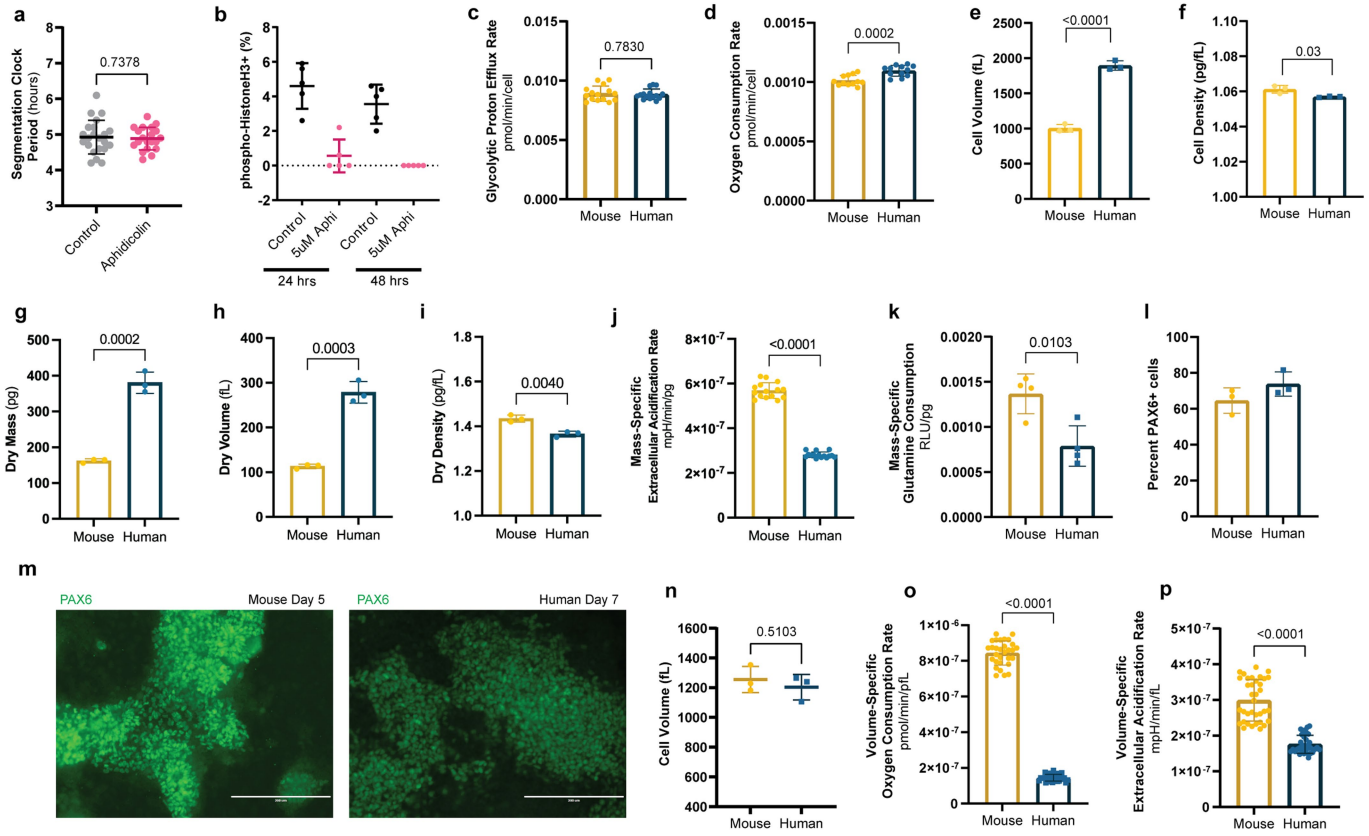

Extended Data Fig. 2 | Comparison of metabolic and physical parameters in mouse vs. human PSM and neural progenitor cells. a. HES7-Achilles oscillatory period in human PSM cells under control (DMSO; n = 22) or 5 µM aphidicolin (n = 20) conditions. Cultures were pre-treated with DMSO or aphidicolin for 24 h to induce cell cycle arrest. Mean ±SD. Unpaired two-sided t-test. b. Quantification of immunofluorescence staining for histone H3 phosphorylated at Ser10 in human PSM cells treated with vehicle control (DMSO) or 5 µM aphidicolin for 24 or 48 h. Mean ±SD. n = 5 biological replicates. c. Glycolytic proton efflux rate per cell for MSGN1-Venus+ PSC-derived mouse and human PSM cells. Same data as Fig. 2d but normalized by cell. Mean ±SD. n = 15. Unpaired two-sided t-test. d. Oxygen consumption rate per cell for MSGN1-Venus+ PSC-derived mouse and human PSM cells. Same data as Fig. 2d but normalized by cell. Mean ±SD. n = 12. Unpaired two-sided t-test. e. Total cell volume as measured in a suspended microchannel resonator for MSGN1-Venus+ PSC-derived mouse and human PSM cells. Each datapoint represents the mean of >200 individual cells. Mean ±SD. n = 3 independent experiments. Unpaired two-sided t-test: $p = 5.9 \times 10^{-5}$. f. Total cell density of MSGN1-Venus+ PSC-derived mouse and human PSM cells as measured on a suspended microchannel resonator. Each datapoint represents the mean of >200 individual cells. Mean ±SD. n = 3 independent experiments. Unpaired two-sided t-test. g. Dry mass as measured in a suspended microchannel resonator for MSGN1-Venus+ PSC-derived mouse and human PSM cells. Each datapoint represents the mean of >200 individual cells. Mean ±SD. n = 3 independent experiments. Unpaired two-sided t-test. h. Dry volume as measured in a suspended microchannel resonator for MSGN1-Venus+ PSC-derived mouse and human PSM cells. Each datapoint represents the mean of >200 individual cells. Mean ±SD. n = 3 independent experiments. Unpaired two-sided t-test. i. Dry density as measured in a suspended microchannel resonator for MSGN1-Venus+ PSC-derived mouse and human PSM cells. Each datapoint represents the mean of >200 individual cells. Mean ±SD. n = 3 independent experiments. Unpaired two-sided t-test. j. Mass-specific extracellular acidification rate (ECAR) in MSGN1-Venus+ PSC-derived mouse and human PSM cells. Mean ±SD. n = 15. Unpaired two-sided t-test: $p = 8.7 \times 10^{-23}$. k. Relative mass-specific glutamine consumption after 12 h of culture for MSGN1-Venus+ PSC-derived mouse and human PSM cells. Mean ±SD. n = 4 biological replicates. Unpaired two-sided t-test. l. Percent PAX6+ cells in mouse (day 5) and human (day 7) neural progenitor cultures as measured by intracellular staining and flow cytometry. Mean ±SD. n = 3 independent experiments. m. Representative micrographs of immunofluorescence staining for PAX6 in PSC-derived mouse (left) and human (right) neural progenitor cells on days 5 and 7 of differentiation, respectively. Similar results were obtained n = 3 times. Scale bar = 200 µm. n. Volume of mouse (day 5) and human (day 7) neural progenitor cells as measured by a coulter counter. Mean ±SD. n = 3 independent experiments. Unpaired two-sided t-test. o. Volume-specific oxygen consumption rate for PSC-derived mouse and human neural progenitor cells. Mean ±SD. n = 30. Unpaired two-sided t-test: $p = 1.69 \times 10^{-51}$. p. Volume-specific extracellular acidification rate for PSC-derived mouse and human neural progenitor cells. Mean ±SD. n = 36. Unpaired two-sided t-test: $p = 3.75 \times 10^{-18}$.

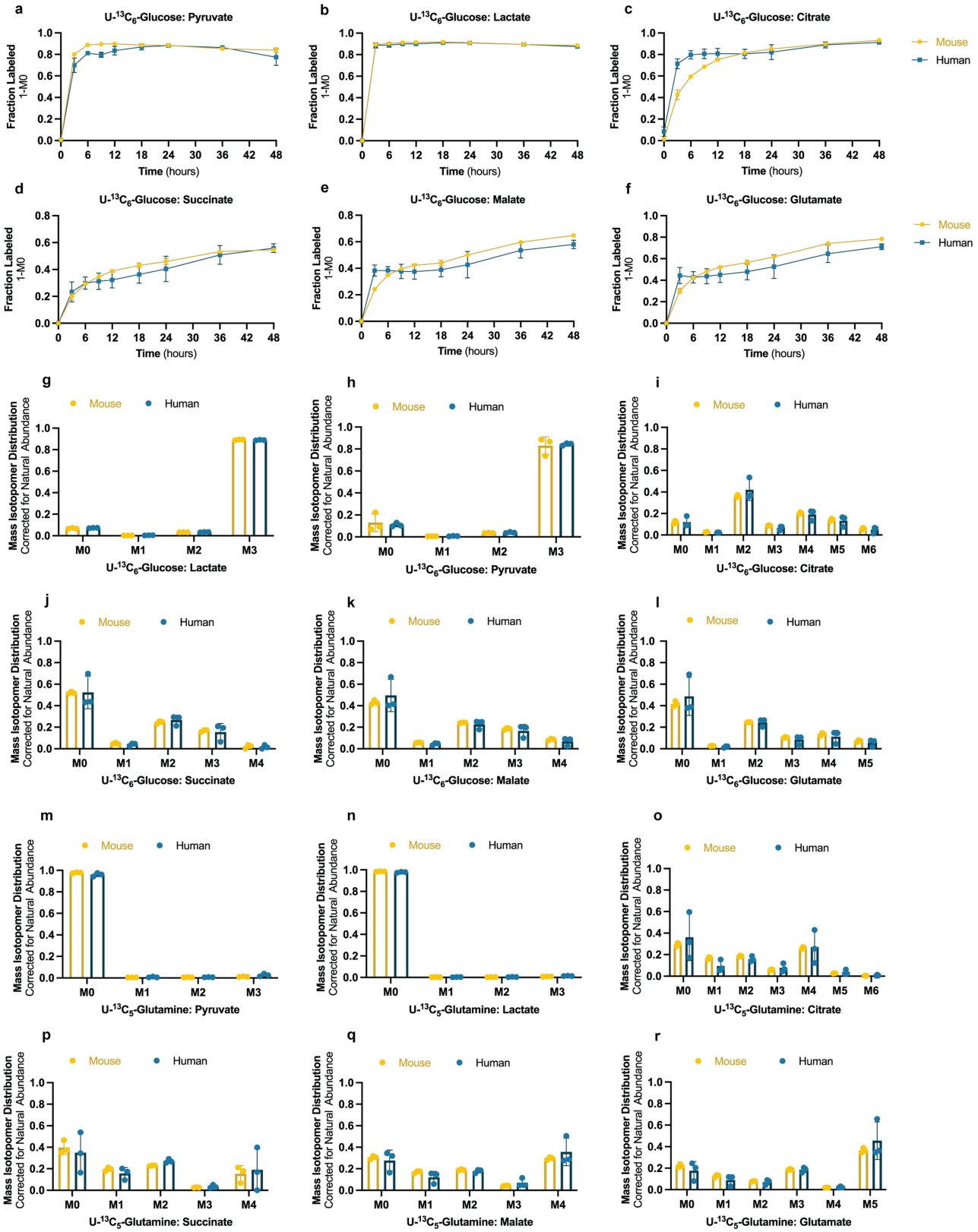

Extended Data Fig. 3 | Stable isotope tracing of glucose and glutamine utilization patterns in mouse and human PSM cells. a-f. Stable isotope labeling with 25 mM $U^{13}C_6$-Glucose over the course of 48 h for PSC-derived mouse and human PSM cells. Total fraction labeled by any isotopomer is expressed as 1-M0 for pyruvate (a), lactate (b), citrate (c), succinate (d), malate (e), and glutamate (f). Mean ±SD. n = 3 independent experiments. g-l. Mass isotopomer distribution, adjusted for natural abundance, for pyruvate (e), lactate (f), citrate (g), succinate (h), malate (i), and glutamate (j) after 24 h of labeling with 25 mM $U^{13}C_6$-Glucose in mouse and human PSM cells. Labels in the x-axis correspond to distinct mass isotopomers with increasing number of heavy carbons. Mean ±SD. n = 3 independent experiments. m-r. Mass isotopomer distribution, adjusted for natural abundance, for pyruvate (k), lactate (l), citrate (m), succinate (n), malate (o), and glutamate (p) after 24 h of labeling with 4 mM $U^{13}C_5$-Glutamine in mouse and human PSM cells. Labels in the x-axis correspond to distinct mass isotopomers with increasing number of heavy carbons. Mean ±SD. n = 3 independent experiments.

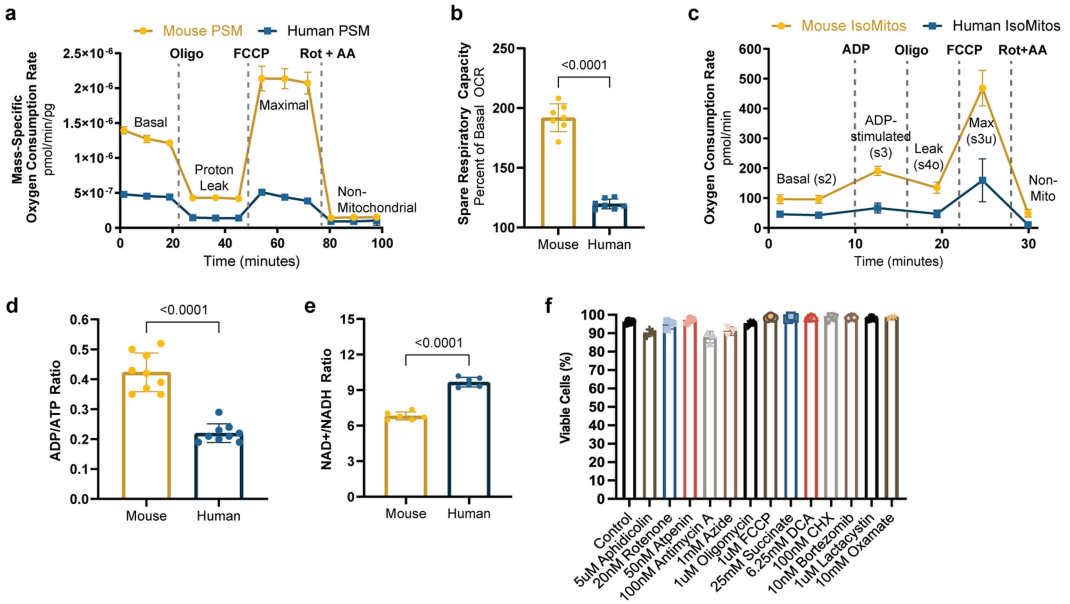

Extended Data Fig. 4 | Mitochondrial properties of mouse and human PSM cells. a. Mass-specific oxygen consumption rate measured over the course of the mitochondrial stress test for MSGN1-Venus+ PSC-derived mouse (n = 9) and human (n = 7) PSM cells. 1 µM oligomycin, 1 µM FCCP, and 0.5 µM Rotenone + 0.5 µM Antimycin A were added at the timepoints marked by dotted lines. The first three timepoints denote basal respiration;, respiration after oligomycin addition corresponds to proton leak; FCCP induces maximal respiration; and rotenone/antimycin reveal non-mitochondrial respiration. Spare capacity refers to the difference between maximal and basal respiration rates. Mean ±SD. b. Spare respiratory capacity in MSGN1-Venus+ PSC-derived mouse and human PSM cells. Mean ±SD. n = 7 biological replicates. Unpaired two-sided t-test: $p = 2.7 \times 10^{-9}$. c. Oxygen consumption rate profiles for mitochondria isolated from mouse and human PSC-derived PSM cells. Rates correspond to 10 ug mitochondria seeded per assay well. ETC complex I substrates pyruvate and malate were provided to fuel respiration. 2 mM ADP, 5 µM Oligomycin, 6 µM FCCP, and 1 µM Rotenone with 1 µM Antimycin A were injected at the timepoints marked by dotted lines. First two timepoints correspond to basal respiration (state 2), followed by ADP-stimulated respiration (state 3), then leak respiration (state 4o), followed by maximal FCCP-stimulated respiration (state 3u), and finally non-mitochondrial respiration. Mean ±SD. n = 5 biological replicates. d. Whole-cell NAD^+/NADH ratio in MSGN1-Venus+ PSC-derived mouse and human PSM cells. Each datapoint represents the average of 3 technical replicates. Mean ±SD. n = 6 biological replicates. Unpaired two-sided t-test: $p = 1.2 \times 10^{-7}$. e. Whole-cell ADP/ATP ratio in MSGN1-Venus+ PSC-derived mouse and human PSM cells. Mean ±SD. n = 9. Each datapoint represents the average of 3 technical replicates. Unpaired two-sided t-test: $p = 2.42 \times 10^{-7}$. f. Percent viable cells as measured by trypan blue staining in human PSM cells treated with the indicated inhibitors for 24 h. n = 3 independent experiments.

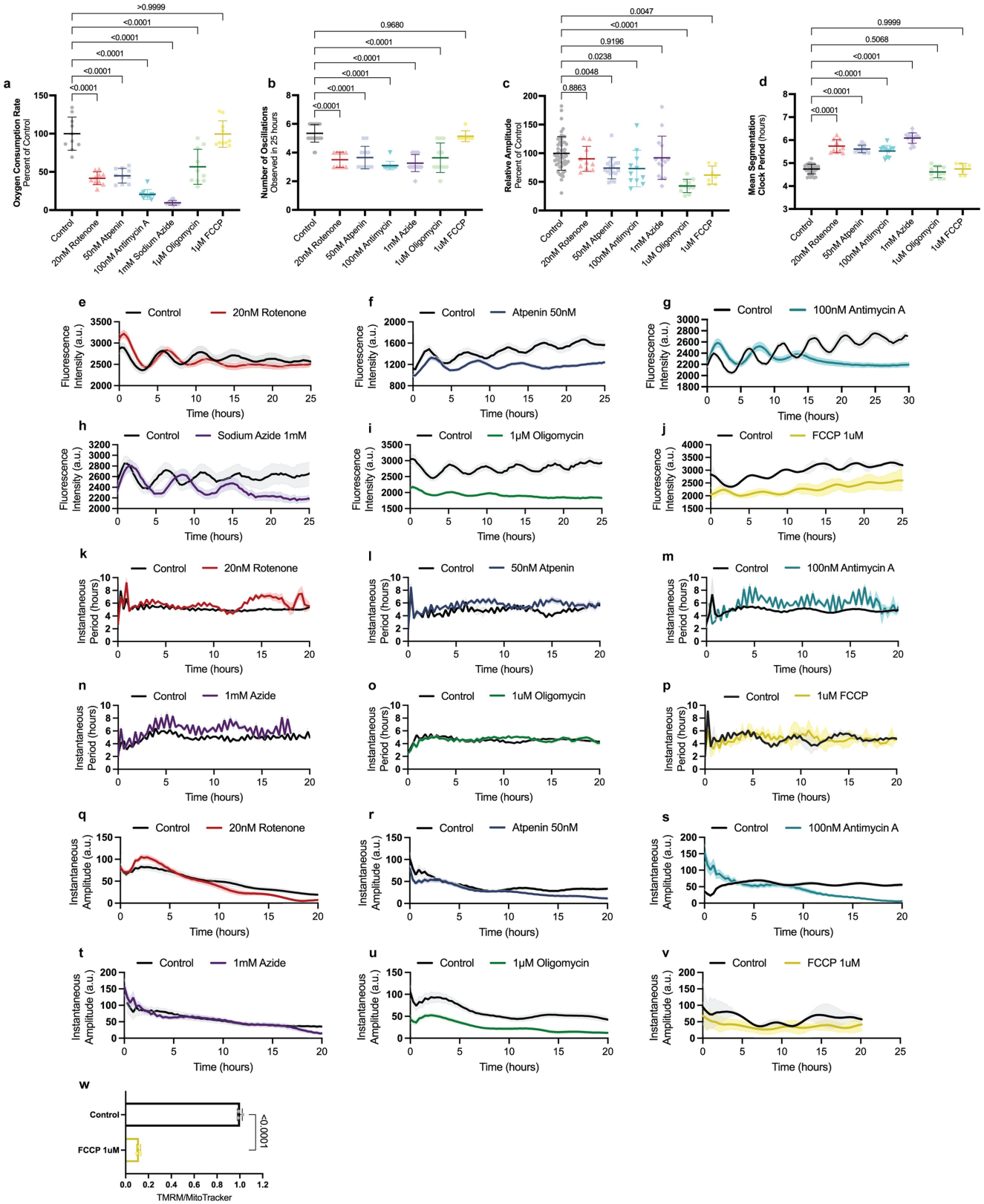

Extended Data Fig. 5 | See next page for caption.

Extended Data Fig. 5 | Effect of electron transport chain inhibitors on the segmentation clock. a. Basal oxygen consumption rate in human PSM cells treated with vehicle control (DMSO), 20nM rotenone, 50 nM atpenin A5, 100 nM antimycin A, 1 mM sodium azide, 1 μM oligomycin or 1 μM FCCP. Mean ±SD. n = 10 biological replicates. One-way ANOVA with Šidák correction: control vs. rotenone $p = 5.4 \times 10^{-12}$, control vs. atpenin $p = 4.3 \times 10^{-11}$, control vs. antimycin $p = 3.8 \times 10^{-18}$, control vs. azide $p = 1.04 \times 10^{-20}$, control vs. oligomycin $p = 5.9 \times 10^{-8}$, control vs. FCCP p = 0.999. b. Number of HES7-Achilles oscillations observed in 25 h for human PSM cells treated with vehicle control (DMSO, n = 29), 20 nM rotenone (n = 10), 50 nM atpenin A5 (n = 17), 100 nM antimycin A (n = 11), 1 mM sodium azide (n = 15), 1 μM oligomycin (n = 11), or 1 μM FCCP (n = 7). n denotes independent experiments. Mean ±SD. One-way ANOVA with Šidák correction: control vs. rotenone $p = 1.1 \times 10^{-10}$, control vs. atpenin $p = 2.3 \times 10^{-12}$, control vs. antimycin $p = 6.1 \times 10^{-15}$, control vs. azide $p = 2.0 \times 10^{-15}$, control vs. oligomycin $p = 4.7 \times 10^{-10}$. c. Mean amplitude expressed as a percent of control for HES7-Achilles oscillations in human PSM cells treated with vehicle control (DMSO, n = 53), 20 nM rotenone (n = 10), 50 nM atpenin A5 (n = 18), 100 nM antimycin A (n = 11), 1 mM sodium azide (n = 14), 1 μM oligomycin (n = 11), or 1 μM FCCP (n = 7). n denotes independent experiments. Mean ±SD. One-way ANOVA with Dunnett correction: control vs. oligomycin $p = 3.4 \times 10^{-8}$. d. Mean segmentation clock period as calculated by Hilbert transformation for human PSM cells treated with vehicle control (DMSO, n = 53), 20 nM rotenone (n = 10), 50 nM atpenin A5 (n = 18), 100 nM antimycin A (n = 11), 1 mM sodium azide (n = 14), 1 μM oligomycin (n = 11), or 1 μM FCCP (n = 7). n denotes independent experiments. Mean ±SD. One-way ANOVA with Šidák correction: control vs. rotenone $p = 8.9 \times 10^{-21}$, control vs. atpenin $p = 1.8 \times 10^{-18}$, control vs. antimycin $p = 2 \times 10^{-15}$, control vs. azide $p = 1.4 \times 10^{-33}$. e. HES7-Achilles oscillatory profile in human PSM cultures treated with DMSO control (n = 10) or 20 nM rotenone (n = 11). n denotes independent experiments. Mean ±SEM. f. HES7-Achilles oscillatory profile in human PSM cultures treated with DMSO control (n = 12) or 50 nM atpenin A5 (n = 18). n denotes independent experiments. Mean ±SEM. g. HES7-Achilles oscillatory profile in human PSM cultures treated with DMSO control (n = 11) or 100 nM antimycin A (n = 13). n denotes independent experiments. Mean ±SEM. h. HES7-Achilles oscillatory profile in human PSM cultures treated with DMSO control (n = 9) or 1 mM sodium azide (n = 15). n denotes independent experiments. Mean ±SEM. i. HES7-Achilles oscillatory profile in human PSM cultures treated with DMSO control (n = 12) or 1 μM oligomycin (n = 17). n denotes independent experiments. Mean ±SEM. j. HES7-Achilles oscillatory profile in human PSM cultures treated with DMSO control (n = 3) or 1 μM FCCP (n = 7). n denotes independent experiments. Mean ±SEM. k. Instantaneous HES7-Achilles oscillatory period over time as calculated by Hilbert transformation in human PSM cultures treated with DMSO control (n = 10) or 20 nM rotenone (n = 11). n denotes independent experiments. Mean ±SEM. l. Instantaneous HES7-Achilles oscillatory period over time as calculated by Hilbert transformation in human PSM cultures treated with DMSO control (n = 12) or 50 nM atpenin A5 (n = 18). n denotes independent experiments. Mean ±SEM. m. Instantaneous HES7-Achilles oscillatory period over time as calculated by Hilbert transformation in human PSM cultures treated with DMSO control (n = 11) or 100 nM antimycin A (n = 13). n denotes independent experiments. Mean ±SEM. n. Instantaneous HES7-Achilles oscillatory period over time as calculated by Hilbert transformation in human PSM cultures treated with DMSO control (n = 9) or 1 mM sodium azide (n = 15). n denotes independent experiments. Mean ±SEM. o. Instantaneous HES7-Achilles oscillatory period over time as calculated by Hilbert transformation in human PSM cultures treated with DMSO control (n = 12) or 1 μM oligomycin (n = 17). n denotes independent experiments. Mean ±SEM. p. Instantaneous HES7-Achilles oscillatory period over time as calculated by Hilbert transformation in human PSM cultures treated with DMSO control (n = 3) or 1 μM FCCP (n = 7). n denotes independent experiments. Mean ±SEM. q. Instantaneous HES7-Achilles oscillatory amplitude over time as calculated by Hilbert transformation in human PSM cultures treated with DMSO control (n = 10) or 20 nM rotenone (n = 11). n denotes independent experiments. Mean ±SEM. r. Instantaneous HES7-Achilles oscillatory amplitude over time as calculated by Hilbert transformation in human PSM cultures treated with DMSO control (n = 12) or 50 nM atpenin A5 (n = 18). n denotes independent experiments. Mean ±SEM. s. Instantaneous HES7-Achilles oscillatory amplitude over time as calculated by Hilbert transformation in human PSM cultures treated with DMSO control (n = 11) or 100 nM antimycin A (n = 13). n denotes independent experiments. Mean ±SEM. t. Instantaneous HES7-Achilles oscillatory amplitude over time as calculated by Hilbert transformation in human PSM cultures treated with DMSO control (n = 9) or 1 mM sodium azide (n = 15). n denotes independent experiments. Mean ±SEM. u. Instantaneous HES7-Achilles oscillatory amplitude over time as calculated by Hilbert transformation in human PSM cultures treated with DMSO control (n = 12) or 1 μM oligomycin (n = 17). n denotes independent experiments. Mean ±SEM. v. Instantaneous HES7-Achilles oscillatory amplitude over the time as calculated by Hilbert transformation in human PSM cultures treated with DMSO control (n = 3) or 1 μM FCCP (n = 7). n denotes independent experiments. Mean ±SEM. w. Inner mitochondrial membrane potential ($\Delta\Psi m$) in human PSM cells under control conditions or treated acutely with 1 μM FCCP. TMRM fluorescence was normalized by mitochondrial content (MitoTracker Green) following flow cytometry. Mean ±SD. n = 3 biological replicates. Unpaired two-sided t-test: $p = 6.4 \times 10^{-7}$.

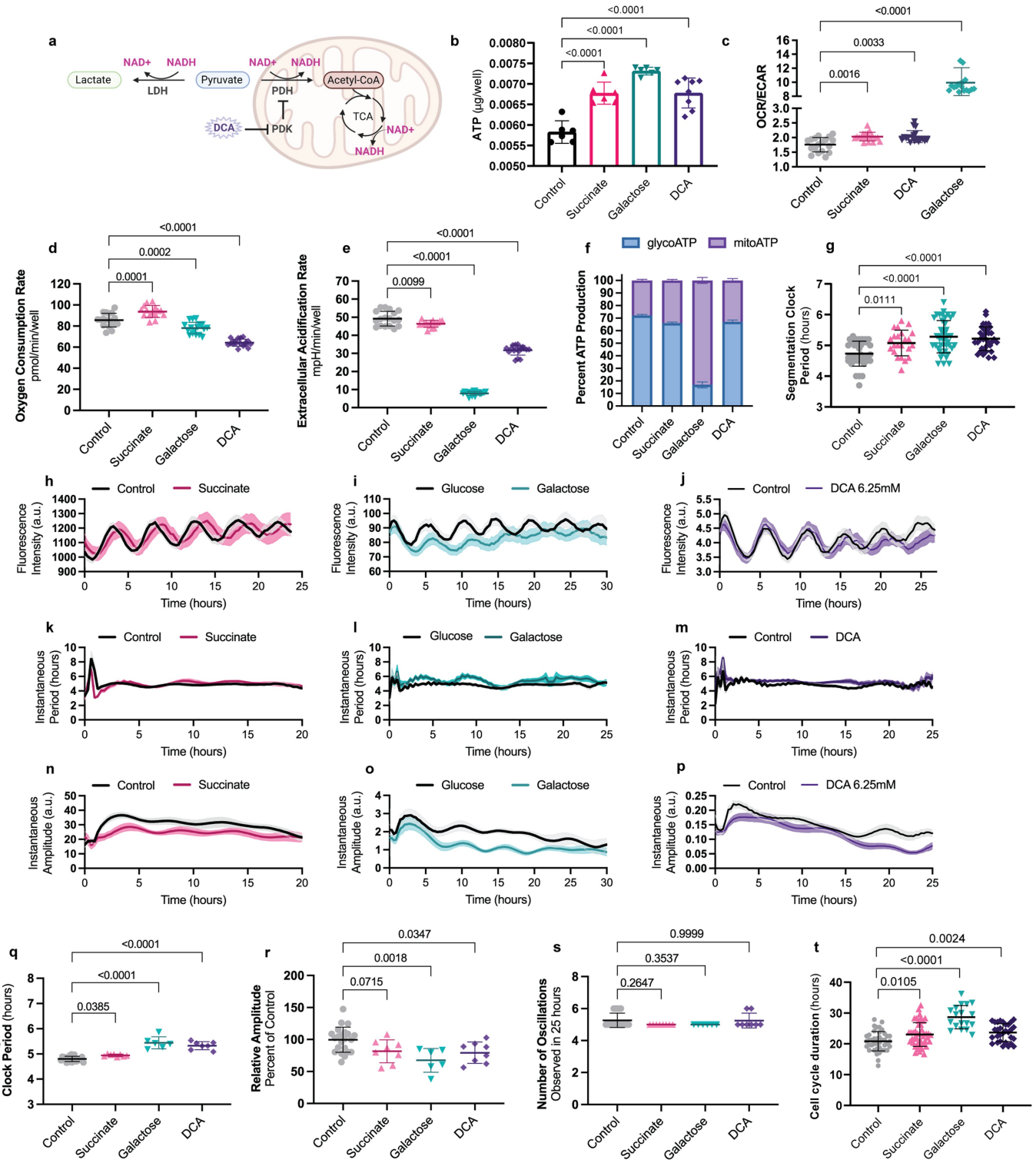

Extended Data Fig. 6 | See next page for caption.

Extended Data Fig. 6 | Increased ATP concentrations do not accelerate the segmentation clock. a. Illustration depicting the alternate fates of pyruvate and their regulation by metabolic enzymes. Lactate dehydrogenase (LDH) converts pyruvate to lactate and regenerates NAD^+ from NADH. Pyruvate dehydrogenase (PDH) oxidizes pyruvate to acetyl coenzyme-A (acetyl-CoA) in the mitochondria and consumes NAD^+. Acetyl -CoA then enters the tricarboxylic acid (TCA) cycle, which also consumes NAD^+. Pyruvate dehydrogenase kinase (PDK) inhibits PDH by phosphorylating it. DCA is a PDK inhibitor that promotes the conversion of pyruvate to acetyl-CoA by relieving PDH inhibition. Created with BioRender.com. b. ATP content per well for human PSM cells in control (water; n = 6), 25 mM succinate supplementation (n = 6), 10 mM galactose in the absence of glucose (n = 6), and 6.25 mM DCA (n = 8) conditions after 24 h of culture. In each case, 30,000 cells were seeded per assay well. Each datapoint represents the average of 3 technical replicates. Mean ±SD. One-way ANOVA with Šidák correction: control vs. succinate $p = 2 \times 10^{-5}$, control vs. galactose $p = 1.6 \times 10^{-8}$, control vs. DCA $p = 7.4 \times 10^{-6}$. c. Ratio of Oxygen consumption rate (OCR) to extracellular acidification rate (ECAR) in human PSM cells treated with water control (n-18), 25 mM succinate (n = 15), 6.25 mM DCA (n = 18), or cultured with 10 mM galactose instead of glucose (n = 18) for 24 h. Mean ±SD. One-way Brown-Forsythe and Welch ANOVA with Dunnett T3 correction: control vs. galactose $p = 2.5 \times 10^{-12}$. d. Oxygen consumption rate (OCR) in human PSM cells treated with water control (n = 18), 25 mM succinate (n = 15), 6.25 mM DCA (n = 18), or cultured with 10mM galactose instead of glucose (n = 18) for 24 h. Mean ±SD. One-way ANOVA with Dunnett correction: control vs. DCA $p = 3.8 \times 10^{-18}$. e. Extracellular acidification rate (ECAR) in human PSM cells treated with water control (n = 18), 25 mM succinate (n = 15), 6.25 mM DCA (n = 18), or cultured with 10 mM galactose instead of glucose (n = 18) for 24 h. Mean ±SD. One-way ANOVA with Šidák correction: control vs. galactose $p = 3.05 \times 10^{-51}$, control vs. DCA $p = 1 \times 10^{-28}$. f. Percent of total ATP production corresponding to glycolysis (glycoATP) or mitochondrial respiration (mitoATP) in human PSM cells treated with water control (n = 6), 25 mM succinate (n = 5), 6.25 mM DCA (n = 6), or cultured with 10 mM galactose instead of glucose (n = 6) for 24 h. Mean ±SD. g. HES7-Achilles oscillatory period in human PSM cells treated with vehicle control (water; n = 36), 25 mM succinate (n = 23), 10 mM galactose in the absence of glucose (n = 43), and 6.25 mM DCA (n = 34). Mean ±SD. One-way ANOVA with Šidák correction: control vs. galactose $p = 5.9 \times 10^{-7}$, control vs. DCA $p = 3.1 \times 10^{-5}$. h. HES7-Achilles oscillatory profile in human PSM cells cultured under control conditions or supplemented with 25 mM succinate. Mean ±SEM. n = 8. i. HES7-Achilles oscillatory profile in human PSM cells cultured with either 10 mM glucose or 10 mM galactose. Mean ±SEM. n = 6. j. HES7-Achilles oscillatory profile in human PSM cultures under control conditions (n = 9) or 6.25 mM DCA (n = 8). Mean ±SEM. k. Instantaneous HES7-Achilles oscillatory period over time as calculated by Hilbert transformation in human PSM cells cultured under control conditions or supplemented with 25 mM succinate. Mean ±SEM. n = 8. l. Instantaneous HES7-Achilles oscillatory period over time as calculated by Hilbert transformation in human PSM cells cultured with either 10 mM glucose or 10 mM galactose. Mean ±SEM. n = 6. m. Instantaneous HES7-Achilles oscillatory period over time as calculated by Hilbert transformation in human PSM cells cultured under control conditions (n = 9) or supplemented with 6.25 mM DCA (n = 7). Mean ±SEM. n. Instantaneous HES7-Achilles oscillatory amplitude over time as calculated by Hilbert transformation in human PSM cells cultured under control conditions or supplemented with 25 mM succinate. Mean ±SEM. n = 8. o. Instantaneous HES7-Achilles oscillatory amplitude over time as calculated by Hilbert transformation in human PSM cells cultured with either 10 mM glucose or 10 mM galactose. Mean ±SEM. n = 6. p. Instantaneous HES7-Achilles oscillatory amplitude over time as calculated by Hilbert transformation in human PSM cells cultured under control conditions (n = 9) or supplemented with 6.25 mM DCA (n = 8). Mean ±SEM. q. Mean segmentation clock period as calculated by Hilbert transformation for human PSM cells treated with vehicle control (water; n = 21), 25 mM succinate (n = 8), 10 mM galactose in the absence of glucose (n = 6), and 6.25 mM DCA (n = 8). n denotes independent experiments. Mean ±SD. One-way ANOVA with Šidák correction: contro vs. galactose $p = 3.3 \times 10^{-12}$, control vs. DCA $p = 1.4 \times 10^{-10}$. r. Mean amplitude expressed as a percent of control for HES7-Achilles oscillations in human PSM cells treated with vehicle control (water; n = 22), 25 mM succinate (n = 8), 10 mM galactose in the absence of glucose (n = 6), and 6.25 mM DCA (n = 7). n denotes independent experiments. Mean ±SD. One-way ANOVA with Dunnett correction. s. Number of HES7-Achilles oscillations observed in 25 h for human PSM cells treated with vehicle control (water; n = 23), 25 mM succinate (n = 8), 10 mM galactose in the absence of glucose (n = 6), and 6.25 mM DCA (n = 8). n denotes independent experiments. Mean ±SD. One-way ANOVA with Dunnett correction. t. Duration of the cell cycle in hours for human PSM cells treated with vehicle control (DMSO; n = 42), 25 mM succinate (n = 44), 10 mM galactose in the absence of glucose (n = 18), and 6.25 mM DCA (n = 30). Mean ±SD. One-way ANOVA with Dunnett correction: control vs. galactose $p = 1.2 \times 10^{-12}$.

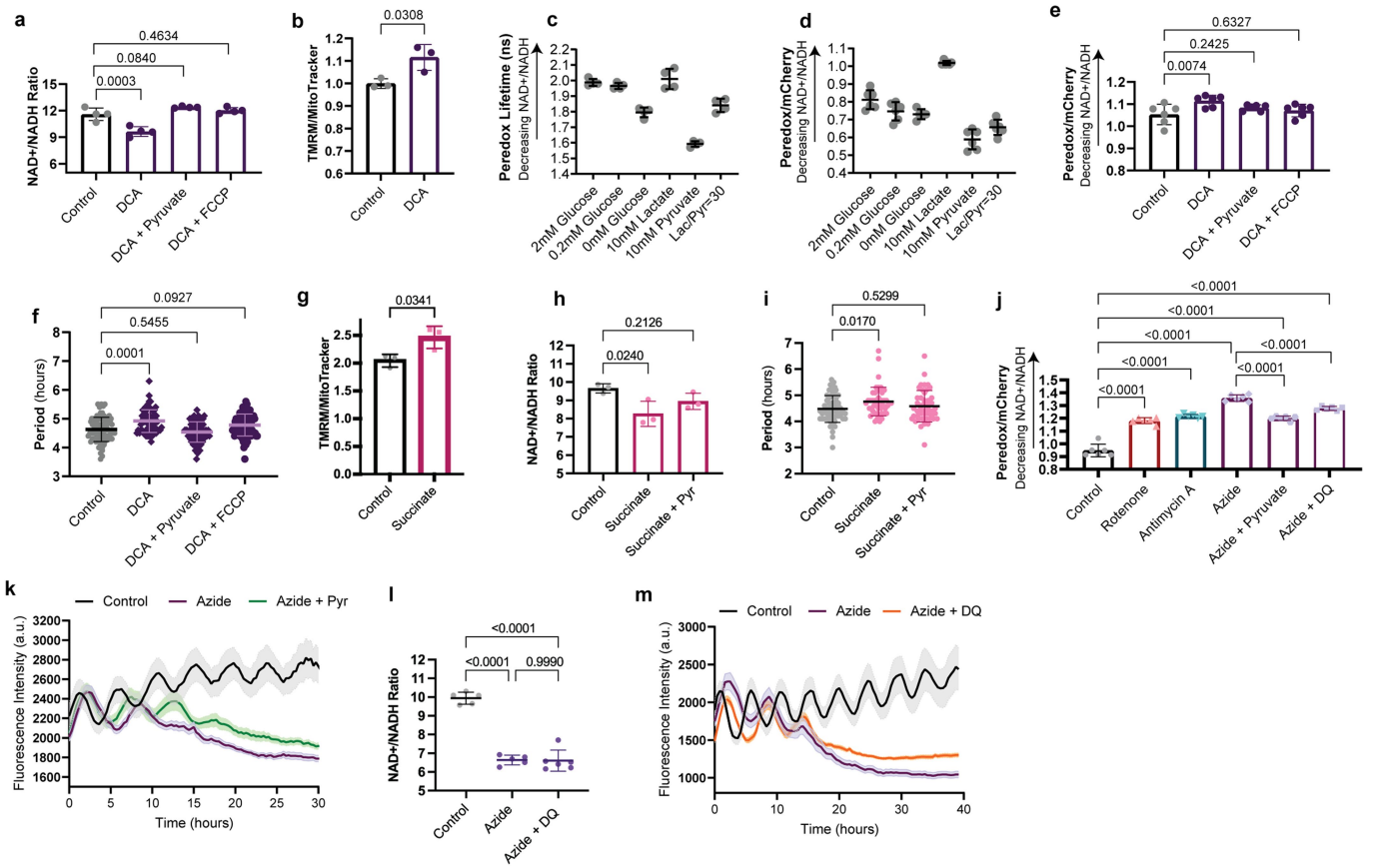

Extended Data Fig. 7 | Rescue of the segmentation clock period by restoration of the NAD$^+$/NADH ratio. a. Whole-cell NAD$^+$/NADH ratio in vehicle-treated human PSM cells and cells treated with either 6.25 mM DCA alone or DCA in combination with 1 mM sodium pyruvate or 10 nM FCCP for 24 h. Each datapoint represents the average of 3 technical replicates. Mean ±SD. n = 4. One-way ANOVA with Dunnett correction. b. Inner mitochondrial membrane potential (ΔΨm) in human PSM cells under control conditions or treated with 6.25 mM DCA for 24 h. TMRM fluorescence was normalized by mitochondrial content (MitoTracker Green) following flow cytometry. Mean ±SD. n = 3 biological replicates. Unpaired two-sided t-test. c. Peredox-mCherryNLS fluorescence lifetime in human PSM cells cultured acutely in a balanced salt solution and supplemented with the indicated concentrations of glucose, lactate or pyruvate. Mean ±SD. n = 4 biological replicates. d. Ratiometric Peredox-to-mCherry fluorescence signal in human PSM cells cultured acutely in a balanced salt solution and supplemented with the indicated concentrations of glucose, lactate or pyruvate. Mean ±SD. n = 6 biological replicates. e. Ratiometric Peredox/mCherry signal in vehicle-treated human PSM cells and cells treated with either 6.25 mM DCA alone or DCA in combination with 1 mM sodium pyruvate or 10 nM FCCP for 24 h. Each datapoint represents the average of >200 individual cells analyzed within a biological replicate. Mean ±SD. n = 6 biological replicates. One-way ANOVA with Dunnett correction. f. HES7-Achilles oscillatory period in human PSM cells treated with vehicle control (water; n = 78), 6.25 mM DCA alone (n = 68), DCA with 1 mM sodium pyruvate (n = 73), and DCA with 10 nM FCCP (n = 85). Mean ±SD. One-way ANOVA with Dunnett correction. g. Inner mitochondrial membrane potential (ΔΨm) in human PSM cells under control conditions or treated with 25 mM succinate for 24 h. TMRM fluorescence was normalized by mitochondrial content (MitoTracker Green) following flow cytometry. Mean ±SD. n = 3 biological replicates. Unpaired two-sided t-test. h. Whole-cell NAD$^+$/NADH ratio in vehicle-treated human PSM cells and cells treated with either 25 mM succinate alone or succinate in combination with 1 mM sodium pyruvate for 24 h. Each datapoint represents the average of 3 technical replicates. Mean ±SD. n = 3 biological replicates. One-way ANOVA with Dunnett correction. i. HES7-Achilles oscillatory period in human PSM cells treated with vehicle control (water; n = 62), 25 mM succinate alone (n = 46), or succinate with 1 mM sodium pyruvate (n = 46). Mean ±SD. One-way ANOVA with Dunnett correction. j. Ratiometric Peredox/mCherry signal in DMSO-treated human PSM cells and cells treated with 20 nM rotenone, 100 nM antimycin A, 1 mM sodium azide alone, azide with 1 mM sodium pyruvate, and azide with 5 µM duroquinone (DQ) for 24 h. Each datapoint represents the average of >200 individual cells analyzed in a biological replicate. Mean ±SD. n = 6. One-way ANOVA with Šidák correction: control vs. rotenone p = 2.9 × 10-15, control vs. antimycin p = 7.1×10^{-17}, control vs. azide p = 4.4×10^{-22}, control vs. azide+pyr p = 3.3×10^{-16}, control vs. azide+DQ p = 2.2×10^{-19}, azide vs. azide+pyr p = 9.7×10^{-10}, azide vs. azide+DQ p = 5.3×10^{-6}. k. HES7-Achilles oscillatory profile in human PSM cells cultures treated with DMSO control (n = 10), 1 mM sodium azide alone (n = 13), and azide with 1mM sodium pyruvate (n = 13). Mean ±SEM. l. Whole-cell NAD+/NADH ratio in human PSM cells treated with vehicle-control (n = 5), 1 mM sodium azide alone (n = 5), or azide with 5 µM duroquinone (DQ) (n = 6) for 24 h. Each datapoint represents the average of 3 technical replicates. Mean ±SD. One-way ANOVA with Tukey correction: control vs. azide p = 3.5×10^{-8}, control vs. azide+DQ p = 1.8×10^{-8}. m. HES7-Achilles oscillatory profile in human PSM cells cultures treated with DMSO control (n = 11), 1 mM sodium azide alone (n = 19), and azide with 5 µM duroquinone (n = 21). Mean ±SEM.

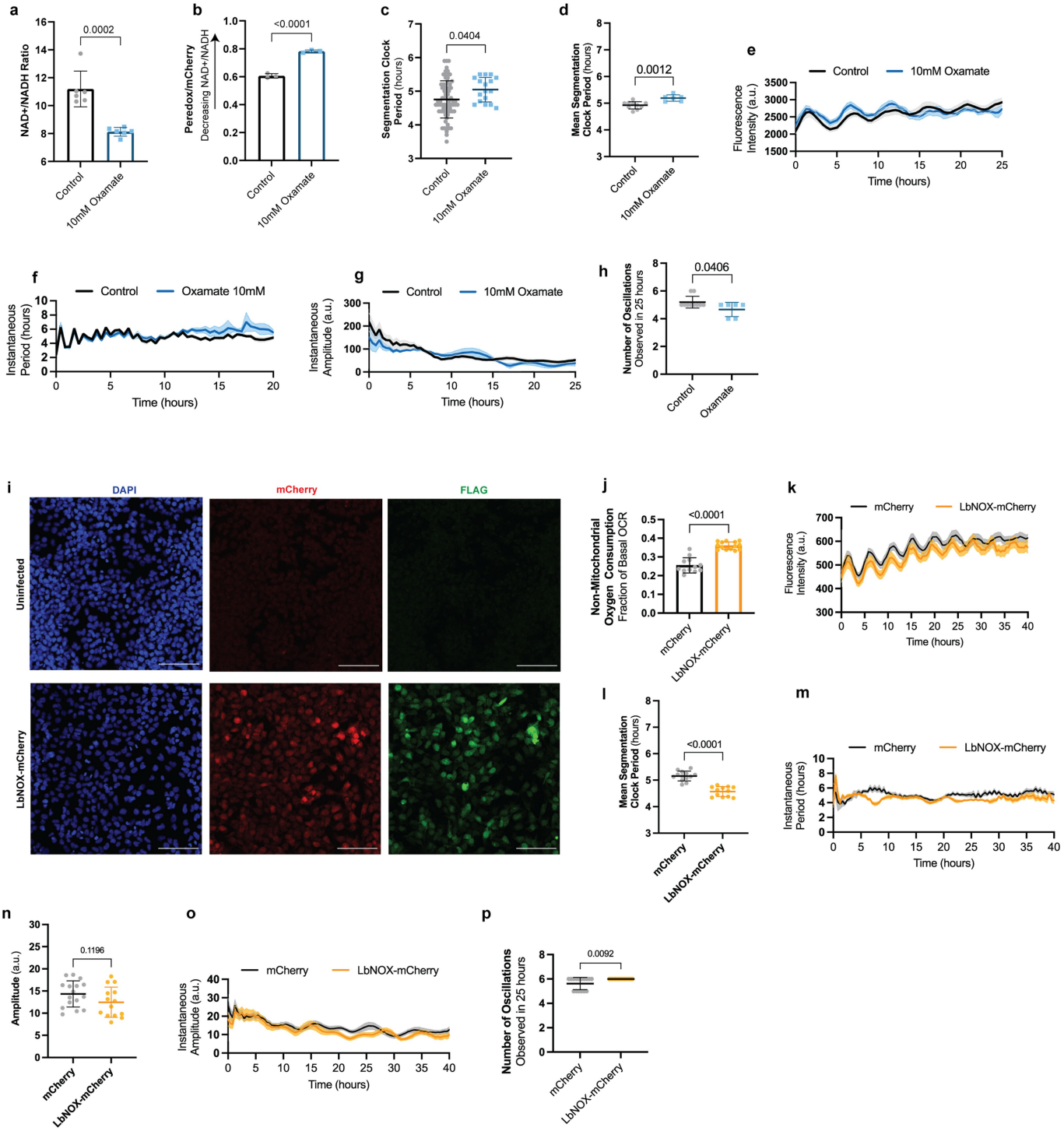

Extended Data Fig. 8 | See next page for caption.

Extended Data Fig. 8 | Modulation of the segmentation clock period by direct manipulation of the NAD$^+$/NADH ratio. a. Whole-cell NAD$^+$/NADH ratio human PSM cells under control conditions or treated acutely with 10mM oxamate. Each datapoint represents the average of 3 technical replicates. Mean ±SD. n = 6. Unpaired two-sided t-test. b. Ratiometric Peredox/mCherry signal in human PSM cells cultured under control conditions or treated acutely with 10 mM oxamate. Each datapoint represents the average of >200 individual cells analyzed within a biological replicate. Mean ±SD. n = 3. Unpaired two-sided t-test, $p = 8.3 \times 10^{-5}$. c. Period of HES7-Achilles oscillations in human PSM cells cultures treated with water control (n = 73) or 10 mM sodium oxamate (n = 17). Mean ±SEM. Unpaired two-sided t-test. d. Mean segmentation clock period as calculated by Hilbert transformation for human PSM cells cultures treated with water control (n = 10) or 10 mM sodium oxamate (n = 6). n denotes independent experiments. Mean ±SD. Unpaired two-sided t-test. e. HES7-Achilles oscillatory profile in human PSM cells cultures treated with water control (n = 10) or 10 mM sodium oxamate (n = 3). n denotes independent experiments. Mean ±SEM. f. Instantaneous HES7-Achilles oscillatory period over time as calculated by Hilbert transformation in human PSM cells cultures treated with water control (n = 10) or 10 mM sodium oxamate (n = 3). n denotes independent experiments. Mean ±SEM. g. Instantaneous HES7-Achilles oscillatory amplitude over time as calculated by Hilbert transformation in human PSM cells cultures treated with water control (n = 10) or 10 mM sodium oxamate (n = 3). n denotes independent experiments. Mean ±SEM. h. Number of HES7-Achilles oscillations observed in 25 h in human PSM cells cultures treated with water control (n = 10) or 10 mM sodium oxamate (n = 6). n denotes independent experiments. Mean ±SD. Unpaired two-sided t-test. i. Representative micrographs of DAPI nuclear stain, mCherry endogenous fluorescence, and anti-FLAG immunofluorescence (LbNOX is flag-tagged in the C terminus[28]) in human PSM cells subjected to mock transduction (top) or transduced with LbNOX-mCherry (bottom). Similar results were obtained n = 15 times. Scale bar = 100 µm. j. Non-mitochondrial oxygen consumption in human PSM cells transduced with a lentivirus expressing either mCherry alone (n = 12) or LbNOX in combination with mCherry (n = 14). OCR after addition of 0.5 µM rotenone and 0.5 µM antimycin A is expressed as fraction of basal OCR. Mean ±SD. Unpaired two-sided t-test: $p = 1.04 \times 10^{-8}$. k. HES7-Achilles oscillatory profile over the course of 40 h for human PSM cells transduced with a lentivirus expressing either mCherry alone (n = 16) or LbNOX in combination with mCherry (n = 14). Mean ±SEM. l. Mean segmentation clock period as calculated by Hilbert transformation for human PSM cells transduced with a lentivirus expressing either mCherry alone (n = 13) or LbNOX in combination with mCherry (n = 12). Mean ±SD. Unpaired two-sided t-test: $p = 4.87 \times 10^{-8}$. m. Instantaneous HES7-Achilles oscillatory period over time as calculated by Hilbert transformation in human PSM cells transduced with a lentivirus expressing either mCherry alone (n = 13) or LbNOX in combination with mCherry (n = 12). Mean ±SD. n. Mean HES7-Achilles oscillation amplitude in human PSM cells transduced with a lentivirus expressing either mCherry alone (n = 16) or LbNOX in combination with mCherry (n = 14). Mean ±SD. Unpaired two-sided t-test. o. Instantaneous HES7-Achilles oscillatory amplitude over time as calculated by Hilbert transformation in human PSM cells transduced with a lentivirus expressing either mCherry alone (n = 16) or LbNOX in combination with mCherry (n = 14). Mean ±SD. p. Number of oscillations (peaks) observed in 25 h for human PSM cells transduced with a lentivirus expressing either mCherry alone (n = 16) or LbNOX in combination with mCherry (n = 14). Mean ±SD. Unpaired two-sided t-test.

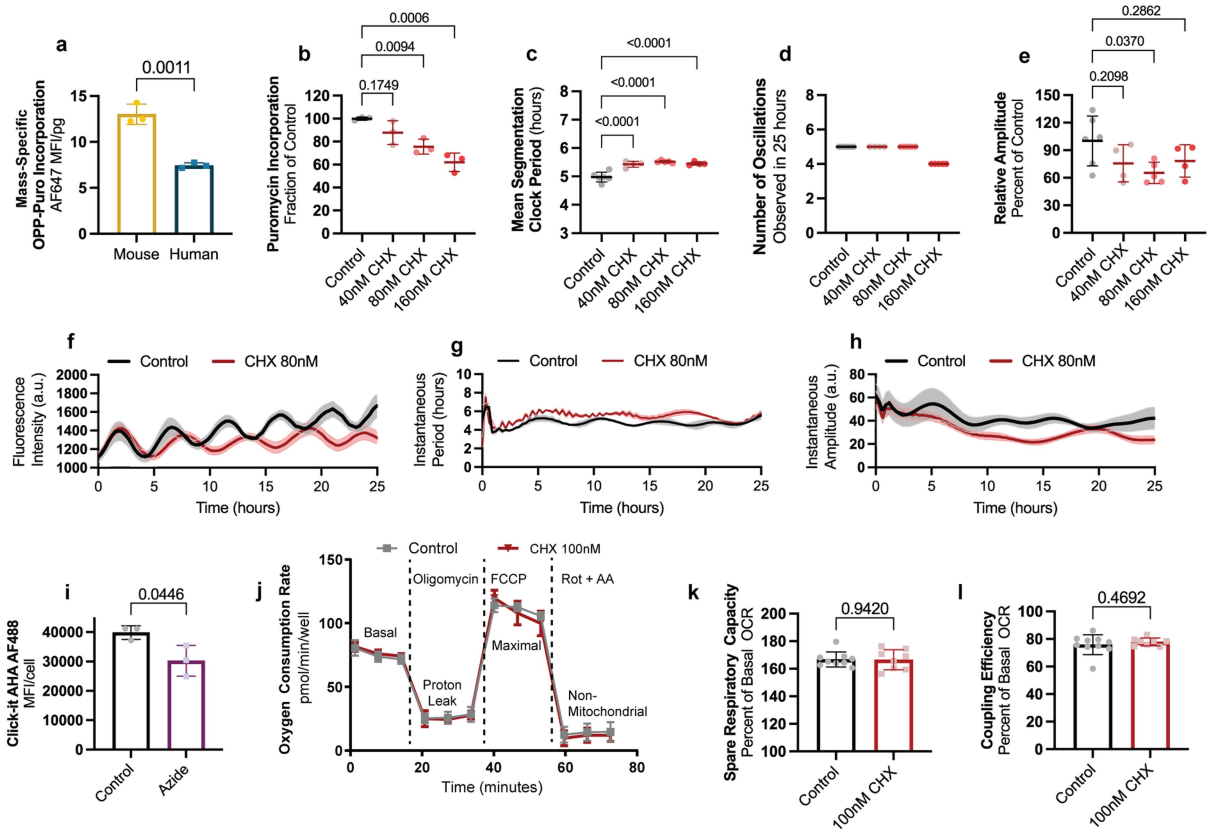

Extended Data Fig. 9 | The segmentation clock is sensitive to the rate of translation. a. Mass-specific OPP-Puromycin incorporation as a measure of global translation rate in MSGN1-Venus+ PSC-derived mouse and human PSM cells. OPP-Puromycilated peptides were detected by click chemistry with AlexaFluor647-Picoyl Azide. Mean ±SD. n = 3 biological replicates. Unpaired two-sided t-test. b. Translation rate as measured by puromycin incorporation expressed as percent of control for human PSM cells treated with DMSO, 40 nM, 80 nM or 160 nM cycloheximide (CHX) for 24 h. Mean ±SD. n = 3 biological replicates. One-way ANOVA with Dunnett correction. c. Mean segmentation clock period as calculated by Hilbert transformation for human PSM cells treated with DMSO (n = 6), 40 nM (n = 4), 80 nM (n = 5) or 160 nM (n = 4) cycloheximide (CHX) for 24 h. n denotes independent experiments. Mean ±SD. One-way ANOVA with Šidák correction: control vs. 40 nM $p = 7.6 \times 10^{-5}$, control vs. 80 nM $p = 4.5 \times 10^{-6}$, control vs. 160 nM $p = 4.2 \times 10^{-5}$. d. Number of HES7-Achilles oscillations observed in 25 h in human PSM cells treated with DMSO (n = 6), 40 nM (n = 4), 80 nM (n = 5) or 160 nM (n = 5) cycloheximide (CHX) for 24 h. n denotes independent experiments. Mean ±SD. e. Mean amplitude expressed as a percent of control in human PSM cells treated with DMSO (n = 6), 40 nM (n = 4), 80 nM (n = 5) or 160 nM (n = 4) cycloheximide (CHX) for 24 h. n denotes independent experiments. Mean ±SD. One-way ANOVA with Dunnett correction. f. HES7-Achilles oscillatory profile for human PSM cells treated with DMSO-control (n = 3) or 80 nM cycloheximide (CHX; n = 5). n denotes independent experiments. Mean ±SEM. g. Instantaneous HES7-Achilles oscillatory period over time as calculated by Hilbert transformation for human PSM cells treated with DMSO-control (n = 3) or 80 nM cycloheximide (CHX, n = 5). n denotes independent experiments. Mean ±SEM. h. Instantaneous HES7-Achilles oscillatory amplitude over time as calculated by Hilbert transformation for human PSM cells treated with DMSO-control (n = 3) or 80 nM cycloheximide (CHX, n = 5). n denotes independent experiments. Mean ±SEM. i. Translation rate as measured by incorporation of the methionine analog AHA in human PSM cells treated with either DMSO control or 1mM sodium azide for one hour. Mean ±SD. n = 3 biological replicates. Unpaired two-sided t-test. j. Oxygen consumption rate measured over the course of the mitochondrial stress test for human PSM cells treated with DMSO control or 100 nM cycloheximide for 24 h. 1 µM Oligomycin, 1 µM FCCP, and 0.5 µM Rotenone + 0.5 µM Antimycin A were added at the timepoints marked by dotted lines. Mean ±SD. n = 9 biological replicates. k. Spare respiratory capacity in human PSM cells treated with vehicle control (DMSO) or 100 nM cycloheximide (CHX) for 24 h. Mean ±SD. n = 8 biological replicates. Unpaired two-sided t-test. l. Coupling efficiency shown as the percent of basal oxygen consumption that is linked to ATP production in human PSM cells treated with vehicle control (DMSO) or 100 nM cycloheximide (CHX) for 24 h. Mean ±SD. n = 8 biological replicates. Unpaired two-sided t-test.

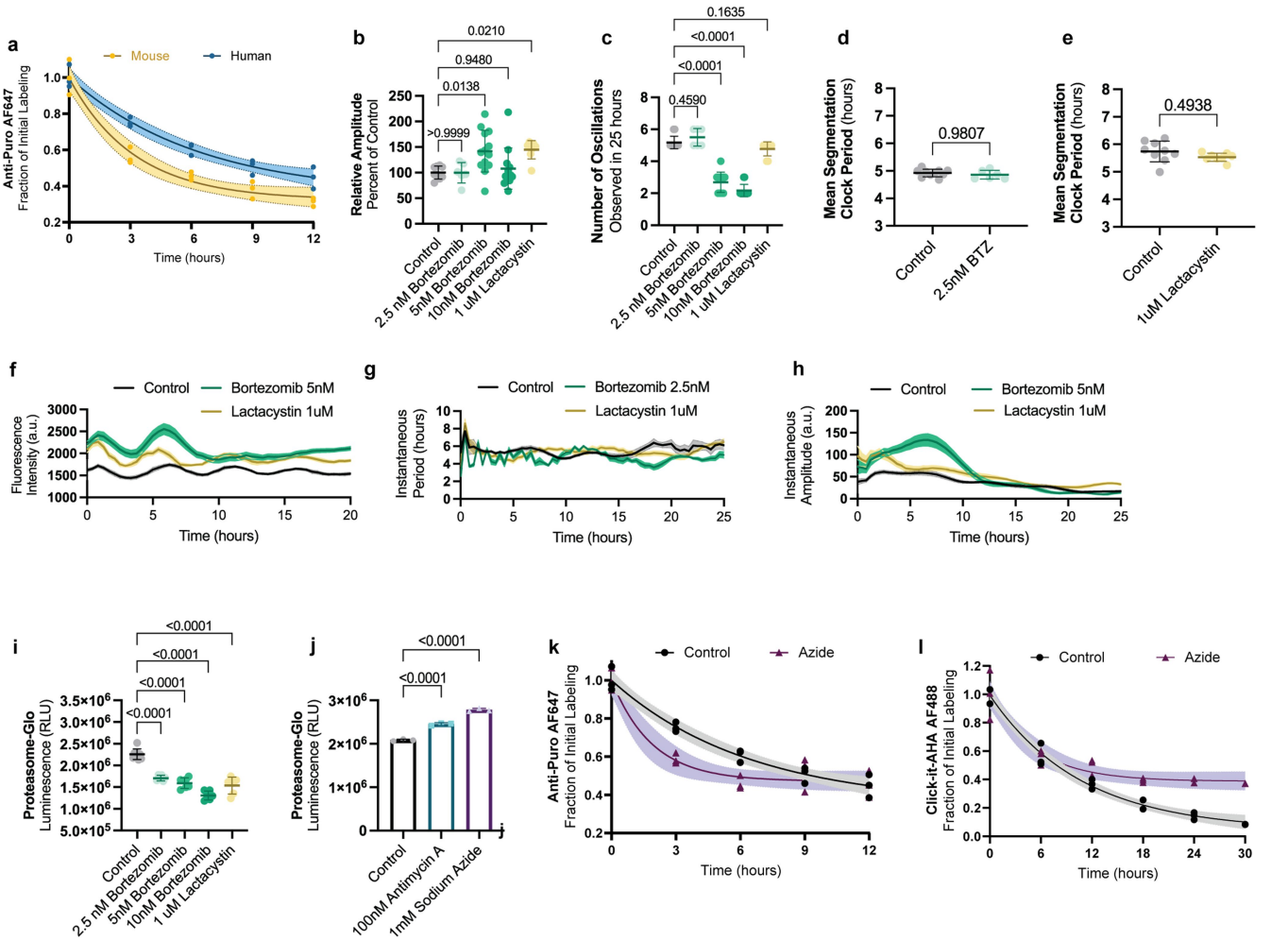

Extended Data Fig. 10 | Protein stability differences between mouse and human PSM cells. a. Pulse-chase experiment tracking the degradation of puromycylated peptides over the course of 12 h in MSGN1-Venus+ PSC-derived mouse and human PSM cells following a 1-hour pulse with puromycin. Solid line represents best one-phase decay fit with the 95% confidence intervals shown as shaded regions. n = 3 independent experiments. b. Mean amplitude expressed as a percent of control in human PSM treated with DMSO control (n = 9), 2.5 nM (n = 6), 5 nM (n = 13) or 10 nM (n = 12) bortezomib, or 1 μM lactacystin (n = 8). n denotes independent experiments. Mean ±SD. One-way ANOVA with Dunnett correction. c. Number of HES7-Achilles oscillations observed in 25 h in human PSM treated with DMSO control (n = 17), 2.5 nM (n = 6), 5 nM (n = 13) or 10 nM (n = 12) bortezomib, or 1 μM lactacystin (n = 9). n denotes independent experiments. Mean ±SD. One-way ANOVA with Šidák correction: control vs. 5 nM bortezomib $p = 2.4 \times 10^{-19}$, control vs. 10 nM bortezomib $p = 1.8 \times 10^{-22}$. d. Mean segmentation clock period as calculated by Hilbert transformation for human PSM cells treated with DMSO control (n = 10) or 2.5 nM bortezomib (BTZ, n = 6). n denotes independent experiments. Mean ±SD. Unpaired two-sided t-test. e. Mean segmentation clock period as calculated by Hilbert transformation for human PSM cells treated with DMSO control (n = 9) or 1 μM lactacystin (n = 8). n denotes independent experiments. Mean ±SD. Unpaired two-sided t-test. f. HES7-Achilles oscillatory profile for human PSM cells treated with DMSO-control (n = 9), 5 nM bortezomib (n = 13), or 1 μM lactacystin (n = 8). Mean ±SEM. g. stantaneous HES7-Achilles oscillatory period over time as calculated by Hilbert transformation for human PSM cells treated with DMSO-control (n = 9), 2.5 nM bortezomib (n = 6), or 1 μM lactacystin (n = 8). Mean ±SEM. h. Instantaneous HES7-Achilles oscillatory amplitude over time as calculated by Hilbert transformation for human PSM cells treated with DMSO-control (n = 9), 5 nM bortezomib (n = 13), or 1 μM lactacystin (n = 8). Mean ±SEM. i. Proteasome activity cells as measured by cleavage of a luminogenic proteasome substrate in human PSM treated with DMSO control, 2.5 nM, 5 nM or 10 nM bortezomib, or 1 μM lactacystin for 24 h. Mean ±SD. n = 6 biological replicates. One-way ANOVA with Šidák correction: control vs. 2.5 nM bortezomib $p = 5.8 \times 10^{-8}$, control vs. 5 nM bortezomib $p = 1.2 \times 10^{-9}$, control vs. 10 nM bortezomib $p = 4.3 \times 10^{-13}$, control vs. 1 μM lactacystin $p = 2.2 \times 10^{-10}$. j. Proteasome activity cells as measured by cleavage of a luminogenic proteasome substrate in human PSM treated with DMSO control, 100 nM antimycin A, or 1 mM sodium azide for 24 h. Mean ±SD. n = 3 biological replicates. One-way ANOVA with Šidák correction: control vs. antimycin $p = 1.3 \times 10^{-5}$, control vs. azide $p = 3.1 \times 10^{-7}$. k. Pulse-chase experiment tracking the degradation of puromycylated peptides over the course of 12 h in human PSM cells treated with DMSO control or 1 mM sodium azide following a 1-hour pulse with puromycin. Solid line represents best one-phase decay fit with the 95% confidence intervals shown as shaded regions. n = 3 independent experiments. l. Pulse-chase experiment tracking the degradation of AHA-labeled proteins over the course of 30 h in human PSM cells treated with DMSO control of 1 mM sodium azide following a 1-hour pulse with AHA. Solid line represents best one-phase decay fit with the 95% confidence intervals shown as shaded regions. n = 3 independent experiments.

nature portfolio

Corresponding author(s): Margarete Diaz-Cuadros
Olivier Pourquie

Last updated by author(s): Oct 29, 2022

Reporting Summary

Nature Portfolio wishes to improve the reproducibility of the work that we publish. This form provides structure for consistency and transparency in reporting. For further information on Nature Portfolio policies, see our Editorial Policies and the Editorial Policy Checklist.

Statistics

For all statistical analyses, confirm that the following items are present in the figure legend, table legend, main text, or Methods section.

n/a	Confirmed	
☐	☒	The exact sample size (*n*) for each experimental group/condition, given as a discrete number and unit of measurement
☐	☒	A statement on whether measurements were taken from distinct samples or whether the same sample was measured repeatedly
☐	☒	The statistical test(s) used AND whether they are one- or two-sided *Only common tests should be described solely by name; describe more complex techniques in the Methods section.*
☒	☐	A description of all covariates tested
☐	☒	A description of any assumptions or corrections, such as tests of normality and adjustment for multiple comparisons
☐	☒	A full description of the statistical parameters including central tendency (e.g. means) or other basic estimates (e.g. regression coefficient) AND variation (e.g. standard deviation) or associated estimates of uncertainty (e.g. confidence intervals)
☐	☒	For null hypothesis testing, the test statistic (e.g. *F*, *t*, *r*) with confidence intervals, effect sizes, degrees of freedom and *P* value noted *Give P values as exact values whenever suitable.*
☒	☐	For Bayesian analysis, information on the choice of priors and Markov chain Monte Carlo settings
☒	☐	For hierarchical and complex designs, identification of the appropriate level for tests and full reporting of outcomes
☒	☐	Estimates of effect sizes (e.g. Cohen's *d*, Pearson's *r*), indicating how they were calculated

Our web collection on statistics for biologists contains articles on many of the points above.

Software and code

Policy information about availability of computer code

Data collection	Zen black (Zeiss), In-Fusion cloning tools (https://www.takarabio.com/learning-centers/cloning/in-fusion-cloning-tools), NEBuilder Assembly Tool (https://nebuilderv1.neb.com/), Geneious 9.1.5, ApE v2.0.49.10, Wave 2.6, FACS Diva 6.1.3, ProSort 1.6, TraceFinder 4.1
Data analysis	Graphpad Prism 9, ImageJ (Fiji 2.3), FlowJo 10.7, Wave 2.6, R 3.2.1, Microsoft Excel 16.66, MATLAB R2022a. The MATLAB code for Hilbert analysis of oscillation properties can be found in github: https://github.com/md2981/Hilbert-Segmentation-Clock. The R custom package, mzrtools, for correction of natural isotope abundance in raw mass isotopomer distributions can also be found in github: https://github.com/wmoldham/mzrtools.

For manuscripts utilizing custom algorithms or software that are central to the research but not yet described in published literature, software must be made available to editors and reviewers. We strongly encourage code deposition in a community repository (e.g. GitHub). See the Nature Portfolio guidelines for submitting code & software for further information.

Data

Policy information about availability of data

All manuscripts must include a data availability statement. This statement should provide the following information, where applicable:

- Accession codes, unique identifiers, or web links for publicly available datasets
- A description of any restrictions on data availability
- For clinical datasets or third party data, please ensure that the statement adheres to our policy

All data are available within the article, supplementary files and source data files. Source data are provided with this paper.

Human research participants

Policy information about studies involving human research participants and Sex and Gender in Research.

Reporting on sex and gender	No human research participants in this study
Population characteristics	N/A
Recruitment	N/A
Ethics oversight	N/A

Note that full information on the approval of the study protocol must also be provided in the manuscript.

Field-specific reporting

Please select the one below that is the best fit for your research. If you are not sure, read the appropriate sections before making your selection.

☒ Life sciences ☐ Behavioural & social sciences ☐ Ecological, evolutionary & environmental sciences

For a reference copy of the document with all sections, see nature.com/documents/nr-reporting-summary-flat.pdf

Life sciences study design

All studies must disclose on these points even when the disclosure is negative.

Sample size	Sample sizes were not pre-determined. Rather, we ensured our sample sizes were sufficient by checking that inclusion of additional data points did not significantly change the variance (SD) of the data. In all cases, sample sizes were at a minimum n=3 independent experiments. Exact sample sizes are indicated in figure legends.
Data exclusions	In Seahorse assays, individual wells were excluded when oxygen consumption or extracellular acidification yielded negative values (non-physiological) due to bubbles trapped in the injection port. In Hilbert instantaneous period calculations, we excluded non-physiological period values (e.g. <0 or >30 hours) stemming from irregularities in the oscillation profiles.
Replication	To ensure the reproducibility of our findings, we carried out all experiments several independent times (exact n for each experiment reported in the figure legends). Each independent experiment contained technical triplicates. We ensured that these independent datasets of similar size did not change the reported results.
Randomization	Randomization is not relevant as the same cell lines were used in all cases: mouse vs. human comparisons were always made using the pMsgn1-Venus and MSGN1-Venus cell lines. Within wells of a multi-well plate, samples were randomly allocated to small molecule treatments.
Blinding	Blinding is not applicable to data collection because the investigator is aware of sample and treatment allocations while setting up the experiment. In the case of time-lapse imaging analysis, all labels were removed and individual microscopy files were analyzed blindly in ImageJ for all conditions tested. Similarly, flow cytometry files were blinded prior to analysis in FlowJo. For Seahorse experiments, sample identities were input into the software prior to data collection and analysis was automatically performed by Wave without input from the investigator, therefore negating the need for blinding. For plate reader-based assays, data was automatically collected and then analyzed in excel without sample labels, therefore essentially blinded. For all other assays, sample blinding was not necessary as the analyses were performed in an automated fashion with the software specified above.

Reporting for specific materials, systems and methods

We require information from authors about some types of materials, experimental systems and methods used in many studies. Here, indicate whether each material, system or method listed is relevant to your study. If you are not sure if a list item applies to your research, read the appropriate section before selecting a response.

Materials & experimental systems

n/a	Involved in the study
☐	☒ Antibodies
☐	☒ Eukaryotic cell lines
☒	☐ Palaeontology and archaeology
☐	☒ Animals and other organisms
☒	☐ Clinical data
☒	☐ Dual use research of concern

Methods

n/a	Involved in the study
☒	☐ ChIP-seq
☐	☒ Flow cytometry
☒	☐ MRI-based neuroimaging

Antibodies

Antibodies used

Primary antibodies:
Rabbit α PAX6 Biolegend cat. no. 901301, lotB277104
Rabbit α pHistone H3 (Ser10) Santa Cruz cat. no. sc-8656, lot D1615
Rabbit α Flag Cell Signaling Technologies cat. no. 14793S, lot 7

Secondary antibodies:
Goat anti-Rabbit Alexa-Fluor 488 conjugated secondary antibody (ThermoFisher cat. no. A11034), lot 2380031
Goat anti-Rabbit Alexa Fluor 594 conjugated secondary antibody (ThermoFisher cat. no. A11037), lot 2439060

Validation

All antibodies were validated by the suppliers:
PAX6: Reactivity against Human, Mouse, Rat. Each lot of this antibody is quality control tested by Western blotting and formalin-fixed paraffin-embedded immunohistochemical staining of brain tissue. For Western blotting, the suggested use of this reagent is 1.0 µg/mL (1:2000). For immunohistochemistry, a dilution of 1:50 - 1:100 is suggested. It is recommended that the reagent be titrated for optimal performance for each application. (https://www.biolegend.com/en-us/products/purified-anti-pax-6-antibody-11511?GroupID=GROUP26)

pHistone H3: Recommended for detection of Ser 10 phosphorylated Histone H3 of mouse, rat, human, Drosophila melanogaster, Xenopus laevis and avian origin by WB, IP, IF, IHC(P) and ELISA; also reactive with additional species, including and equine, canine, bovine, porcine and avian. (https://www.scbt.com/p/p-histone-h3-antibody-ser-10)

Flag: DYKDDDDK Tag (D6W5B) Rabbit mAb detects exogenously expressed DYKDDDDK proteins in cells. The antibody recognizes the DYKDDDDK peptide, which is the same epitope recognized by Sigma's Anti-FLAG® antibodies, fused to either the amino-terminus or carboxy-terminus of the target protein. (https://www.cellsignal.com/products/primary-antibodies/dykddddk-tag-d6w5b-rabbit-mab-binds-to-same-epitope-as-sigma-s-anti-flag-m2-antibody/14793)

Goat anti-Rabbit Alexa-Fluor 594: Product Specific Information
To minimize cross-reactivity, these goat anti-rabbit IgG whole antibodies have been cross-adsorbed against bovine IgG, goat IgG, mouse IgG, rat IgG, and human IgG. Cross-adsorption or pre-adsorption is a purification step to increase specificity of the antibody resulting in higher sensitivity and less background staining. The secondary antibody solution is passed through a column matrix containing immobilized serum proteins from potentially cross-reactive species. Only the nonspecific-binding secondary antibodies are captured in the column, and the highly specific secondaries flow through. The benefits of this extra step are apparent in multiplexing/multicolor-staining experiments (e.g., flow cytometry) where there is potential cross-reactivity with other primary antibodies or in tissue/cell fluorescent staining experiments where there are may be the presence of endogenous immunoglobulins.

Alexa Fluor dyes are among the most trusted fluorescent dyes available today. Invitrogen™ Alexa Fluor 594 dye is a bright, red-fluorescent dye with excitation ideally suited to the 594 nm laser line. For stable signal generation in imaging and flow cytometry, Alexa Fluor 594 dye is pH-insensitive over a wide molar range. Probes with high fluorescence quantum yield and high photostability allow detection of low-abundance biological structures with great sensitivity. Alexa Fluor 594 dye molecules can be attached to proteins at high molar ratios without significant self-quenching, enabling brighter conjugates and more sensitive detection. The degree of labeling for each conjugate is typically 2-8 fluorophore molecules per IgG molecule; the exact degree of labeling is indicated on the certificate of analysis for each product lot.

Target Information
Anti-Rabbit secondary antibodies are affinity-purified antibodies with well-characterized specificity for rabbit immunoglobulins and are useful in the detection, sorting or purification of its specified target. Secondary antibodies offer increased versatility enabling users to use many detection systems (e.g. HRP, AP, fluorescence). They can also provide greater sensitivity through signal amplification as multiple secondary antibodies can bind to a single primary antibody. Most commonly, secondary antibodies are generated by immunizing the host animal with a pooled population of immunoglobulins from the target species and can be further purified and modified (i.e. immunoaffinity chromatography, antibody fragmentation, label conjugation, etc.) to generate highly specific reagents. (https://www.thermofisher.com/antibody/product/Goat-anti-Rabbit-IgG-H-L-Secondary-Antibody-Polyclonal/A-11037)

Goat anti-Rabbit Alexa Fluor 488 conjugated secondary antibody: To minimize cross-reactivity, the goat anti-rabbit IgG whole antibodies have been highly cross-adsorbed against bovine IgG, goat IgG, mouse IgG, rat IgG, and human IgG. Cross-adsorption or pre-adsorption is a purification step to increase specificity of the antibody resulting in higher sensitivity and less background staining.

The secondary antibody solution is passed through a column matrix containing immobilized serum proteins from potentially cross-reactive species. Only the nonspecific-binding secondary antibodies are captured in the column, and the highly specific secondaries flow through. Further passages through additional columns result in 'highly cross-adsorbed' preparations of secondary antibody. The benefits of these extra steps are apparent in multiplexing/multicolor-staining experiments where there is potential cross-reactivity with other primary antibodies or in tissue/cell fluorescent staining experiments where there may be the presence of endogenous immunoglobulins. Alexa Fluor dyes are among the most trusted fluorescent dyes available today. Invitrogen™ Alexa Fluor 488 dye is a bright, green-fluorescent dye with excitation ideally suited to the 488 nm laser line. For stable signal generation in imaging and flow cytometry, Alexa Fluor 488 dye is pH-insensitive over a wide molar range. Probes with high fluorescence quantum yield and high photostability allow detection of low-abundance biological structures with great sensitivity. Alexa Fluor 488 dye molecules can be attached to proteins at high molar ratios without significant self-quenching, enabling brighter conjugates and more sensitive detection. The degree of labeling for each conjugate is typically 2-8 fluorophore molecules per IgG molecule; the exact degree of labeling is indicated on the certificate of analysis for each product lot. (https://www.fishersci.com/shop/products/alexa-fluor-488-goat-a/A11034)

Eukaryotic cell lines

Policy information about cell lines and Sex and Gender in Research

Cell line source(s)	human iPS NCRM1 line was obtained from RUCDR Infinite Biologics at Rutgers University https://commonfund.nih.gov/stemcells/lines#RMP-generated%20iPSC%20lines Mouse E14 mESCs (129P2 genetic background) were obtained from BayGenomics. Lenti-X 293T cells were obtained from Takara Bio cat. no. 632180
Authentication	Authentication was unnecessary due to the unique morphology of human iPS and mouse ESC colonies, as well as their unique differentiation potential. We nevertheless stained for pluripotency markers (Oct4, Nanog, Sox2). Lenti-X 293T cells were authenticated by the supplier. The cells were acquired immediately prior to experiments so there was no opportunity for contamination or misplacement.
Mycoplasma contamination	All cell lines tested negative for mycoplasma contamination.
Commonly misidentified lines (See ICLAC register)	No commonly misidentified cell lines were used.

Animals and other research organisms

Policy information about studies involving animals; ARRIVE guidelines recommended for reporting animal research, and Sex and Gender in Research

Laboratory animals	Mus musculus LuVeLu reporter line (Aulehla et al. 2008) E9.5 embryos
Wild animals	No wild animals were used in this study.
Reporting on sex	Both male and female embryos were used given that sexual dimorphism is not apparent at the E9.5 stage
Field-collected samples	No field collected samples were used in this study.
Ethics oversight	The study protocol was approved by Brigham and Women's Hospital IACUC/CCM. Protocol Number N000478.

Note that full information on the approval of the study protocol must also be provided in the manuscript.

Flow Cytometry

Plots

Confirm that:

☒ The axis labels state the marker and fluorochrome used (e.g. CD4-FITC).

☒ The axis scales are clearly visible. Include numbers along axes only for bottom left plot of group (a 'group' is an analysis of identical markers).

☒ All plots are contour plots with outliers or pseudocolor plots.

☒ A numerical value for number of cells or percentage (with statistics) is provided.

Methodology

Sample preparation	MSGN1-Venus or non-reporter mESC-derived or human iPSC-derived PSM cells were differentiated as indicated in Methods section. On the day of sorting, they were dissociated with TrypLE. For some experiments, cells were stained with dyes, antibodies or click chemistry as described in the methods section. The cells were resuspended in sorting buffer composed of PBS with 1% Pennicilin/Streptomycin and 2% fetal bovine serum.
Instrument	BioRad S3 Cell Sorter; LSR Fortessa

Software	ProSort; FACS Diva respectively
Cell population abundance	Initial cell population abundance varied by experiment. Post-sort fractions of MSGN1-Venus+ were >95% positive. For dyes, antibody staining and click chemistry, all cells were positive and we only quantified the intensity.
Gating strategy	We first selected for singlets by using an FSC height vs . FCS area gate. We then selected viable cells and excluded cell debris by applying an FSC vs. SSC gate. For cell lines carrying Venus reporters (mESC pMsgn1-Venus and hiPSC MSGN1-Venus), we used parental cell lines that do not carry the reporters as negative controls to determine the boundary between negative and positive cell populations. Parental lines were differentiated to a PSM state in parallel to experimental samples. For dyes, antibody staining and click-chemistry, negative controls without staining were used to set the gates.

☒ Tick this box to confirm that a figure exemplifying the gating strategy is provided in the Supplementary Information.